POLITECNICO DI TORINO

Collegio di Ingegneria Civile

Corso di Laurea Magistrale in Ingegneria Civile Geotecnica

TESI DI LAUREA MAGISTRALE

NUMERICAL STUDY OF FLINT/BOULDER BEHAVIOUR DURING PILE DRIVING

Relatori:

Prof. Guido Musso

Dr. Emilio Nicolini

Candidato:

Paolo Gargarella

Marzo 2018

A mamma e papà

Acknowledgments

In this important moment of my life I would like to express my sincere gratitude to all who accompanied me during the last five years and to all who have supported and helped during the development of this project. In particular, I would like to acknowledge:

- to my supervisor at Politecnico di Torino, Professor Guido Musso, who encouraged me to enroll this project, for the support and guidance offered;
- to Emilio Nicolini, for having proposed a so interesting theme, for having shared his experience and knowledge and for all the interest demonstrated in the project. Also, to all Cathie Associates staff that received me so well during the time that I was in the company in Paris;
- to all my friends and housemates, for all the good moments, fun and enjoy during these years;
- to all my university mates, for having eased the stressful times and for having made this period of my life unforgettable;
- to my girlfriend Cristina, for always being by my side, for supporting me for everything, for the patience, for making my life happy, for her precious advices and especially, for pushing me in this experience, for sharing it with me and for making it special;
- to my parents, for all the support and care, for always having encouraged me in all my own choices.

Summary

In the renewables offshore industry, structures are very often founded on driven, steel open ended piles. With the increasing size and power of the turbines, the piles dimension is increasing year after year, with the pile wall becoming more exposed to damages during driving, at the toe. This risk is particularly important where the soil is characterized by nodules or flints, which during pile driving operations could trigger the local buckling of tip steel wall and thus potentially cause the premature refusal of installation.

The study of the above phenomena implies the interaction of several elements: the structural behavior of the pile steel pipe, the confining effect of the soil surrounding the pile, the localized load produced by the hitting flint or nodule, just to mention the principal ones. The interaction of all these parts is quite complex and far beyond the normal computational and numerical capabilities of the engineering studies.

This thesis presents the results of a numerical study on the behavior of a nodule/flint under static and dynamic loading, which as shortly discussed above is part of a wider research frame, where the pile tip buckling is numerically investigated.

Flints occur usually within a weak chalky formation, so that they can potentially be displaced by the pile tip during penetration, without being broken. However, the impact of the pile wall tip on the flint is expected to produce a significant increase in its global resistance to displacement, and thus a reduction of the driving energy is envisaged to avoid pile tip damage. A similar problem could arise also in case of larger size, hard boulders embedded in glacial till grounds.

In this thesis, following a literature research to collect today's knowledge on the subject and the presentation of the results of the numerical analyses carried out, conclusions are drawn in terms of the static and dynamic forces necessary to displace a nodule/flint embedded in a softer formation, taking into account different geometries and soil properties.

Contents

List of figures

List of tables

Notation

γ_{dry}	dry unit weigth	$\mathbf{J}$	damping factor
γ_{sat}	saturated unit weight	$\mathbf{k}$	equivalent spring stiffness
γ_w	water unit weigth	$\boldsymbol{K}$	stiffness matrix
E_{oed}	oedometric modulus	$\boldsymbol{K'}$	bulk modulus of the soil structure
I_e	target element dimension	k_c	pile circular stiffness
N_b	ball penetrometer factor	$\boldsymbol{K_w}$	bulk modulus of the water
$\boldsymbol{N_c}$	T-bar factor	$\mathbf{L}$	cylindrical flint length
R_s	static soil resistance	$\boldsymbol{l}$	pile length
R_t	total soil resistance	$\boldsymbol{M}$	mass matrix
$\ddot{u}$	acceleration	$\mathbf{m}$	steps
$\dot{u}$	velocity	$\boldsymbol{m_r}$	mass of ram
$\boldsymbol{\alpha_N}, \boldsymbol{\beta_N}$	Newmark coefficients	$\boldsymbol{n}$	porosity
$\boldsymbol{\alpha_R}, \boldsymbol{\beta_R}$	Rayleigh coefficients	$\mathbf{n}$	sub-steps
$\boldsymbol{\sigma_y}$	pile yield stress	n_c	relative element size
Δt	time interval	N_{lim}	normal limit force
$\boldsymbol{A}$	cross-sectional area of pile	$\boldsymbol{N_q}$	bearing capacity factor
$\mathbf{B}$	Skempton's coefficient	$\boldsymbol{Q}$	quake
$\boldsymbol{C}$	damping matrix	$\boldsymbol{q_b}$	limiting end-bearing pressure
$\boldsymbol{c}$	wave speed in pile	$\mathbf{r}$	flint radius
C_1, C_2	relaxation factor viscous boundaries	R_{inter}	interface strength reduction factor
$\mathbf{d}$	flint diameter	S_u	undrained shear strength
$\mathbf{D}$	pile diameter	$\mathbf{t}$	pile thickness
D_R	damping value	T_{lim}	tangential limit force
E_u	undrained elastic stiffness modulus	**UCS**	unconfined compressive strength
$\mathbf{F}$	force	u_x	horizontal displacement
$\mathbf{f}$	frequency	u_y	vertical displacement
$\boldsymbol{G}$	shear modulus of soil	V_0	ram velocity
IP	index of plasticity	V_p	P-wave velocity

$\mathbf{V_s}$	S-wave velocity	$\boldsymbol{\nu}$	pile Poisson's ratio
$\mathbf{v_u}$	undrained Poisson's ratio	$\boldsymbol{\sigma_t}$	tensile strength
X	normalized displacement	**E**	pile Young's modulus
Y	normalized force	**u**	displacement
$\boldsymbol{Z}$	pile impedance=EA/c	$\boldsymbol{\delta t}$	time step
$\boldsymbol{\alpha_S}$	roughness surface factor	$\boldsymbol{\rho}$	density

1. Introduction

1.1 Scope and motivation

The constantly increasing demand of the world energy has led to a remarkable advancement in the offshore engineering field that is closely related to the wind energy production. In Europe the offshore wind industry has grown at an extraordinary rate over the last few years, particularly in the North Sea.

Offshore wind turbines are usually founded on monopiles with typical diameters of 4-6 m, and up to 8m in some cases, which makes the pile much less stiff as a direct consequence of the reduction of the thickness compared to the diameter. The pile is thus becoming more and more exposed to potential damage during driving, especially in particular geological condition (i.e. chalk with flints). To prevent this risk which would led to very expensive consequences, a thorough study on the pile-obstruction interaction during driving has been made with the aim of proving practical procedures to use in a driveability risk assessment analyses.

1.2 Aim of the research

In this work, the proposed investigation of the behavior of the flint will be carried out with a purely numerical approach and in particular by means of several finite element analyses in order to understand the pile-nodule interaction during driving. To create a robust model and to gain confidence with the mechanics of the problem, a 2D and 3D static model was first developed. Afterwards, a dynamic model was created. The following objectives were decided for this research:

- review flint and chalk geology, focusing on the engineering properties;
- study pile driving process, driveability analysis and pile buckling;
- study basic principles regarding the brittle behavior of rock;
- develop a static plane strain model and study the soil mechanism that arises when a static load is applied on a flint;
- provide failure forces and failure envelopes for different loading conditions;

- develop a static 3D model and compare the results with the 2D plane strain model;
- develop a dynamic 2D model for parametric analyses of flint displacements;
- provide an approximate law which returns, given flint size and chalk properties, the flint displacement due to a certain dynamic impact force;
- calibrate the pile thickness and/or the hammer energy to prevent the potential pile damage.

1.3 Structure of the document

Besides this initial introduction chapter, the present work is structured in 7 more chapters.

Chapter 2 presents a literature review on the offshore geology of south England. In detail, flints and chalk are studied in terms of characteristics, formation, location and engineering properties which will be used in the following analyses.

Chapter 3 is a general overview of pile driving in difficult conditions. The attention is focused on the pile tip buckling which could occur in presence of a flint. Moreover, the theories of the impact driving and of the driveability analysis are presented.

Chapter 4 analyzes the possible behaviour of a flint which is hit by a pile during driving. Three possibilities are considered: pile buckling, flint breakage and flint displacements. In the following chapters a more relevance will be given to the study of flint displacement.

Chapter 5 discusses the results of 2D finite element analyses with PLAXIS 2D. A plane strain model of a flint loaded in different positions is done in order to provide failure envelopes and failure forces.

Chapter 6 compares the results of 3D static analyses with the ones obtained in the previous chapter, in order to investigate a more realistic geometry than plane strain condition.

Chapter 7 reports the results of 2D dynamic analyses, in which the impact load generated by the pile on the flint during driving is modelled. An interpolating law, which links the peak force to the flint permanent displacement is found from a parametric analysis.

Chapter 8 summarizes the conclusions and proposes future developments.

2. Geology

2.1 Introduction

Chalks and flints are probably the two most conspicuous rocks in Europe, and were formed during the Late Cretaceous Epoch (60-100 million years ago). Chalk is generally considered to be a soft to hard, very pure white limestone and is very often associated with layers of the so called flints. By contrast, flints are a very to extremely hard, brittle and siliceous stones (Mortimore, et al., 2001). These latter are the common hard stones in the south and east of England and they usually occur within the chalk in layers and row of scattered lumps and noduli (Walter, 1972), as it is shown in *Figure 1*.

Figure 1. Nodular flint in Chalk (thecostalpath.net)

2.2 Chalk

2.2.1 Definition and characteristics

Chalk is a soft, white, porous, sedimentary carbonate rock. It is a form of limestone chemically composed of the mineral calcite which is an ionic salt called calcium carbonate or $CaCO_3$, with minor amounts of silt and clay (Hancock, 1975).

It is formed from the remains of tiny marine organisms (plankton) that lived and died in clear warm seas that covered much of Britain around 60 to 90 million years ago. When they died, they fell to the bottom in a rain of fine white mud (see §2.2.2). As chalk formed from the mud, layers and lumps of hard, glassy flint also developed (see §2.3.2).

Chalk has greater resistance to weathering and slumping than the clays with which it is usually associated; for that reason, it can form tall steep cliffs typical towards sea. The cliffs are eroded by wave action at the foot and, every few years, more of the cliffs above collapse, usually after heavy rain. The most famous chalk deposit is the White Cliffs of Dover bordering the English Channel, showed in *Figure 2*.

Figure 2. White Cliff of Dover (Giel, I. Photographer)

In *Figure 3* the presence of thin dark lines running horizontally is clearly visible: the darker bands which are seen are actually flint layers, regularly distributed along the cliff facing. Whilst the chalk in the cliffs was made from the calcium-rich skeletons of a number of plankton, called coccoliths, the flint is of a different origin. It is not calcium-rich at all, but formed primarily of silica (SiO_2).

Figure 3. Horizontal band of flint in cliff of Dover (discoveringfossils.co.uk)

The chalk is also a big aquifer and chalk ground-water provides much of the tap water for east and south-east England. In fact, because of its high porosity, water can drain down from the surface into cracks and cavities inside the rock.

According to Lake's work (1975), the English chalk could be classified as follow:

- the Upper Chalk, which is characterized by a high degree of uniformity being typically white, very pure (about 98% calcium carbonate), relatively soft and fine grained. Flints are present and may be nodular or tabular and may occur isolated or in bands (layers);
- the Middle Chalk, which is essentially similar but with a lower presence of flints. With increasing depth, this chalk becomes less uniform and harder;
- the Lower Chalk, which is constituted for about 80% of clay minerals. The resultant grey colored calcareous clays give rise to true marls, with a clearly different aspect and properties from the overlying chalks.

In the book "Engineering of Chalk" (Lord, et al., 2002), the Authors recognized the need for a revised approach to the classification of chalk in terms of its engineering properties, based on previous researches. In fact, Burland and Lord (1970) found that the difference in settlement behaviour of a loaded plate was due mainly to the spacing and aperture of the chalk discontinuities. Moreover, Clayton and Saffari-Shooshtari (1990) showed that the most easily measured property of chalk which is indicative of its behaviour in earthworks is the dry density (or porosity) of the intact block of chalk.

Thus, this new classification is based on the following listed factors, which most influence the behaviour of the chalk mass:

- dry density of the intact chalk;
- spacing and pattern of rock joints;
- aperture of joints.

On the basis of these factors, chalk may be classified into 4 grades, from A (structured chalk) to D (structureless chalk), as reported in *Table 1*.

Table 1. Chalk classification CIRIA

CIRIA density method				
Grade	D	C	B	A
Identification method	**Low density**	**Medium density**	**High density**	**Very high density**
Intact dry density[2]	< 1.55 Mg/m^3	1.55–1.70 Mg/m^3	1.70–1.95 Mg/m^3	> 1.95 Mg/m^3
Approximate UCS[3]	< 3 MN/m^2	3–5 MN/m^2	5–12.5 MN/m^2	> 12.5 MN/m^2
BS 5930 strength term	Very weak and lower end of weak	Upper end of weak	Moderately weak	Moderately strong
Ease of breaking fragments[9]	30–40 mm-thick fragments can be crushed between finger and thumb, and remould to putty[4]	30–40 mm-thick fragments can be broken in two using both hands, but cannot be crushed between finger and thumb[4]	30–40 mm-thick fragments cannot be broken in two[4]. Only thin slabs < 10 mm thick, and corners and edges of lumps can be broken with difficulty using both hands	Cannot be broken by hand. 100 mm-diameter lump can be broken by a single hammer blow when held in the palm of the hand[5]
150 mm nail penetration[6] [7] [10]	> 25 mm, putty formed around nail	15–25 mm	6–15 mm	< 6 mm
Used hammer pick penetration[7] [8] [11]	> 30 mm, chalk splashes	11–30 mm	2–11 mm	< 2 mm
New hammer pick penetration[7] [8] [11]	> 35 mm, chalk splashes	18–35 mm	6–18 mm	< 6 mm

In this work, the focus will be on the grade D chalk because this material required large piles to be installed as foundations, which in turn can be installed by driving. On the contrary, “hard” chalk of grades A is typically studied and used in civil engineering as a construction material.

Grade D chalk is a structureless material with a high porosity and relatively low density. It can be subdivided on the basis of engineering behaviour by the addition of the suffixes “m” or “c”. Where the fine graded chalk matrix dominates, the material will behave as a cohesive fine soil (grade Dm), and where the clasts (intact chalk lumps) dominate, the material will behave as a granular coarse soil (grade Dc). In the following pictures (*Figure 4-5*) a grade A chalk is compared with a grade D.

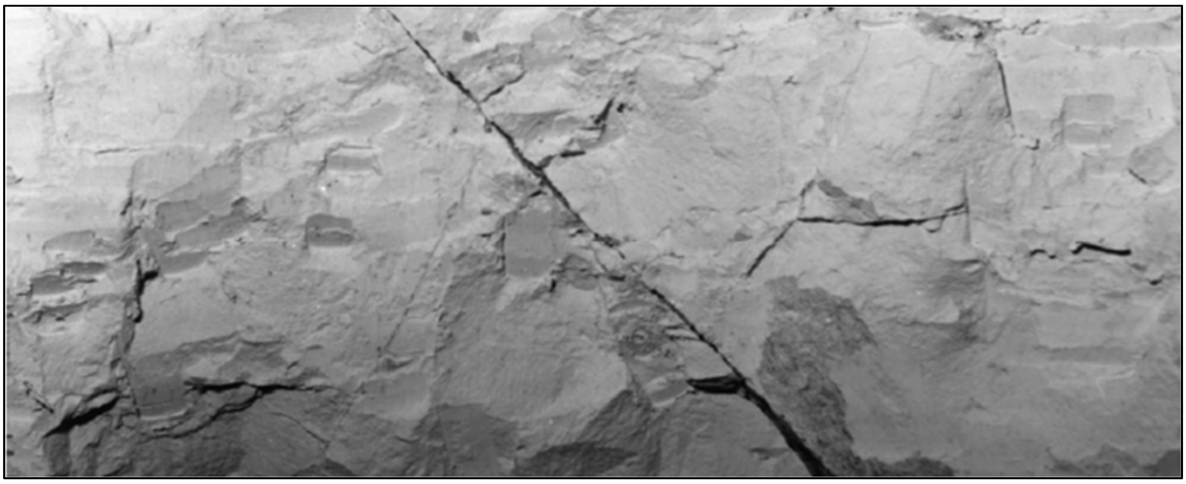

Figure 4. Chalk grade A (Lord et al., 2002)

Figure 5. Chalk grade D (Lord et al., 2002)

2.2.2 Formation

As already recalled, extensive chalk deposits were formed in the sea which covered most of northern and central Europe and Britain during the Cretaceous Period, 100 million to 60 million years ago. Chalk is mainly composed of microscopic skeletons of planktonic organisms called coccolithophores (Britannica, 2013). The coccolithophores are the most important group of chalk forming plankton. Each miniscule individual has a spherical skeleton called a cocosphere, formed from a number of calcareous discs called coccoliths, as it can be seen in *Figure 6*. After death, most coccospheres and coccoliths collapse into their constituent parts.

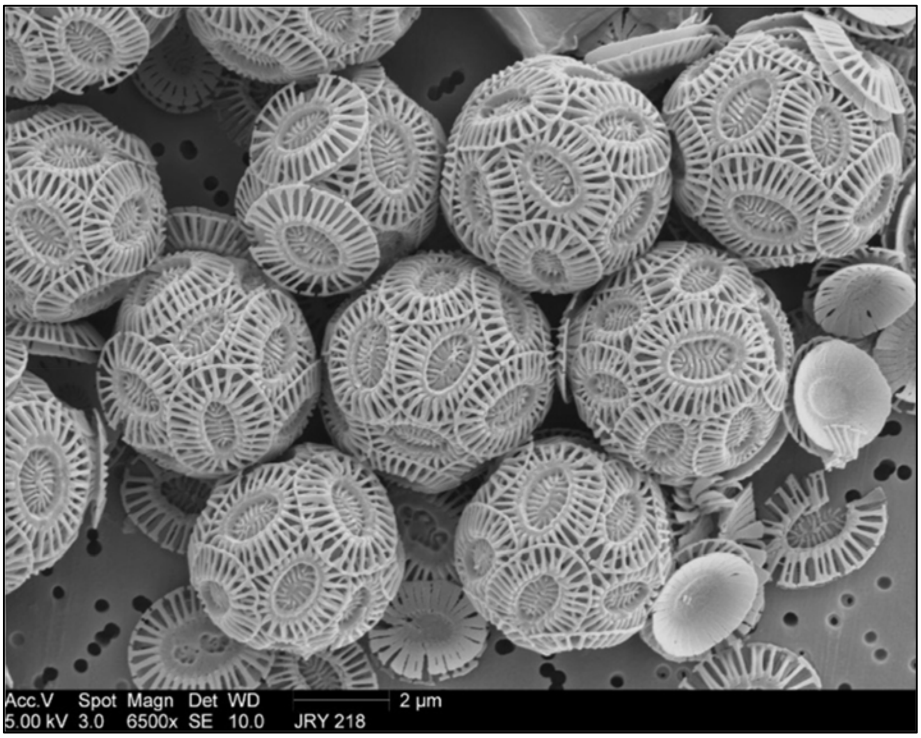

Figure 6.Coccolithophores (co2.ulg.ac.be/peace)

Chalk composition also includes fossils formed from the shells and skeletons of larger sea creatures. In fact, ocean-dwelling organisms such as oysters, clams, mussels and coral use calcium carbonate ($CaCO_3$) found in seawater to create their shells and bones. When these organisms die, their shells are left on the ocean floor, lake bottom or river bed where they may accumulate into thick deposits. Their shells and bones are broken down by waves and accumulate on the sea floor where they are compacted over millions of years, creating limestone from the sediments and the pressure of the overburden. This geological process is known as lithification: the lime mud is subjected to heat and pressure, which remove the water and compact the sediment, and by consequence it is converted into rock. Whether the chalk was subjected to further heat and pressure it would become marble (Monroe, et al., 2006).

Chalk is white because it is formed from the colorless skeletons of marine plankton. However, most limestones have a different coloration because they contain impurities, such as clays sourced from the land, or organics. The Cretaceous chalk is free from impurities because sea levels were very high, so there was little land exposed to supply other sediments. The result was a very pure lime mud, formed almost entirely of planktonic skeletons.

2.2.3 Location

The chalk in England is divided into two major sedimentary provinces, the Southern and the Northern Provinces, separated by a transitional area (Mortimore & Wood, 1986).

The chalk of southern England belongs to Anglo-Paris basin Province, which for the most part is characterized by soft, massive chalks with nodular chalks and hardgrounds at some levels. Flints, where present, are typically black.

The chalk of northern England, which occurs in Yorkshire, Lincolnshire, Humberside and north Norfolk, constitutes the Northern Province. Here the succession is characterized by hard chalks which lack hardgrounds, except in local condensed sequences and within sedimentary channels.

The distribution of the chalk in the British Isles, as it occurs at the present time, is depicted in *Figure 7* (Mortimore, 2010).

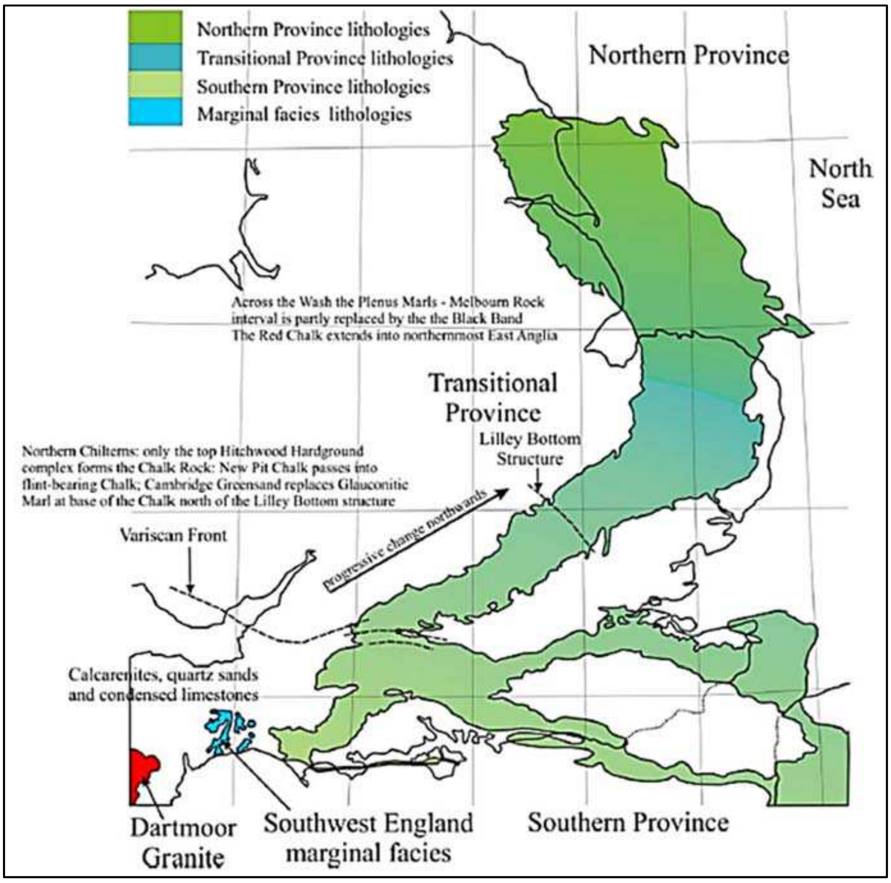

Figure 7. Distribution of chalk in England (Mortimore, 2010)

2.2.4 Properties

In composition, much of the chalk is a monotonous white material with variations coming only in the form of flints and mainly in the Upper Chalk. On the contrary, in terms of porosity the chalk is a material of great contrast and this variability has an important influence on its behaviour. A literature review was done in order to provide reliable values of the undrained shear strength, of the unit weight and of the elastic stiffness modulus.

First of all, reported strength parameters for intact chalk tested in the Hoek triaxial cell (Saffari-Shooshtari, 1989) show modes of behaviour which vary from that of rock, for high density very low porosity chalks, to that of undrained clay for low density very high porosity chalks, as it is shown in *Figure 8*.

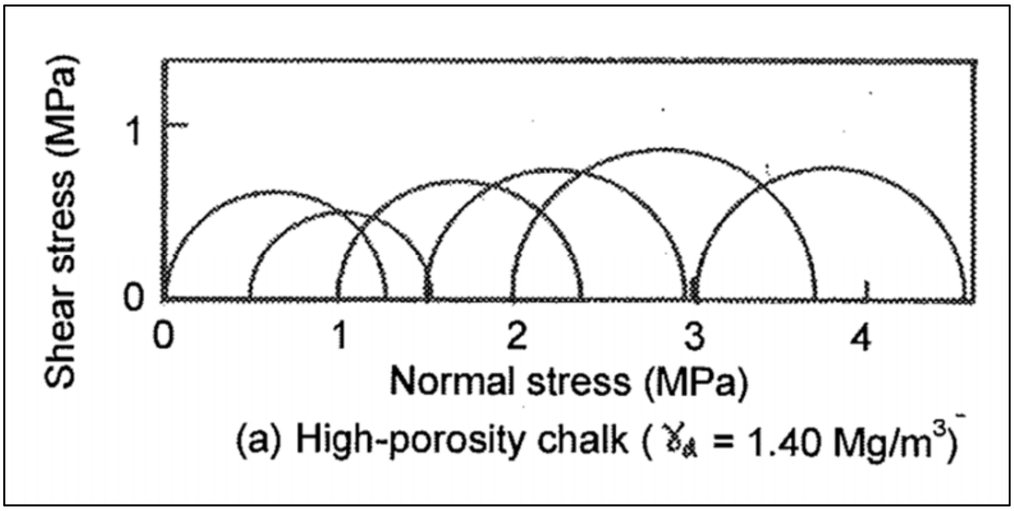

Figure 8. Results of Hoek cell tests for high porosity Chalk (Saffari Shooshtari, 1989)

Based on a literature study done by Lord (2002), the observed ranges of several index properties within the chalk are reported in *Table 2*. Especially for the dry density, the porosity and *UCS,* the variability is significant, due to the fact that 4 different grades of chalk were included in the data collected.

Table 2. Typical range of index properties for the chalk

Property		Units	Range
Dry density	γ_d	Mg/m³	1.29–2.46
Porosity	n*	%	9–52
Voids ratio	e*	—	0.10–1.10
Saturated moisture content	m_{sat}	%	4–40†
Calcium carbonate content		%	55–99
Specific gravity	G_s	—	2.69–2.71
Liquid limit	w_L	%	18–53
Plasticity index	I_p	%	4–30
Liquidity index		—	-2.25–+2.50
Point load index	$I_{s(50)}$	MPa	0.01–1.15
Unconfined compressive strength⁺	q_u	MPa	0.7–40
Slake durability index	I_{d2}	%	13–96

* calculated from dry density assuming $G_s = 2.70$
† wet

In fact, the effects of alteration can provide a fractured mass with properties that differ substantially from the intact properties, and an extreme weathering can lead to a completely structureless chalk.

Figure 9 shows a correlation between the *UCS* and the dry density, for both dry and saturated chalk. It is noted that, for same dry density, the unconfined strength of the saturated chalk is systematically lower than that of the dry one.

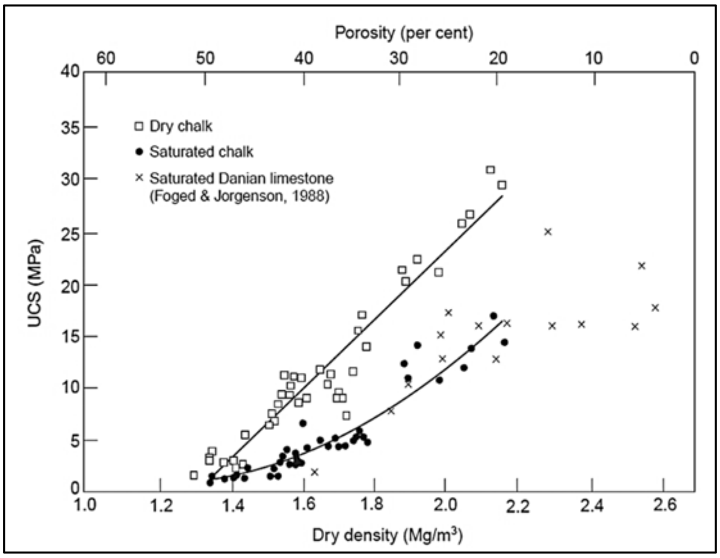

Figure 9. UCS vs intact dry density – (Matthews and Clayton, 1993)

Based on this data, for a high porosity grade D chalk (dry density between 1.4 and 1.6Mg/m^3) the *UCS* could be assumed around 2MPa or lower, and by consequence the S_u around 1MPa (the undrained shear strength of a cohesive soil is equal to one-half the unconfined compressive strength).

Based on Lord classification (Lord, et al., 2002), a low density chalk (grade D) could have an intact dry density lower than 1.5Mg/m^3 and an approximate *UCS* lower than 3MPa. By consequence, an approximate S_u should be lower than 1.5MPa.

Lake (1975), on the basis of test data concluded that the in-situ undrained shear strength of the weakest natural chalk is unlikely to be less than about 70 to 100kPa and for the characteristic soft virgin jointed chalks, it probably falls within the range 140 to 500kPa.

Personal experience within Cathie Associates proves that for grade Dm chalk, underwater and in marine environment, the values of UCS for saturated chalk in *Figure 9* above, in particular for dry densities within the range 1.4 to 1.6Mg/m^3, are to be considered an upper bound of the measured strength. Thus, the S_u to be considered should range between 100 to 500kPa.

In conclusion, referring to the values previously reported, in this work an undrained shear strength lower than 1MPa will be assumed.

Concerning the unit weight, if 15kN/m^3 is assumed as an average dry unit weight and a porosity of 40% is considered for a high porosity chalk, the saturated unit weight will be 19 kN/m^3, based on 2.1 relation (Lancellotta, 2012):

$$\gamma_{sat} = \gamma_{dry} + n\,\gamma_w \tag{2.1}$$

Finally, it is necessary to find a reliable value of the elastic modulus of the chalk. Until relatively recently, few reliable measurements have been made of the intact chalk. Matthews and Clayton (1993) report the results of numerous intact specimens, with varying porosities, which were tested with local strain measurement. For low-porosity chalks (grade A), the intact elastic modulus approaches 30GPa; for high-porosity chalks (grade D), it is in the order of 5GPa, as it is shown in *Figure 10*.

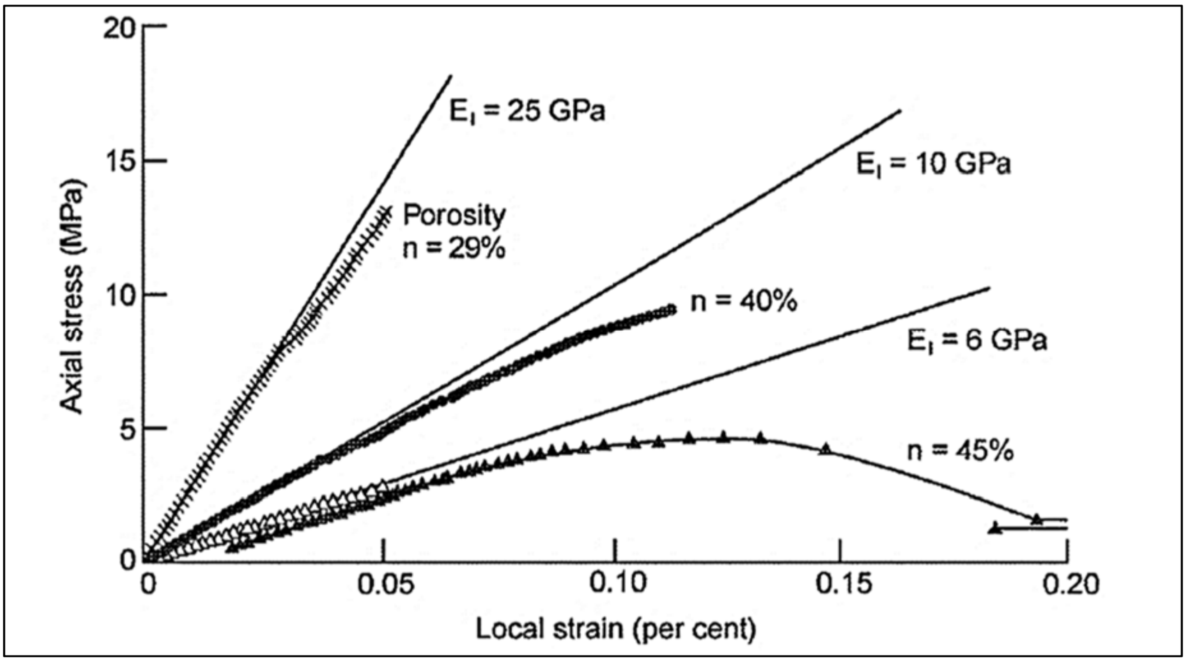

Figure 10. Stress strain curve for different porosity Chalks (Matthews and Clayton, 1993)

Since a high porosity chalk is considered, a value of the elastic modulus lower than 1GPa and a value of S_u lower than 1MPa will be considered, by assuming a ratio E_u/S_u=1000. The order of magnitude of this ratio could be also confirmed by Jamiolkowski's correlations for clays with an IP<30 (Jamiolkowski, 1979).

In *Table 3* are summarized the selected properties, previously analyzed.

Table 3. Grade D chalk properties

Dry unit weight γ_d	15kN/m^3
Saturated unit weight γ_s	19kN/m^3
Porosity *n*	40%
Undrained shear strength S_u	< 1MPa
Undrained elastic modulus E_u	< 1GPa
Ratio E_u /S_u	1000

2.3 Flint

2.3.1 Definition and characteristics

Flint is a hard, insoluble, sedimentary cryptocrystalline[1] form of the mineral quartz, categorized as a variety of chert (Frye, 1983). Thus, flint cannot be classified as a mineral but technically spoken can be defined as a rock consisting of a random mosaic of microscopically-small crystals of silica (only a few microns in diameter) tightly packed together.

It is primarily composed of silica (87%-99%) with an amounts of calcite and clay minerals. In fact, flint is not a chemically very pure quartz variety and the large amounts of impurities and its fine-grained structure can make it dull and almost opaque (Britannica, 2013).

Inside the nodule, flints are usually dark grey, black, green, white or brown in color, and often have a glassy appearance (*Figure 11*). The color can be caused by inclusions of organic compounds (black), metal sulfides (black), and various metal oxides and hydroxides (yellow, orange, brown, reddish, etc.). They are slightly translucent to almost opaque, sometimes only thin chips are translucent at the edges.

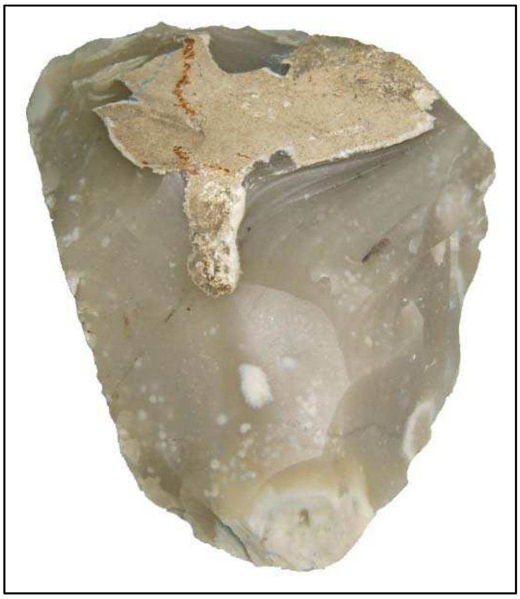

Figure 11. A light colored sample of flint (Crandell O. Photographer)

[1] rock texture made up of such minute crystals that its crystalline nature is only vaguely revealed even microscopically.

It occurs primarily as nodules and masses in sedimentary rocks, such as chalks and limestones. In sedimentology and geology, a nodule is a small, irregularly rounded mass of a mineral or mineral aggregate that typically has a contrasting composition from the enclosing sediment or sedimentary rock, such as a chert nodule in limestone (Boggs, 2009). Knauth (1994) refers to flint as "nodular chert", because he considers them equal in their basic physical properties.

Flint can have various morphologies: sheet, tabular, tubular, nodular and Paramoudra flints as in *Figure 12* (Clayton, 1986); they can be several decimeters in diameter, although typically measuring only some centimeters, and constitute a real major threat in drilling, boring, sampling and carrying out in-situ tests in the chalk.

Figure 12. Paramoudra Flint (flint-paramoudra.com)

2.3.2 Formation

The exact mode of flints formation is not yet clear, but it is thought that it occurs as a result of chemical changes in compressed sedimentary rock formations, during the process of diagenesis.

According to Nichlos (2009), diagenetic flints are formed by the replacement of calcium carbonate by waters rich in silica flowing through the rock. The source of the silica is mainly biogenic. In order to explain chert replacement of limestone it is necessary to identify geologic conditions where diagenetic waters are simultaneously supersaturated with respect to crystalline silica and undersaturated with respect to calcite.

Knauth (1979) presented a simple model where it is proposed that many nodular cherts in limestone have formed in the ground water where dissolution of biogenic opal and mixing of marine and fresh waters have produced waters highly supersaturated with respect to quartz and undersaturated with respect to calcite and aragonite (*Figure 13*).

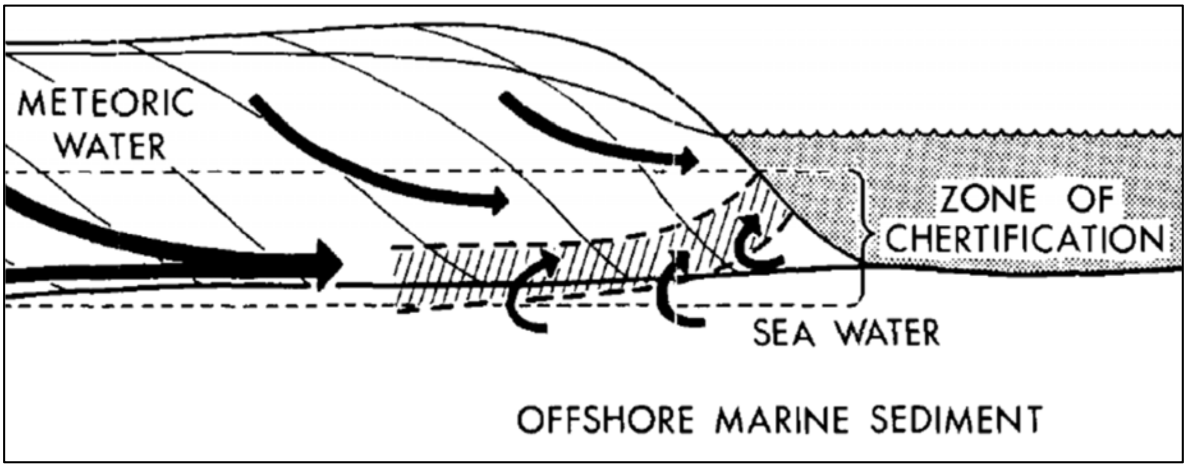

Figure 13. Zone of chertification (Knauth, 1979)

More in detail, this theory for silica diagenesis in chalk assume that flint has formed through dissolution of Si-containing organisms (primarily siliceous spicules of sponges) in the chalk followed by the precipitation/recrystallization of silica associated with replacement of chalk under special favorable chemical conditions (Lindgreen & Jakobsen, 2012).

Chert formed in this way occurs as nodules within a rock, such as the dark flint nodules that are common within the Cretaceous Chalk (*Figure 14*), and as nodules and irregular layers within other limestones and mudstones.

Figure 14. Flint nodule (geology.com)

The form of the replacement is probably controlled by the porosity-permeability distribution of the carbonate, the hydrologic flow, and various factors affecting nucleation. For example, nodules might grow outward from a nucleation site where the mixing zone occurs in sediment that is fairly homogeneous with respect to mineralogy, grain size, porosity, and permeability (Knauth, 1979).

2.3.3 Location

Flints exist within chalk units which are found widely in Europe, parts of the USA and the Middle East. In Europe, flints can be found in large quantities weathering out of the Cretaceous chalk cliffs of the Baltic Sea, in the North Sea and in the English Channel (e.g. the "Cliffs of Dover"). In France, flints can be found in Cretacean limestones in the region of Ile de France (Paris Basin), which was used during the prehistoric times (stone age). Similar flint deposits are found in Jurassic limestones of the Fränkische Alb in Bavaria, Germany.

Mortimore and Wood (1986) reviewed the distribution of flints in the English chalk, empathizing the difference of the stratigraphical distribution of flint bands between the Southern and Northern Provinces (*Figure 15*). In both parts of England, it has been demonstrated that a layer of maximum flint development is present near the top of the Turonian (the second age in the Late Cretaceous epoch) in all areas.

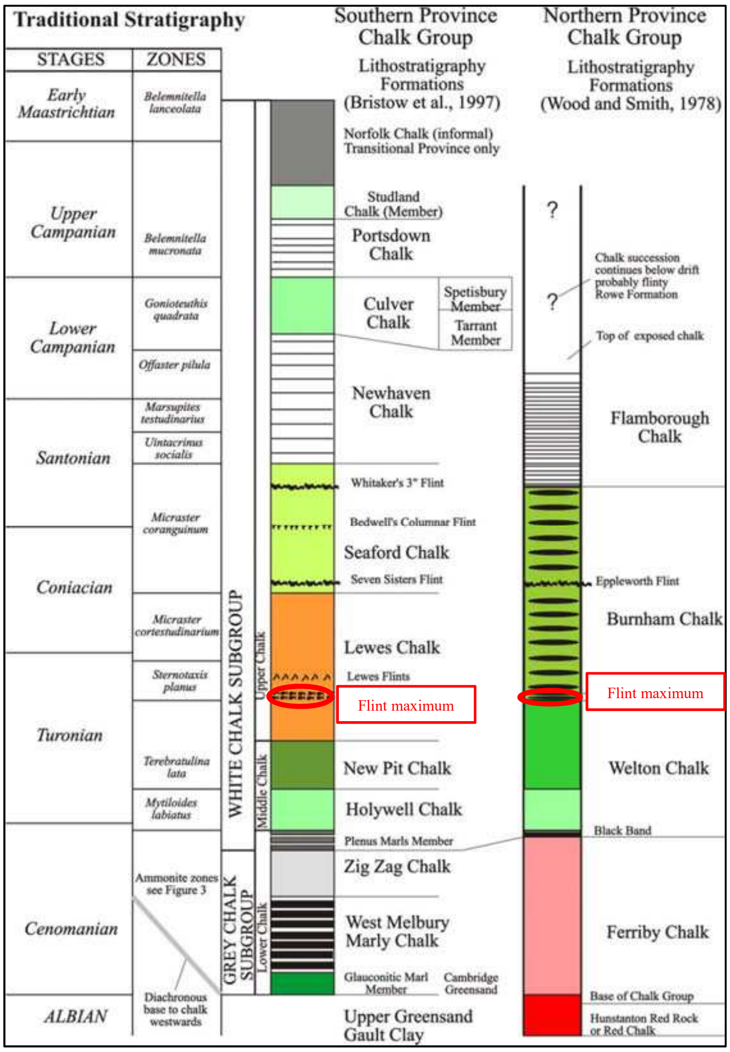

Figure 15. Distribution of Flint in the English Chalk (Mortimore & Wood,1986)

2.3.4 Properties

Flint is quite tough and not as brittle as quartz. Although the structure is homogeneous, it is not crystalline and stresses will dissipate in the material, whereas in a crystal a stress-induced small crack will often propagate through the entire crystal and split it.

The most interesting physical property of flint is the way it splits. Flint has a conchoidal fracture, but its fracture surfaces are not as uneven and curved. It is easier to control the direction of the splitting and the edges are more straight. This depends on the amount of impurities, "purer" flint behaves more like glass (Akhavan, 2013).

The variability of micro-structure/texture, chemical and mineral compositions of flint is reflected in the mechanical characteristics of flint, which are variable. For example, the fine grain nature of flints contributes to their strength.

There is very little information on the strength of flints. Uniaxial compressive strengths (UCS) can vary from 100 to 800 MPa; however, impact strengths[2] can be surprisingly low (see §4.3). Lautridou (1986) quote data from the Laboratoire Central des Ponts et Chaussées, reported in *Table 4*.

Table 4. Strength of flints (Latridou et al., 1986)

Compressive strength	391 MPa (3910 bars)
Brazilian strength	68 MPa (681 bars)
Impact toughness	13
Vickers Hardness	600–1200

Flint generally has a low porosity (i.e. <6% threshold necessary to be damaged from frost). However, Latridou et al. (1986) emphasize also the importance of flint porosity on the mechanical properties. In fact, many of the flints in the highest bed can have a carious, relatively high-porosity structure (Mortimore, et al., 2004), which indicates that the flint strengths may be at the lower end of the scale. Cumming (1999) has undertaken a number of tests on two types of flint, nodular and sheet flint. Her results are summarized in *Table 5*.

Table 5. Strength of flint (Cumming, 1999)

	Point Load I_{s50} (kN)	*UCS (MPa)*
Number of samples	31	6
Mean (all samples)	11	679
Mean (nodular flints)	12	
Maximum (all samples)	25	748
Maximum (nodular flint)	25	
Minimum (all samples)	1	586
Minimum (nodular flint)	1	

[2] impact strength is the capability of the material to withstand a suddenly applied load, it is expressed in terms of energy and is often measured with Charpy impact test, which measure the impact energy required to fracture a sample.

While flints are generally considered to be extremely strong, considerable variability is observed in their strength. Such variability was attributed to the presence of internal microfractures associated with the flint samples. These observations were supported by the work of Smith (2003), in which it is suggested that the variation in material properties of flints might also depend on its geographical location which can influence the mineralogical composition and/or the macrostructure.

Drilling in the chalk can be affected by flints as these materials are normally extremely strong and highly abrasive, which contrasts with the very weak to weak chalk. Due to their silica content, flints can result in significant wear of drilling bits and the cutting heads of tunneling boring machines (Lawrence, et al., 2017). In their study, Lawrence and Collier published some results of tests carried out on flints. *Figure 16* shows the results of variations in the tensile strength T_o, the *UCS* and the elastic properties comprising elastic modulus E_s and static Poisson's ratio *v,* of the flints studied. From these charts an elastic modulus of 80GPa, a tensile strength of 40MPa, an UCS of 500MPa and a Poisson's ratio of 0.125 can be deduced. These values will be considered in the following analyses.

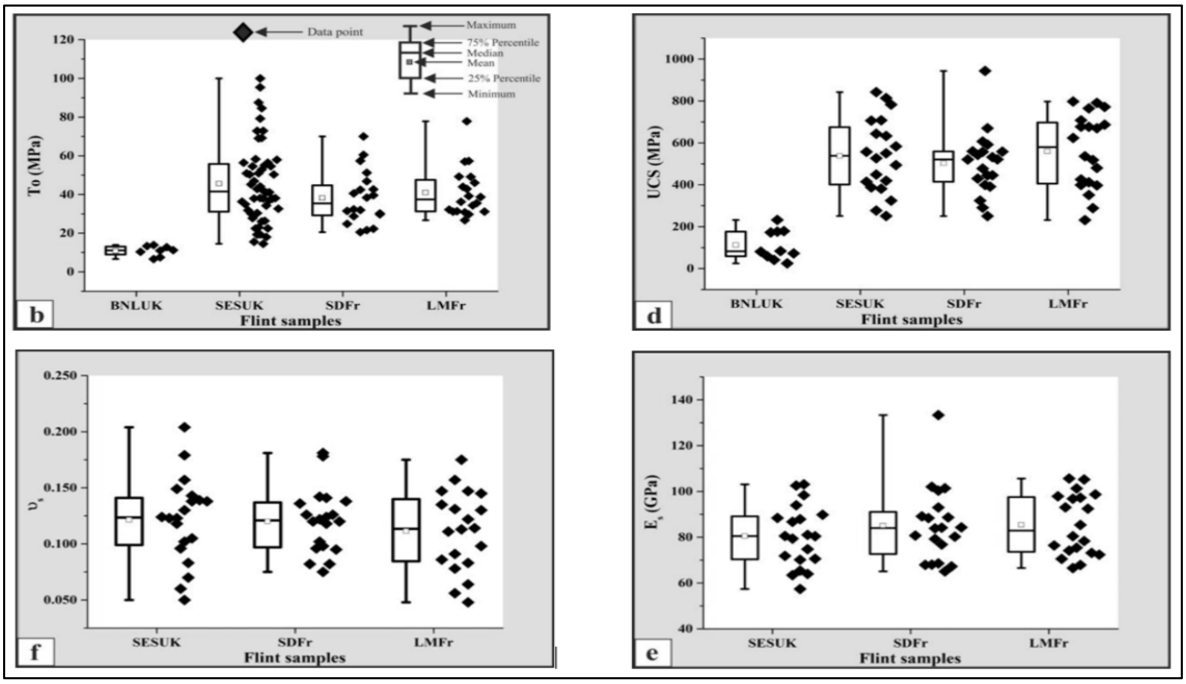

Figure 16. Tensile strength, UCS, Poisson's ratio and Young's modulus of flint from Burnham Chalk Formation-North Landing-Yorkshire (BNLUK), Seaford Chalk Formation-East Sussex (SESUK), Dieppe (SDFr), Lewes Chalk Formation Mesnil-Val-Plage (LMFr) (Lawrence, et al., 2017)

3. Pile driving in difficult conditions

3.1 Introduction

Driven steel pipe piles are widely used for offshore foundations (e.g. monopile wind turbine foundation illustrated in *Figure 17*) because of their good bending response and ease of installation, in principle. They are generally driven, open-ended, by means of a hydraulic or diesel hammer (Randolph, 2016).

Figure 17. Wind turbine monopile, length of 73.5 m and diameter of 6.5 m (eew-group.com)

With the increasing power of the turbines (up to 8 MW) and diameters of the rotor (up to 150m and more), the size of the piles is rising year after year (currently about 8m), with the pile wall becoming exposed to damages during driving, in particular at the toe. The potential for pile damage may be especially critical for piles with progressively higher *D/t* or diameter to wall thickness ratios, which are driven into formations with presence of boulders (Holeyman, et al., 2015).

The piles may encounter refusal due to high driving resistance, normally experienced in strong clays, or from "set-up" (i.e. the increase of shaft friction with time after driving) if pauses in the driving are significantly long. In particular, premature pile refusal can also be experienced if the pile tip encounters boulders, isolated or in layers. Such obstacles are able to produce localized forces and stresses which can easily (depending on several elements) expose the tip to the risk of the irreversible buckling of the steel walls (Strandgaard & Vandenbulcke, 2002). If soil conditions and the global geometry allow, the initial buckling can propagate in a major pile deformation and ovalisation while the pile penetrates, which can end in the complete closure of the tip or with a significant damage to the pile.

Thus, if during driving operation a flint or a continuous flint layer is encountered, refusal in penetration and/or tip buckling could happen, causing economical and time lost during off-shore operations.

3.2 Pile driving

3.2.1 Impact driving

Open ended piles are usually driven into the sea-floor (*Figure 18*) with impact hammers which use steam, diesel fuel, or more recently hydraulic power as the source of impact energy. Impact driving is a pile installation technique which can be very effective and relies on the beneficial effects (in terms of the temporary reduction of the pile capacity during driving) which follow the propagation of a shock stress wave along the pile. The pile wall thickness shall be adequate to resist axial stresses during pile driving.

Figure 18. Impact driving process (offshorewind.biz)

Rausche (2000) presents the state of the art regarding the impact driving technique. This process generally involves the hammer ram, hammer cushion (capblock), helmet (pile cap), pile cushion (only for concrete piles), pile and soil (*Figure 19*).

Hammer cushions are usually made of a resilient material and have the main objective of protecting the ram from excessive fatigue stresses. Pile cushions are designed for decreasing the stress in the contact points and for reducing the peak stress in the pile by distributing the impact force over the time. Helmets needs to align the hammer with the pile and to contain the hammer cushion. They are also used to spread the impact force over the pile top. Pile driving guides should also be used to make sure that the pile is maintained in the correct vertical alignment during installation.

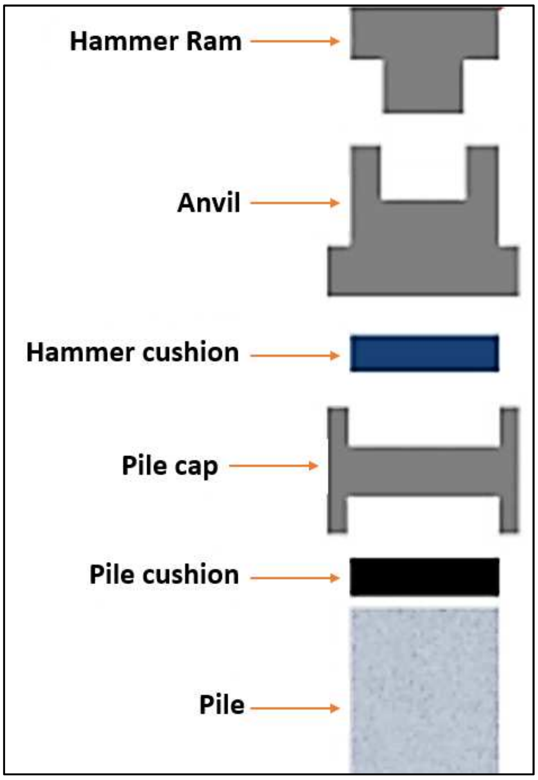

Figure 19. Scheme pile driving equipment

In the case of diesel or steam hammers, the hammers can be classified referring to their potential energy, which is related to the hammer height before the ram starts falling down. The kinetic energy available at the impact of the falling mass and this for the advancement of the pile within the soil is an only portion of the potential energy (friction, losses at the impact, etc.); the ratio between the kinetic energy and the potential energy is named efficiency.

Many hammer solutions are possible (i.e. air/steam hammer, diesel hammer, hydraulic hammer), but recently the trend is towards hydraulic hammers, which allow for very high driving energy to be delivered per each blow. These hammers were initially simple drop hammer fabricated to low drop heights in order to reduce the energy losses. On the contrary new hydraulic hammers consist of a piston rod and a piston connected to the ram. By means of the hydraulic power, the piston is pushed up and then accelerated downwards by the means of the oil pressure. The *Menck MHU* hammer which will be considered in this project shares these characteristics (see §7.2).

During driving the falling ram impacts and compresses the hammer cushion, accelerating the helmet, compressing the pile top cushion, and eventually moving the pile top. The applied impact generates an elastic compression wave which causes the advancement of the pile. The pile motion is contrasted by the soil resistance, which develop along the pile shaft and at its base. By consequence, the wave stress has to be high enough to overcome soil resistance (dynamic and static), and the motion has to be maintained for a sufficiently long duration to overcome elastic deformations and cause permanent pile set. Subsequent hammer blows produce cumulative pile penetration (Hussein, et al., 2003).

3.2.2 Driveability analysis

A rigorous assessment of the driving characteristics of a pile can be achieved by means of a proper dynamic analysis of the pile–soil system. Numerical techniques, such as finite element analyses, can take in account the inertial effects of the soil around the pile and its viscous behavior. However, typically the one-dimensional model suggested by Smith (1960) is used in driveability studies. In this first numerical model, the soil is simplified as a massless medium providing frictional resistance alone, while the pile is modelled as a discrete assembly of mass elements, interconnected by springs (*Figure 20*). Each component of the pile driving system is modelled with one or more of three devices: block (representing weight), spring (representing stiffness), and dashpot (representing damping effects).

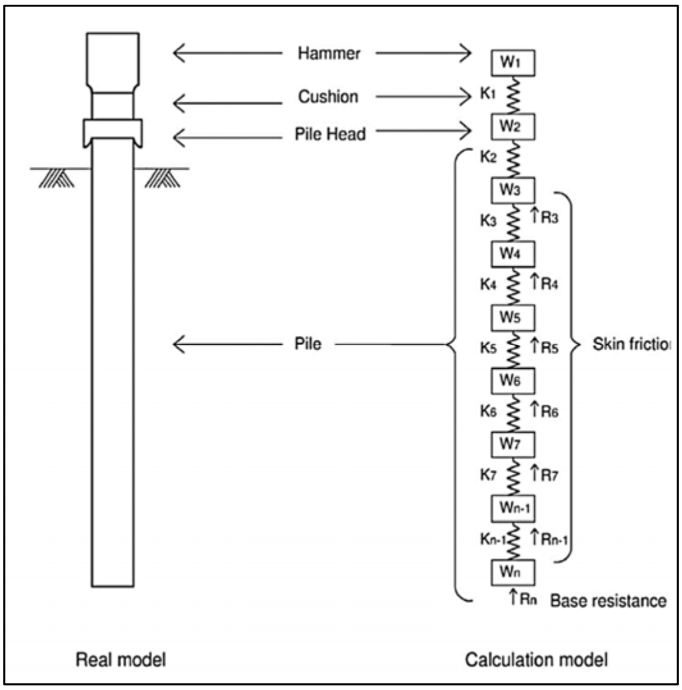

Figure 20. Pile-soil system model (Smith, 1960)

The soil resistance (*Figure 21*) is modeled with both dynamic and static components ($R_{tot} = R_{static} + R_{dynamic}$). The mobilized static shear or base force is displacement dependent and it linearly increases with displacement up to an ultimate strength, which is reached at for a fixed displacement named "quake"; the latter is also the displacement value above which perfectly plastic and irreversible displacements are cumulated. Instead, the additional dynamic shear or base force are modelled with a dashpot and by consequence they are velocity dependent and defined by a damping constant J [s/m] (Hussein, et al., 2006): $R_{dynamic} = R_{static}\,J\,v$.

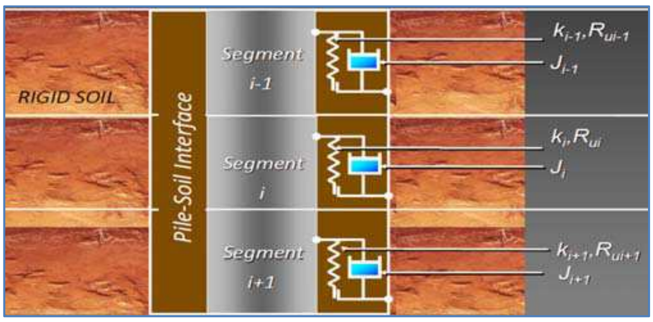

Figure 21. Soil model resistance (PDI)

At the design stage, the main objective of pile driving dynamic analysis is to assess the drivability of a pile in given soil conditions, and with a particular type and size of hammer. This is commonly accomplished using one-dimensional wave equation programs. Probably, the most widely known software is GRLWEAP (Goble & Rausche, 1986).

GRLWEAP software package developed by Goble and Rausche (1999) is one of the most used programs to optimize driving equipment selection and to predict pile characteristics. By means of this software it is possible to simulate pile installation by impact driving.

A possible way to carry out a driveability study with the wave equation method is to represent the results with the so-called bearing graph (*Figure 22*), which is a relation between the pile bearing capacity and pile blow count.

GRLWEAP also provides a suitable method to predict the blow count as a function of the pile penetration. These procedures comprise the so-called pile driveability analysis. This option calculates blow count, stresses and transferred energy versus pile penetration without running separate bearing graph analyses for each depth. Additionally, variables versus time can be also plotted or listed. The variables include accelerations, velocities, displacements, forces and stresses, for every pile segment.

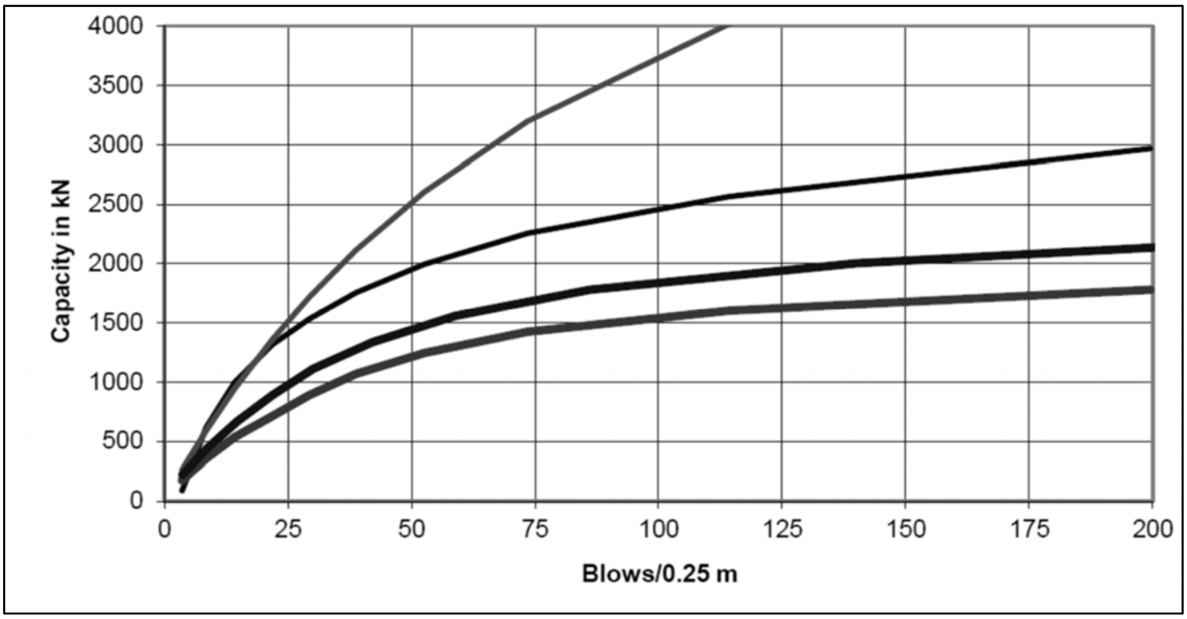

Figure 22. Example of bearing graphs for different soil (PDI)

These results are used to choose the most appropriate hammer, to assess the time and costs of installation of each pile and to provide a quality control on pile installation (in terms of required 'set' per blow for a given capacity). In addition, a drivability study includes the calculation of the maximum tensile and compressive stresses in the pile during driving, the maximum acceleration levels, and the range of required (or permitted) hammer strokes. Limiting the range of hammer stroke may be particularly necessary in order to avoid excessive stresses in the pile (Fleming, et al., 1992).

3.2.3 Refusal

During the design stage of a non-displacement pile, some aspects related with driveability shall be taken into account, such as driving stresses, tip damage and refusal. Refusal occurs when the desirable penetration cannot be achieved. This phenomenon happens because the soil resistance exceeds the hammer capacity or excessive stresses are induced in the steel pile wall. The first solution when pile refusal occurs is to use a higher performance hammers, if stresses allow. Another possibility is to remove the soil inside the pile so that the pile penetration resistance gets reduced; however, if the resistance offered by the soil inside the pile is decisive to the final bearing capacity, the pile must be refilled with soil or concrete.

The technical definition of pile refusal is primarily for contractual purposes to define the point where pile driving with a particular hammer should be stopped and other methods instituted (such as drilling, jetting, or using a large hammer) and to prevent damage to the pile and hammer. The definition of refusal should also be adapted to the individual soil characteristics anticipated for the specific location. Thus, the exact definition of refusal for a particular installation should be defined in the installation contract. An example of such a definition could be: "*pile driving refusal with a properly operating hammer is defined as the point where pile driving resistance exceeds either 300 blows per foot (0.3 m) for five consecutive feet (1.5 m) or 800 blows per foot (0.3 m) of penetration*" (API, 2014). From that recommendation, it can be concluded that a reasonable limit value to define refusal could be an average advancement of 1mm per blow. This in case stresses are not concerned; in any case, according to API specifications (2014) allowable driving stresses for steel piles should not exceeded the 80%-90% of yield strength.

Obstructions below the ground surface are often encountered during pile-driving operations. They are a matter of concern since they can prevent a pile from penetrating enough to provide adequate load-carrying capacity. Piles are frequently forced out of line by obstructions and may be badly damaged by continued driving in an effort to break through the obstruction. With steel or precast concrete bearing piles, extra blows of the hammer may break or dislodge a boulder; however, care must be taken that blows do not damage the pile (*Figure 23*).

Figure 23. Examples of heavily damaged pile toes (Broos, et al., 2017)

In fact, if the pile tip is damaged during driving, it could buckle and then collapse. Local pile tip thickening (usually referred to as a "driving shoe") could be employed to improve driveability, to provide reinforcement against local hard spots such as boulders and to reduce tip stresses. The shoe is an internal wall thickening which can in some cases also reduce the internal skin friction and by consequence the overall resistance to driving. Generally, the shoe consists of a length of pile at the tip which is increased in thickness by up to say 50%; the length of tip thickening varies but should be, according to earlier editions of API, a minimum of one diameter in length. The reduction in internal skin friction during driving is dependent on the decrease in effective contact stress against the pile wall, caused by the difference in diameter of the soil plug extruded through the shoe and the pile internal diameter (HSE, 2001).

Regarding the pile stresses, the driveability study must ensure that the pile is not overstressed and that the process of driving does not increase significantly the fatigue of the pile. In fact, the loss of pile shape due to the pile tip damage can result in the reduction of pile capacity or refusal.

3.3 Pile tip buckling

3.3.1 Background

During installation, pile tips and pile shells may be subjected to high stresses from pile driving forces and soil reactions. Some informal guide rules are observed on the choice of *D/t* ratios (diameter and pile thickness ratio) in the UK North Sea. However, no recommendations are provided on the analysis of these forces to ensure that the integrity of the pile or pile tip is guaranteed. In the case of particularly hard driving, pile shoes may be proposed, although this is generally for the purpose of reducing internal skin friction, and therefore reducing driving resistance.

Pile tip damage has occurred in some regions of the world where limestones or calcarenites are present (e.g. Arabian Gulf, Australian North West). In these cases, the tip damage appeared to be a local buckling. Whilst possible damage may remain undetected unless the pile has to be excavated for a secondary insert, damage could make driving more difficult and could reduce pile capacity (HSE, 2001).

3.3.2 Pile-boulder interaction

If a pile encounters a boulder (*Figure 24*), the resistance to driving is increased and this often results in premature refusal or the potential for pile tip damage. By consequence, predicting this type of occurrence is important since mobilizing and demobilizing remedial tools or the abandon of a pile is of significant expense, normally not acceptable.

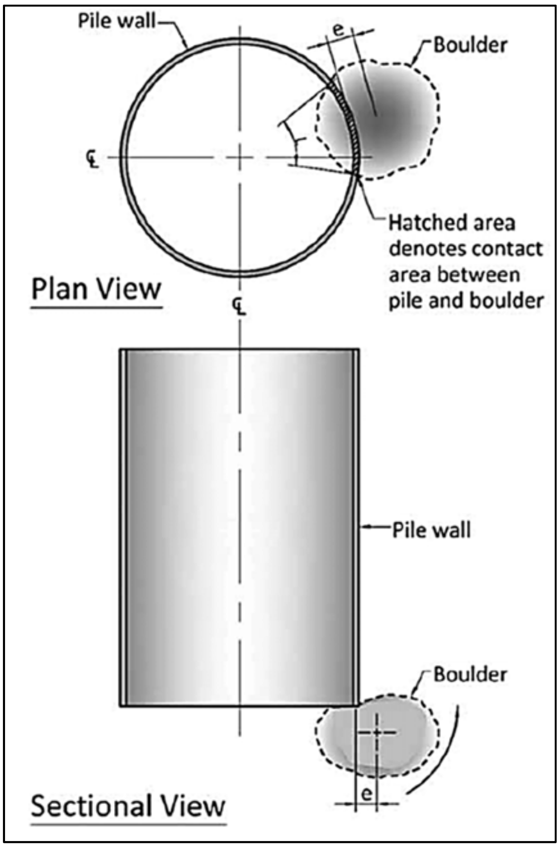

Figure 24. Schematic diagram of pile encountering a boulder (Stuyts, et al., 2017)

Damage to the pile tip may be encountered during the different pile driving installation stages. Whilst there are standard protocols to mitigate and check occurrence of damage to the pile during fabrication and handling, investigation of pile tip damage during driving into the soil is not typically performed and technical challenging.

However, damage to the pile is a real risk that can occur when the pile hits a hard stratum or encounters objects such as boulders in the subsoil as it is being driven. This type of failure or pile damage propagation is likely to occur for thin-walled piles and very stiff subsoil conditions such as very dense sand, stiff boulder-clay formations, and stiff chalk strata. Hence, the potential for pile damage may be especially critical for very large diameter tubular piles such as monopiles with increasingly higher *D/t* or diameter to wall thickness ratios, which are used to support offshore wind turbines and driven into boulder prone formations such as stiff glacial till. In fact, encountering a boulder during driving as the pile penetrates into the subsoil will cause a contact force at the pile tip that may be large enough to initiate a local imperfection or even local pile tip buckling (see 3.3.3). The magnitude of the contact force depends on the hammer settings and on the properties of the pile, the boulder and the embedding soil.

When a boulder is hit, it essentially impresses an external force on the pile which is dependent upon the following characteristics (see Chapter 5): boulder size, boulder strength, how centrically the pile encounters the obstruction and strength of the soil matrix in which the boulder is embedded. So, obstructions location, depth, size, matrix strength and geological unit must be identified. Key areas of the site can then be identified where the probability of encountering a boulder is high and the sizes of the boulder, matrix strengths and depth ranges can also be quantified.

Subsequently, the refusal occurrence can be investigated by determining if a given pile driving hammer, with a certain amount of energy, will overcome the pile resistance (skin friction and end bearing) and the enhanced end bearing associated with encountering a given boulder. An approximate value of the enhanced bearing due to the presence of the obstruction could be calculated by treating the obstruction as an equivalent shallow foundation where the width is assumed to equal the diameter of the obstruction (Stuyts, et al., 2017).

Holeyman (2015) suggests a mechanical model (*Figure 25*) to explore the interaction between a boulder and a pile being driven, taking into account the properties of the rock forming the boulder and the embedding geological formation. The proposed model is shown to highlight the influence of pile dimensions, boulder size, and hammer energy on the potential damage to the pile toe. Since boulder-pile interaction is a dynamic problem, the approach of the study is based on the 1D wave theory. Thus, the numerical analysis outputs the load exerted by the obstructing boulder as a result of the hammer generated wave force. The peak contact force is then compared to the minimum axial force required to initiate local pile tip buckling. If this peak contact load is clearly in excess of the pile local yield load F_{axial}, one must check whether the soil would not fail before the steel tube would locally yield. So, the peak axial contact load obtained by the contact model in the wave equation analysis should be compared to the boulder ultimate resistance to penetration within the soil matrix. If this is bigger, this indicates that the driving force acting on the boulder is able to plastically displace the boulder within its soil matrix. The ultimate resistance of the boulder to a vertical displacement has been assessed based on the undrained shear strength S_u of the embedding medium, using a classical formula of the ball penetrometer (see 6.2.1). For the sake of simplicity, the boulder has been assumed to have an axisymmetric shape and it is considered a rigid body since it possesses a much higher modulus than that of the embedding medium (Holeyman, et al., 2015).

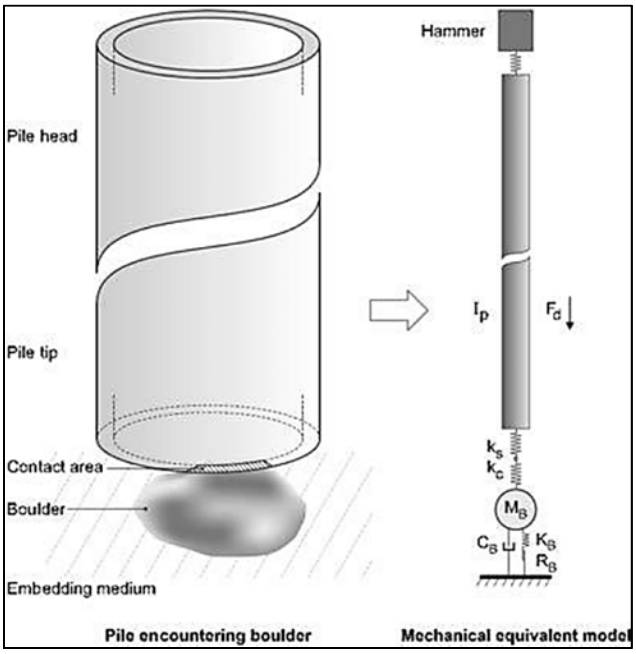

Figure 25. Pile-boulder-soil model (Holeyman, et al., 2015)

However, Holeyman study investigates the problem of the ultimate resistance of the boulder with a classical formula which returns a static failure force. This approach is not able to return the associated boulder displacement, but only a threshold value of the failure force. Since the driving process is a dynamic impact problem, the peak load has a very short duration (some millisecond) and it will produce a certain penetration depending on its magnitude. Starting from this study, the aim is to investigate deeply the plastic penetration mechanism of the boulder subjected to a dynamic force, to find a relationship between the arising dynamic force on the pile and the boulder displacement.

3.3.3 Local buckling

Pile tip damage can arise by various mechanisms:

- pile tip local buckling due to high contact stresses;
- classical ring or shell buckling under lateral pressure;
- ovalisation of initially imperfect tube under lateral pressure;
- enlargement of initially dented pile, under the action of lateral soil pressures;
- propagation buckling of damaged pile.

For the large diameter piles considered, classical ring or shell buckling and pile flutter during driving are not a risk and will not be considered further (see results of HSE study (2001)). So, the main risks for pile tip damage are considered to be: local tip buckling caused by high end bearing contact stresses, or local denting and progressive enlargement of the defect in the pile as penetration continues. *Figure 26* shows a typical distortion of a lower part of the pile that met refusal in a hard layer in the North Sea (Valhall).

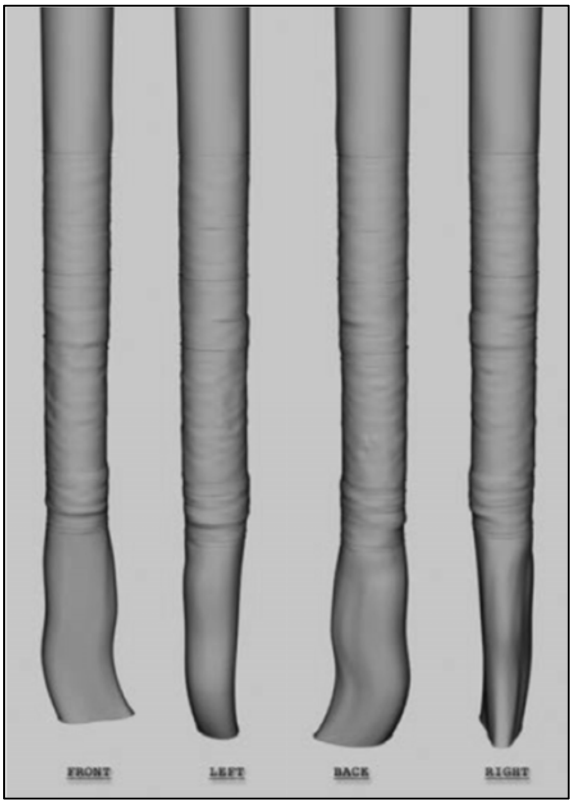

Figure 26. Extrusion buckling of pile tip

Different potential sources of pile tip damage can be identified, including obstructions within the soil. In fact, the pile tip may be deformed by hitting obstructions within the soil, such as boulders. An approximate force given by any obstruction can be estimated from basic soil mechanics principles, but dynamic effects may increase the peak forces and should also be considered (aim of this thesis). Therefore, this risk assessment is concerned with the risk of encountering obstructions in the soil, which can then lead to permanent deformation and damage to the tip.

According to API (2011), unstiffened cylindrical members fabricated from structural steels should be investigated for local buckling due to axial compression when the *D/t* ratio is greater than 60. When the *D/t* ratio is greater than 60 and less than 300, with wall thickness $t > 6$ mm, the elastic buckling force F_{xe} due to axial compression should be determined from:

$$F_{xe} = 2\,C\,E\,\frac{t}{D} \tag{3.1}$$

where C is a buckling coefficient, D is the outside diameter in meter and t is the wall thickness in meters. The theoretical value of C is 0.6; however, a reduced value of $C = 0.3$ is recommended to account for the effect of initial geometric imperfections.

Moreover, the following equation is proposed in order to determine the force that causes local denting[3]:

$$F_{tip} = 1.2\,\sigma_y\,t^2 \tag{3.2}$$

Aldridge et al. (2005) present a simplified approach for assessing the value of the vertical and horizontal force which could cause tip buckling. They assessed the point load that would cause such buckling using upper bound theory for an assumed plastic hinge mechanism. In this approach, a mechanism of plastic hinges and deformation under an applied load is assumed, and will always give an upper bound to the load actually required to cause deformation. The assumed mechanism in this case is presented in *Figure 27*.

[3] a pile tip could be damaged with the formation of a dent during installation; subsequently loading during driving could lead to enlargement of this dent, so that eventually unacceptable deformations may build up.

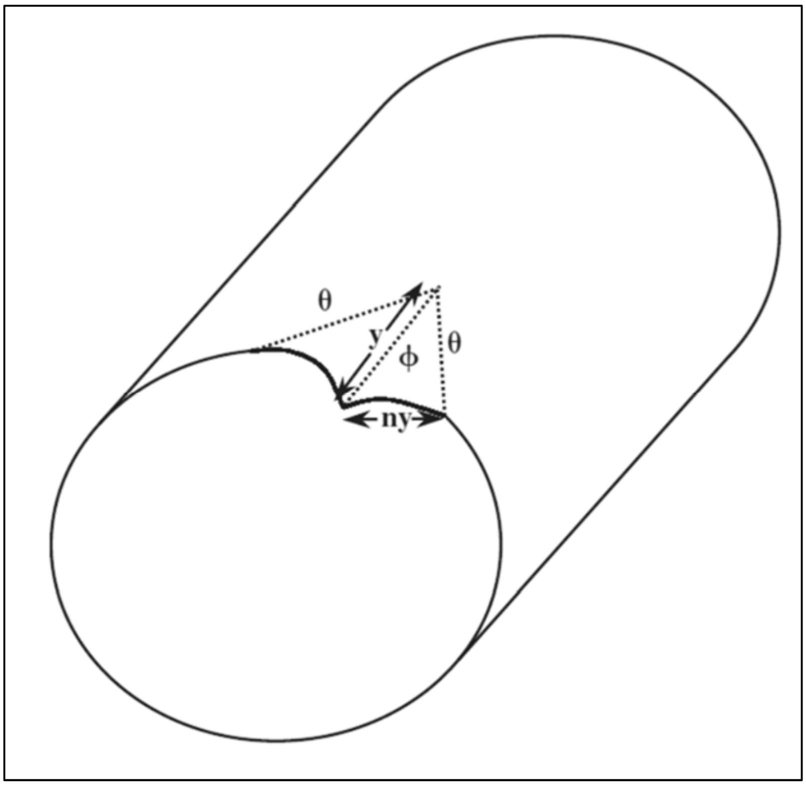

Figure 27. Plastic hinge mechanism assumed (Aldridge, et al., 2005)

This approach, gives the lateral load $F_{lateral}$ which causes plastic hinge formation at the tip of a uniform large diameter thin-wall tube as:

$$F_{lateral} = 1.4\, \sigma_y\, t^2 \qquad 3.3$$

Since this result was simply an upper bound value, the authors have confirmed the validity of the equation by means of laboratory tests on steel tubes and 3D elasto-plastic finite element analyses. Further laboratory tests and 3D finite element analyses were then performed to determine the axial force that would cause a local buckle at the tip:

$$F_{axial} = 2.8\, \sigma_y\, t^2 \qquad 3.4$$

It is notable that for the large diameter steel pipe piles used offshore, the local lateral and axial buckling is not dependent on *D/t*, as is often assumed (e.g. according to API), but simply on the pile wall thickness and steel yield stress. This formulation will be used as a reference for the following analyses.

4. Flints behaviour

4.1 Introduction

As widely discussed in the previous sections, during pile driving in a chalk formation, the pile could encounter a layer with flints. If the pile hits one of this nodules, three phenomena could occur:

- pile local buckling;
- flint breakage/splitting;
- flint displacement (soil bearing capacity failure).

Concerning the first point, different studies have been already performed and in Chapter 3 a literature review has been presented.

Referring to the second and the third point (flint breakage), it is interesting to understand which phenomenon could occur, depending on the geotechnical condition and on the soil properties (*Figure 28*).

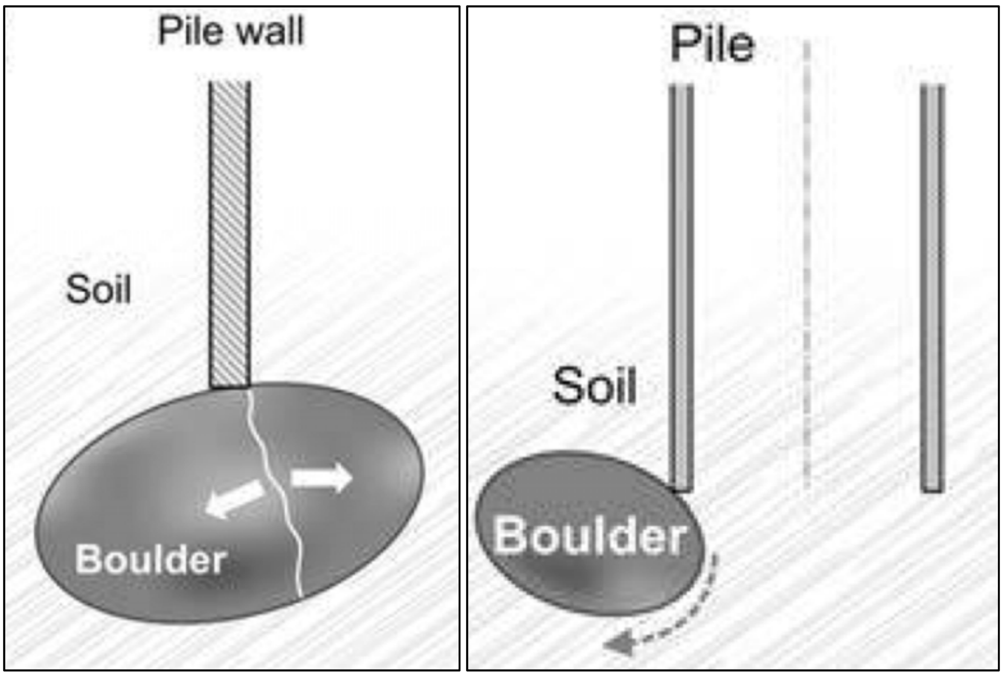

Figure 28. Boulder splitting and boulder displacement (Holeyman, et al., 2015)

When the pile receives the hammer stroke, if it is in contact with the flint, it will transmit a local force which could break the boulder and split it in pieces. A comparison with the so called Brazilian test (see §4.2), frequently used to determine the tensile strength of concrete and rocks, could be a first approach to understand the main features of the problem, even if the real failure would happen under a confinement due to the embedding soil. Also the loading condition is different from this type of test, because the soil around the flint produces a distributed and no punctual reaction. However, because of the lack of similar tests have been already carried out, it is assumed that the pile will produce a splitting of the flint like in a Brazilian test configuration, since the tensile strength in rock is always much lower than the compressive strength.

Moreover, the actual flint resistance could be significantly lower if the effects the repeated loading and the accumulation of fatigue damage are taken into account. Thus, it would be also possible to generate a fracture propagation in flint varying the energy of the hammer. Summarizing, generally rocky materials are “brittle” and in particular because of that, the tensile strength becomes one of the most important parameter influencing deformability and fracture toughness.

According to the third case (flint displacement), if the flint itself has a strength much higher than that of the surrounding soil, a “bearing capacity like” failure should occur before the boulder breaks. By consequence, the pile should progressively displace the flint after a certain number of strokes and the following advancement will proceed regularly. The problem is that the flint displacement will produce a reaction force which will act locally on the pile wall, with the risk of triggering the initiation of pile buckling. Therefore, it will be necessary to calculate the flint displacement per blow for a fixed impact force, and by consequence have a relationship with the hammer energy per blow allowing to avoid to damage the pile.

4.2 Brazilian test

The Brazilian test is used in general for the indirect measurement of the tensile strength of rocks and concrete. In this test, a disc shape specimen is loaded by two opposing normal strip loads at the disc periphery. The load is slowly and continuously increased at a constant rate until failure of the sample occurs, normally within few minutes. At failure, the tensile strength of the rock specimen is calculated as follows (ISRM, 1981):

$$\sigma_t = \frac{2\,F}{\pi\,d\,L} \qquad 4.1$$

where P is the applied load, d the diameter, and L the thickness of the sample.

Equation 4.1 uses the theory of elasticity for isotropic continuous media and gives the tensile stress perpendicular to the loaded diameter at the center of the disc and at the time of failure. If the sample is anisotropic and exhibits weakness planes (preferred orientation of minerals or stress history), the specimen should be prepared in such a way that both directions parallel as well as perpendicular to such planes can be tested (axis of the cylinder parallel to the plane). In *Figure 29* is reported one possible configuration for the indirect tensile strength determination.

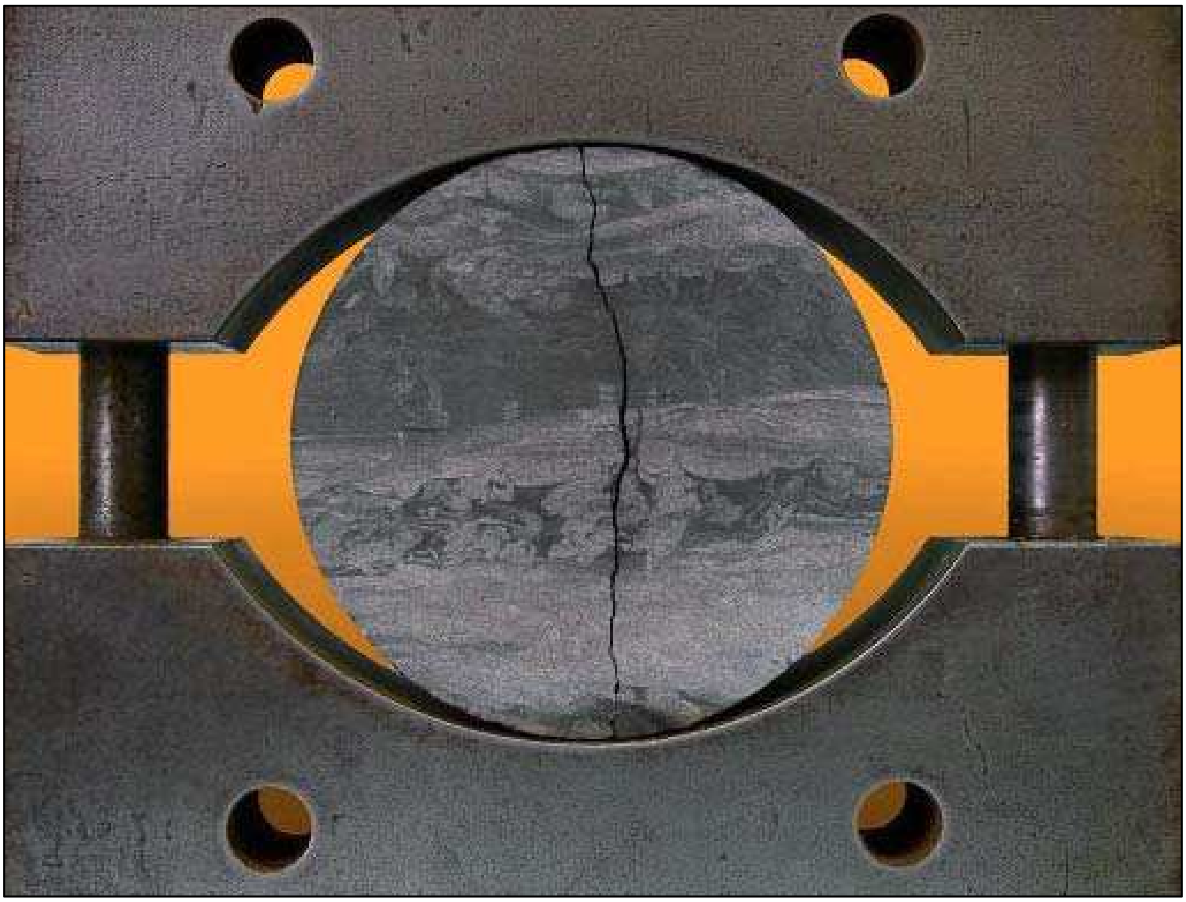

Figure 29. Brazilian test (geolabs.co.uk)

4.3 Brittleness and fatigue

Environmental and human-induced loading works often in a cyclic way, such as in the pile driving process. By consequence, wave propagation is induced and soil is subjected to repeated time-dependent loads. This definition covers a large range of loadings distinct in amplitude and frequency.

The loading of a rock sample may be considered dynamic if the inertial forces generated within the material are significant with respect to the loading force. Dynamic loading is commonly encountered due to shocks, blasting, etc.; it is the case of a flint which is struck by a pile during the driving process. On the contrary, the inertial forces are negligible during quasi-static loading. However, no universal loading rate threshold has been established to differentiate between quasi-static and dynamic behaviours of the material. A loading rate equal to 0.05 MPa/s for uniaxial compression experiment on granite is proposed by Zhao (2000).

Rocks generally have fragile behaviour especially if subjected to cyclic or repeated impact loads. As a matter of fact, brittleness is an important rock property which affects the rock fracturing process. By definition, ductile fracture is always accompanied by a significant amount of plastic deformations, while brittle fracture is characterized by very limited plastic deformations (Nejati & Ghazvinian, 2013). *Figure 30* depicts difference of brittle and ductile tensile failure.

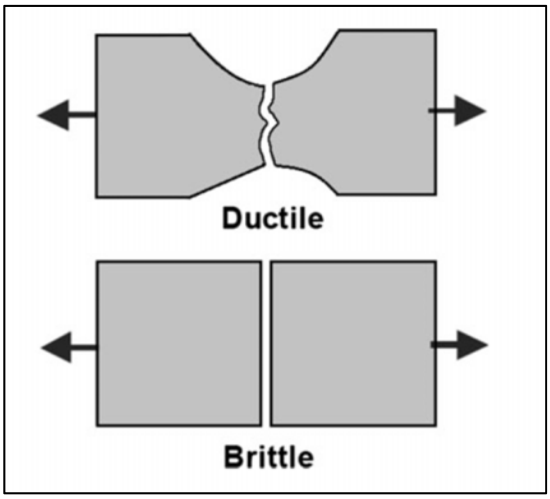

Figure 30. Brittle and ductile fracturing (Nejati & Ghazvinian, 2013)

Cyclic loading mainly results in accumulation of damage cycle after cycle: this phenomenon is called fatigue. By consequence, failure occurs for a maximum cyclic stress which is lower than the monotonic strength of the intact rock. This means that a sample cyclically loaded at constant amplitude or load eventually fails even if the peak load is lower than the monotonic strength.

A simple way to illustrate the fatigue effect on the resistance is to relate the maximum stress applied to the number of cycles necessary to reach failure. Such way of representing the fatigue is expressed by means of the so-called S–N or Wöhler curves, which are common use for engineers whatever the material (Schijve, 2003). S–N curves are very synthetic, simple and fatigue limit may be directly used in design methods (*Figure 31*). The limitation of the S-N approach is that it assumes a constant amplitude of the cyclic load for all the cycles and cannot directly deal with cyclic loads of variable amplitude; this is however solved by grouping together cycles of equal amplitude and summing the equivalent cumulated fatigue damage.

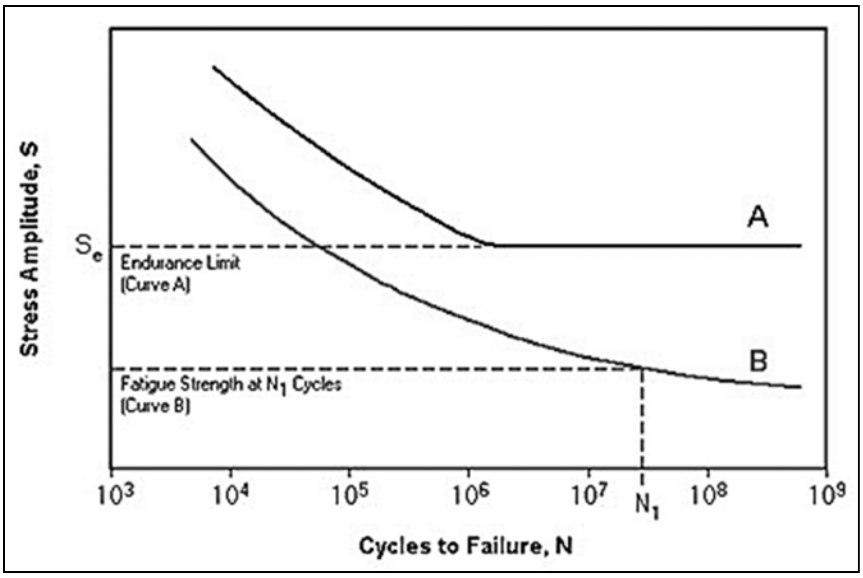

Figure 31. Typical S-N curve (totalmateria.com)

The fatigue limit or fatigue strength may be defined as the stress amplitude for which there is no failure of the specimen, i.e. the fatigue life becomes infinite. Based on a literature study done by Cerfontaine and Colling (2017), if no data are available on a particular rock material, a fatigue limit of 0.7 times the monotonic strength may be assumed. This limit should be used cautiously since the estimated fatigue limit mostly depends on the patience of observers. Failure may occur for a lower stress but also more than one million of cycles. However, a million of cycles should be sufficient to encompass most applications of rock engineering. In fact, referring to the pile driving, the order of magnitude of the number of cycle accepted to break a flint could be 500 to occasionally 1000 blows; after this number of blows the refusal is considered.

The crushability and the brittleness of flints has never been deeply investigated during recent years. The almost totality of the researches were focused on the investigation of the fragile behaviour of different type of soft and hard rocks and concrete. Moreover, most of the published results derive from standard test procedures (i.e. Brazilian Test, Impact Load Test) performed on unconfined samples. This specimen configuration could lead to an underestimation of the energy/load necessary to initiate and propagate the fractures and it seems more reliable to perform test subjected to a confined stress.

In conclusion, in order to investigate deeply flint breakage under impact loads, laboratory tests such as dynamic load tests on flints would be useful in order to define different type of curves S-N and by consequence to determine cyclic stress-number of cycles to failure of flint subjected to tensile loads.

4.4 FEA of flint breakage

A preliminary finite element analysis is done in order to analyze the behaviour of a 0.2m-diameter circular flint embedded in a chalk, subjected to an imposed centered vertical displacement (for more detail on the finite element model see Chapter 5); as well, also the case of a 2m-diameter boulder was analyzed and the same results were achieved. The chalk is modelled with an elastic-perfectly plastic constitutive model, associated with a Mohr-Coulomb (E_u*=100MPa and* v_u*=0.495*) failure criterion (modelled with the undrained C model in PLAXIS), while the flint is modelled with a M-C model with a non-porous behavior ($\varphi = 50°$, *c=4MPa, E=80GPa)*. A tension cut-off is applied to the flint material to specify the chosen tensile strength value, independently of the others parameters (otherwise the program automatically sets $\sigma_t = c \cdot cotg\varphi$). The main hypothesis is that the flint will break because of exceeding its tensile stress, as in a Brazilian test configuration.

First of all, a S_u of 300kPa for the chalk and a σ_t of 1500kPa for the flint are used and a vertical displacement is applied. Such values were selected among the lower bounds ones, to allow for avoid a solution where the flint remains unbroken, which will be treated in the next chapter. The obtained results, with the increasing failure mechanism are shown in *Figure 32*. The elements where the tensile cut-off is activated (i.e. the flint is "broken") are represented by white points.

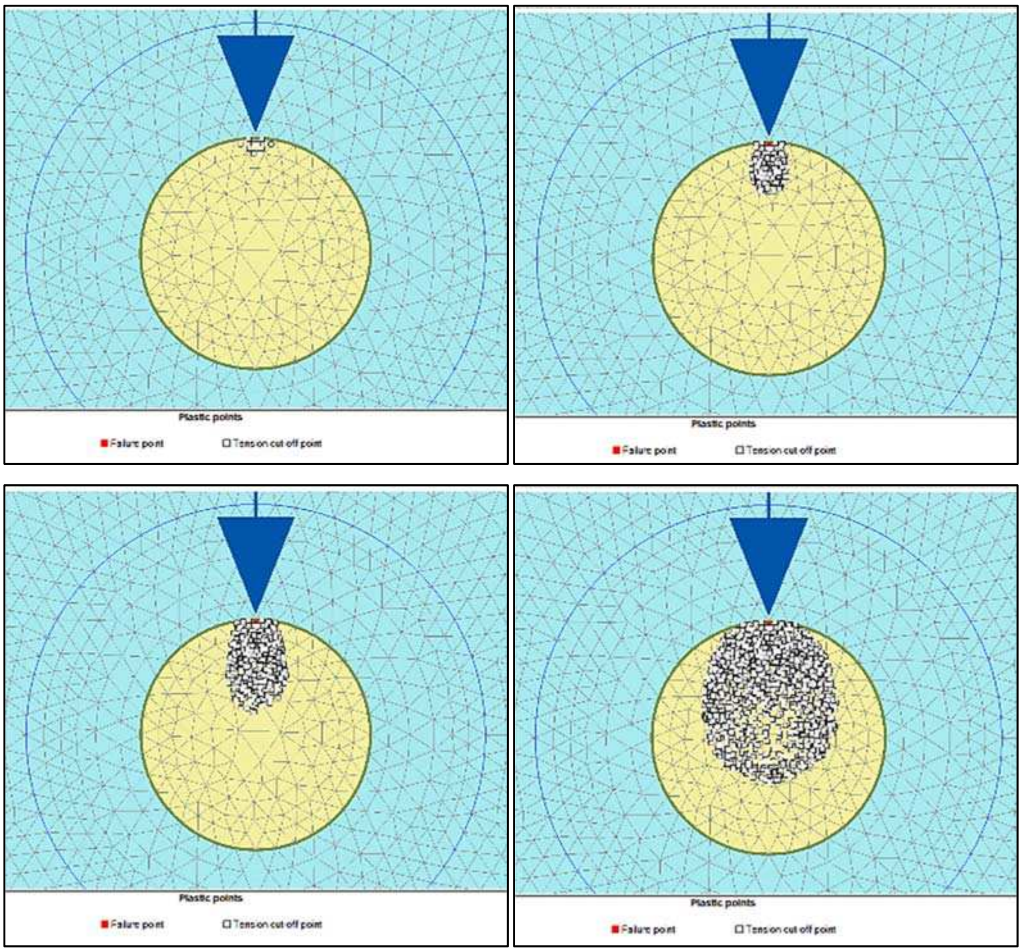

Figure 32. Progressive tension rupture of flint

The more the imposed displacement increases the more the points which reach the tensile strength increase, from top towards the center/bottom of the flint. The calculation does not converge anymore when all the points inside the flint reach the tension cut-off and so when the flint results completely fractured. This corresponds to a vertical displacement of about 5mm (i.e. a ratio to diameter of 2.5%) and to a force of 447kN. The force value resulting from the Brazilian test formula for this geometry is:

$$F = \sigma_t \, \pi \, d \, \frac{L}{2} = 1500 \cdot 3.14 \cdot 0.2 \cdot \frac{1}{2} = 471 \; kN \qquad 4.2$$

The two values of the final force are very similar (difference of about 5%), which is sufficient to benchmark the model for the purpose of this work. However, the failure mechanism is different because in the Brazilian test the load is applied punctually both on the top and on the bottom of the specimen; on the contrary, in this case the load is applied punctually only at the top while the reaction provided by the soil from the bottom is distributed. This can be understood from *Figure 33* where the directions of the compression and of the tension stresses are shown, which differs from that resulting from the Brazilian test configuration (*Figure 34*).

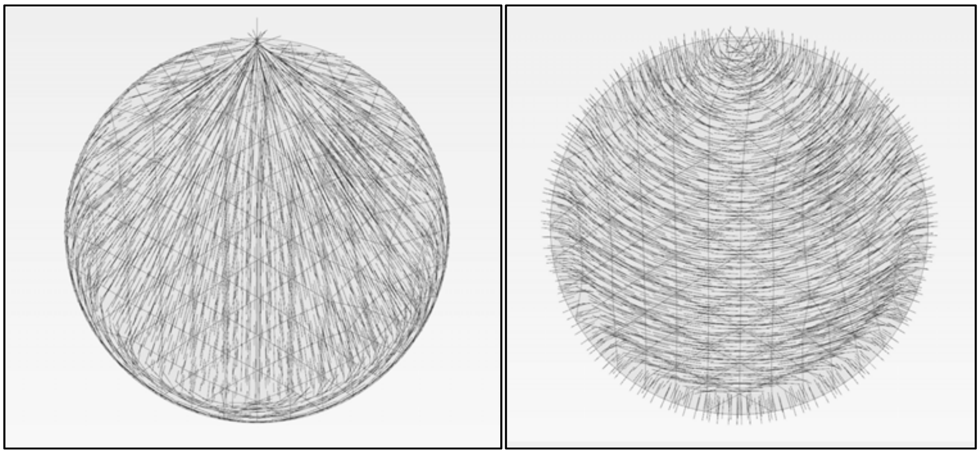

Figure 33. Compression (left) and tension (right) direction stresses

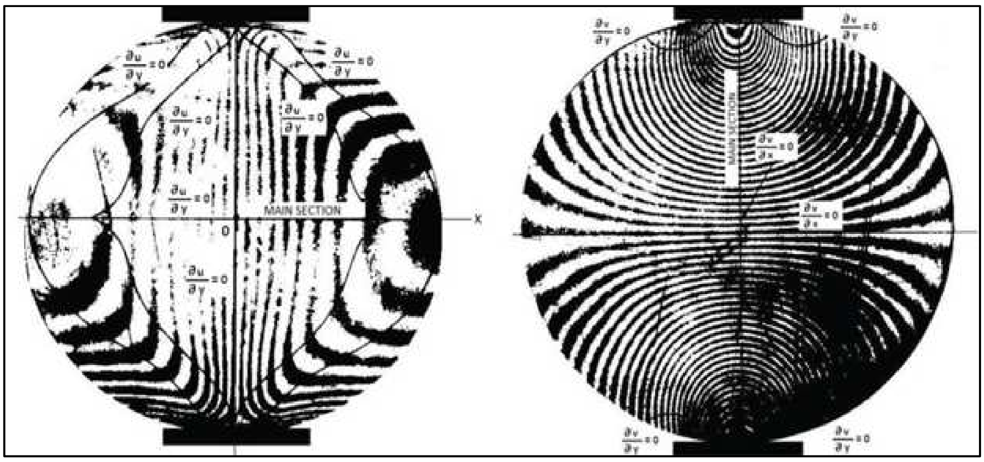

Figure 34. Compression and tension direction in diametral compression test (Durelli & Parks, 1967)

If the same numerical analysis is repeated a second time by setting a linear elastic model for the flint (i.e. infinite strength flint), the results shows a ductile behavior due to the plastic penetration of the flint within the soil. On the contrary, the first analysis has shown a brittle behaviour because of the tensile rupture of the flint. In *Figure 35* the load-displacements curves relative to the two previous investigated models are plotted. The red curve shows clearly a brittle failure, which is a characteristic of tensile breakage. Instead, the blue curve shows the reaching of a plateau, which is a characteristic of a plastic failure (this mechanism will be deeply analyzed in the following chapters).

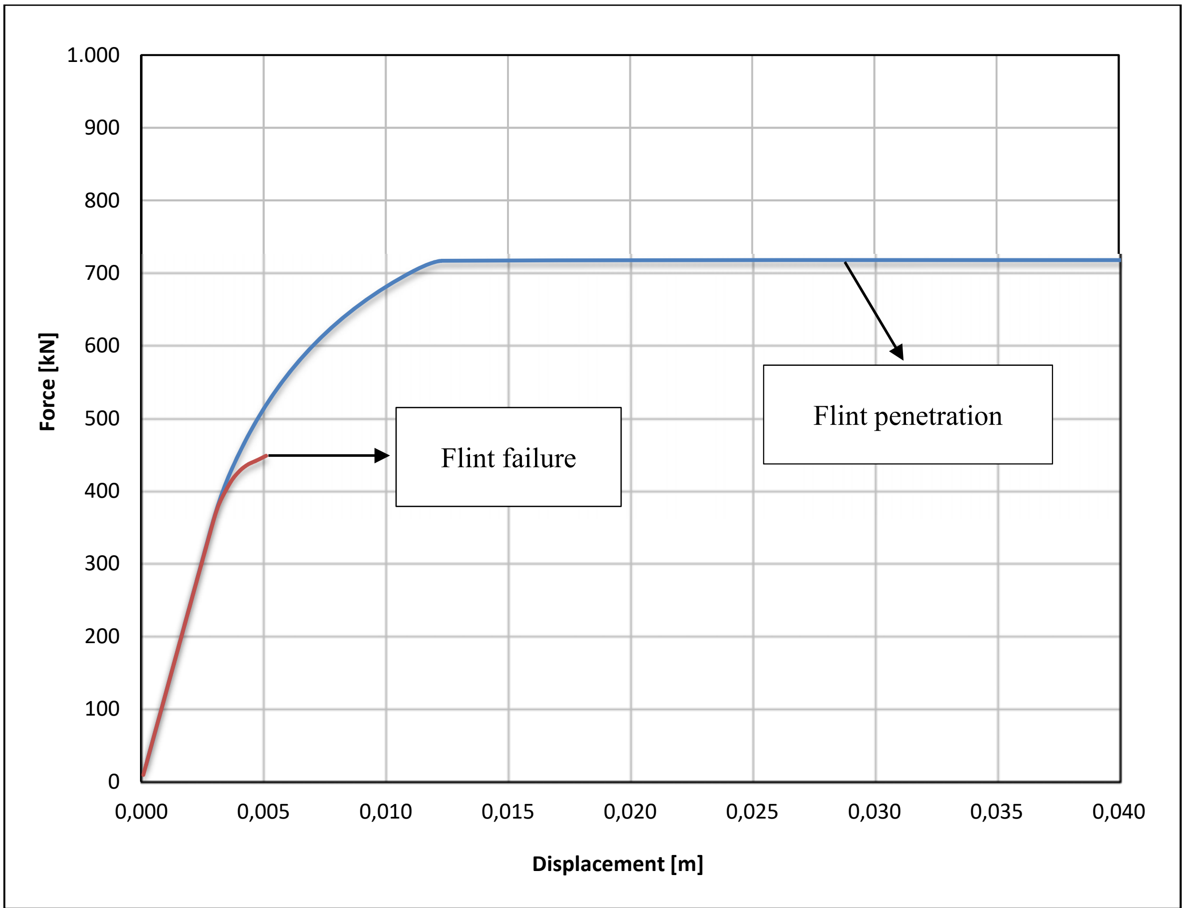

Figure 35. Brittle vs ductile behavior on load-displacements curve

The plastic points developed inside the two models, at the end of the calculations, are shown in *Figure 36-37*:

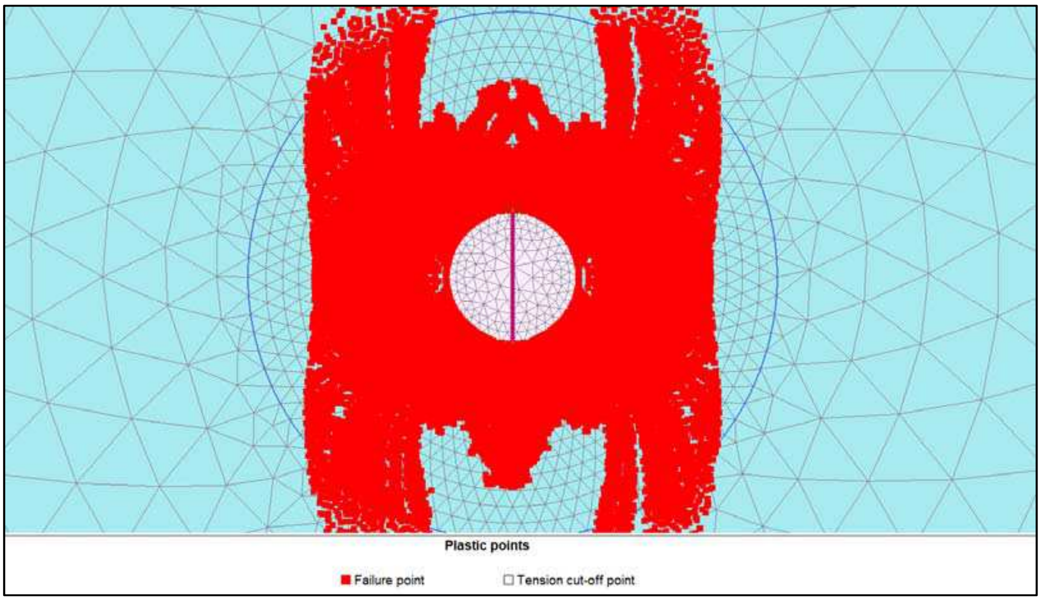

Figure 36. Plastic point with an infinite strength flint

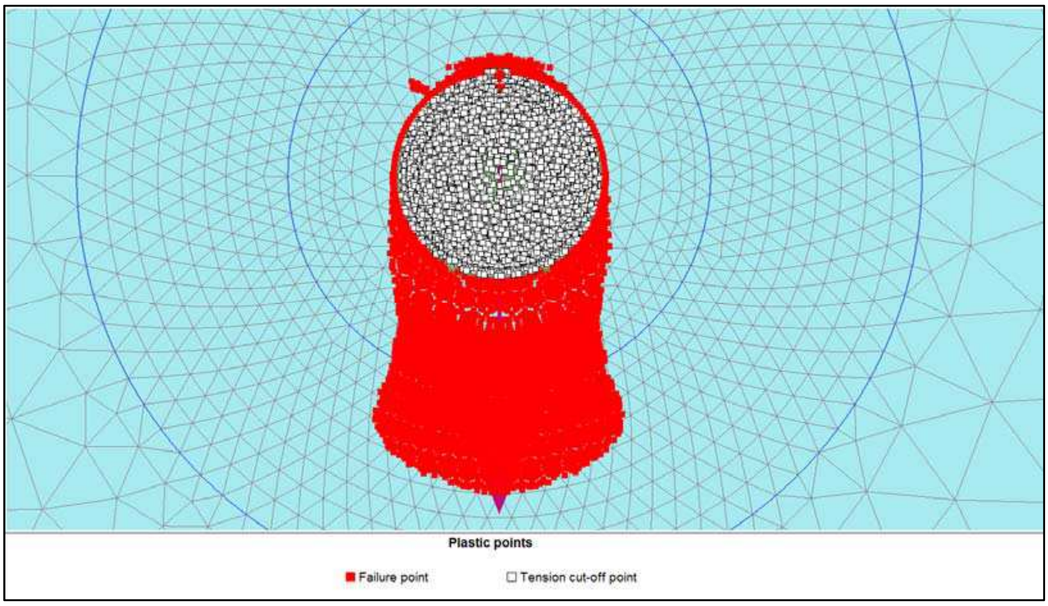

Figure 37. Plastic point with a low tensile strength flint

In *Figure 36* (infinite strength flint) it can be seen the soil flow development around the flint due to the bearing capacity failure: the embedding soil fails and the flint plastically penetrates inside it. On the other hand, in *Figure 37* all the points inside the flint reach the maximum tensile strength (tensile cut-off) and the soil under the flint experiences a little plasticization due to the reaction provided against the flint penetration: the flint fails and a negligible penetration occurs. If the strength of the soil was bigger, no plasticization would occur within it.

In conclusion, since in the cases analyzed the flint has a tensile strength much lower than his compression strength ($1/10$ to $1/25$ usually assumed in rock), probably the breakage will occur because of exceeding the tensile strength. This simple FEA shows that even if the failure mechanism results different, the final value of the force needed to break the flint is comparable with the one resulting from the Brazilian test configuration.

4.5 Flint displacement vs flint splitting

Since both flint displacement and flint splitting could occur during the pile interaction, it is interesting to understand what is the condition for which there is the transition from a soil bearing capacity failure to a flint tensile failure.

If the flint is embedded in a very soft formation, probably it will penetrate inside it when subjected to a force. On the contrary, if the soil is strong enough to provide a high reaction against the displacement of the flints, the tensile failure of the latter could occur.

Since the bearing capacity failure is governed by the undrained shear strength of the chalk and since the tensile failure is governed by the tensile strength of the flint, there will be a S_u/σ_t ratio which will separate the two failure conditions.

The bearing capacity failure force (in plane strain) can be obtained from the T-bar solution (see §5.2.2), assuming a unit length out of plane:

$$F_{lim} = 12 \ S_u \ d \tag{4.3}$$

The splitting force can be obtained from the Brazilian test equation (see §4.2), as well assuming a unit length out of plane:

$$F_{split} = \frac{\sigma_t \, \pi \, \mathrm{d}}{2} \tag{4.4}$$

As the two values shall be equal, the limiting ratio can be found as:

$$F_{lim} = F_{split} \rightarrow \frac{S_u}{\sigma_t} = \frac{\pi}{2 \cdot 12} = 0.13.$$

Thus, for $\frac{S_u}{\sigma_t} < 0.13$ the flint will be plastically displaced because its strength is sufficiently high respect to the chalk strength; on the contrary, for $\frac{S_u}{\sigma_t} > 0.13$ the flint will split and no plastic penetration will occur.

With the same numerical model of §4.4, a parametric analysis on the $\frac{S_u}{\sigma_t}$ ratio has been done in order to confirm this analytical finding. The results are reported in *Figure 38*, together with the theoretical values.

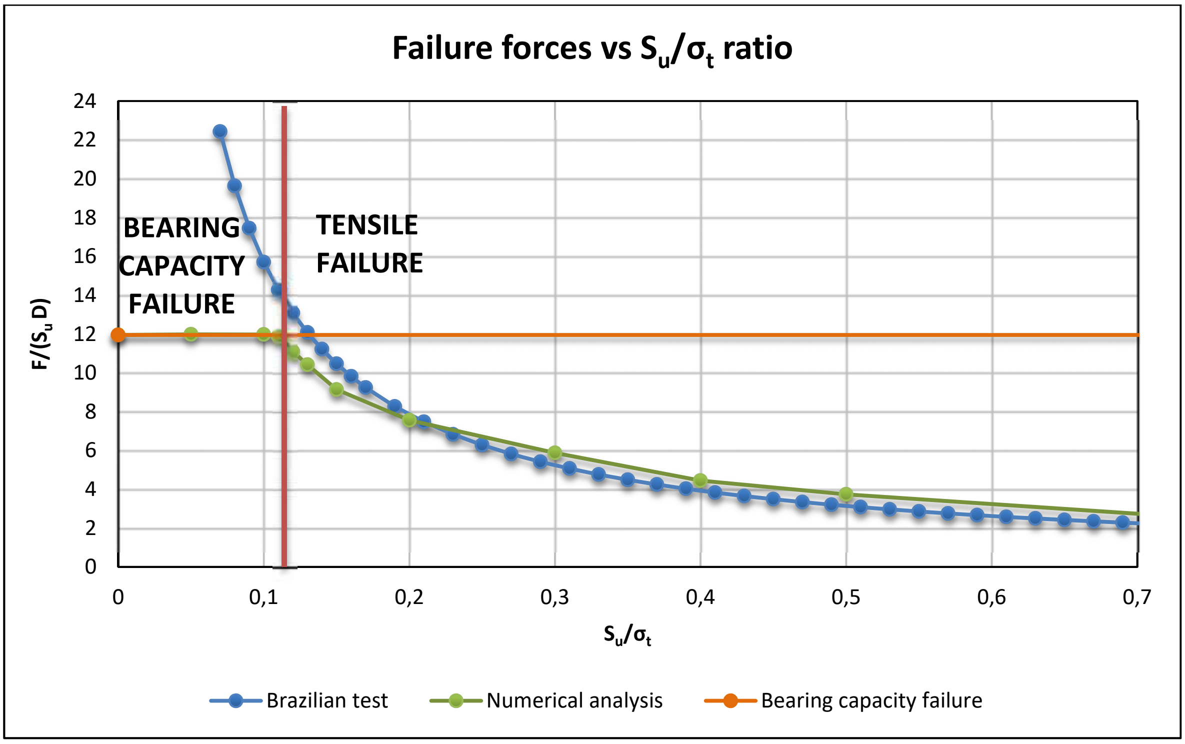

Figure 38. S_u/σ_t ratio vs failure forces-theoretical and numerical results

As it is shown in the graph above, the numerical values are in agreement with the analytical ones and the $\frac{S_u}{\sigma_t}$ ratio results equal to about 0.11, which is perfectly acceptable.

In conclusion, it is possible to affirm that if the S_u of the chalk is lower than about the 10% of the flint tensile strength, the flint probably will move through the chalk, otherwise it will break.

Since the UCS of the flint varies from 100 to 800MPa (see §2.3.4) and the tensile strength is about 1/25 to 1/10 of the UCS, tensile strength will vary from 4MPa (=100/25) to 32MPa (=800/25). The 10% of these values range thus from 400kPa to 3200kPa.

In a grade D chalk, usually the S_u rarely exceeds 500kPa (see §2.2.4, it is concluded that the main mechanism should be the bearing failure capacity. For this matter, in the next parts of this thesis the attention will be focused on the flint resistance to displacement/penetration.

5. Flint resistance to displacement: 2D static analyses

5.1 Introduction

The first approach to a complex problem should always start from a simplified model, in order to understand deeply the basic mechanisms before to advance. Therefore, in this chapter the interaction between the flint and the pile will be analyzed in a static way, even if during pile driving the pile tip applies to the boulder an impact load (i.e. dynamic). The flint will be modelled as a cylinder in plane strain condition, with an infinite stiffness and strength. In this way, it will be possible to understand the failure mechanism of a nodule subjected to forces and displacements with different positions and/or inclinations. Another advantage of static analysis is that the model may be validated, before being used for more complex analyses, thanks to some analytical solutions derived with the plasticity theory. The results will be in terms of horizontal and vertical forces required to produce a bearing capacity failure of a flint embedded in a softer formation (chalk, grade Dm) for different contact points.

5.2 Benchmarks

5.2.1 Validation of the model

The comparison of a numerical model with analytical solutions is a key aspect in the numerical studies. Muir (2004) in his book wrote: "*Before we embark on the analysis we should have some idea of what we expect to happen [...]. If the numerical analysis produces results which are initially counterintuitional then we should nevertheless be able to produce new back-of-the-envelope calculations to support what we have actually seen.*"

Thus, in order to affirm that the model results are correct regarding the behaviour of the system, it is necessary to establish a validation criterion that allows an objective quantification of the difference between the results and the reality. In fact, the main goal of a numerical method is to replicate as closely as possible the behaviour of the "real" world through numbers. The validity of these models is usually established by benchmarks comparison, in order to quantify the agreement between the predictions provided by the model and the real world represented by analytical solutions. One of the main problems of this technique is that it can only be used in simple cases, because usually it is not possible to find an analytical solution to the problem (as a matter of fact this is the reason of making numerical simulations). However, this technique is useful to validate the code of the numerical method, before doing more complex analyses (Jauregui & Silva, 2011).

5.2.2 T-bar penetrometer

The T-bar penetrometer was first introduced at the University of Western Australia in order to improve the accuracy of strength profiling in centrifuge model tests and was first used offshore in the late 1990s. The probe consists of a short cylindrical bar attached at right angles to the penetrometer rods, just below a load cell. It has two major advantages over the cone. Firstly, the load cell measures what is essentially a differential force (or net pressure) on the bar, so that minimal adjustment need be made for the overburden stress and ambient pore pressure. Secondly, the correlation between net pressure on the bar and the undrained shear strength of the soil is supported by an exact plasticity solution, with a potential range of "bar" factor of less than ± 10 per cent (due to different roughness of the bar surface), compared with cone factors that may vary from as low as 7 in sensitive clays, to over 17 a range of ± 40 per cent (Randolph & Gourvenec, 2011).

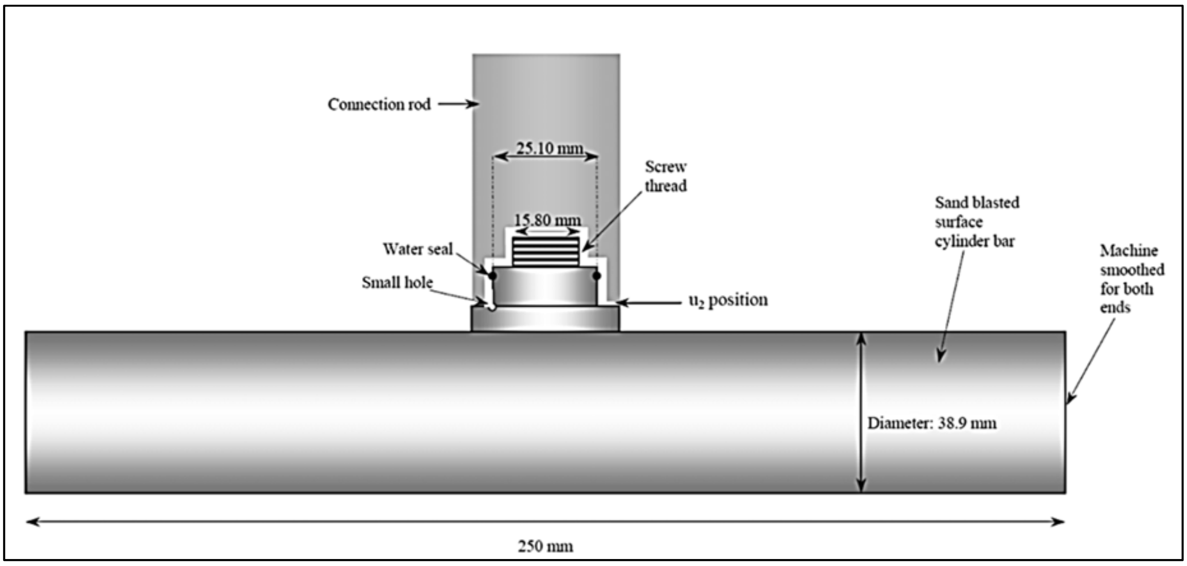

Figure 39. Diagram of T-bar penetrometer

As it is shown in *Figure 39*, the T-bar device is normally a 40mm-diameter cylinder, 250mm long attached to a shaft, with the penetration resistance measured behind the cylinder. This instrument can represent a circular flint modelled in plane strain conditions, loaded with a normal force applied in the center. If this assumption is done, the analytical solution of the T-bar can be used as a benchmark for a 2D plane strain numerical model. Thus, in undrained conditions the equation of the bearing capacity of a cylinder loaded by a normal force can be obtained by referring to the T-bar test equation (Randolph & Stewart, 1994):

$$N_{lim} = N_c \; S_u \; d \tag{5.1}$$

where N_c is a roughness factor, S_u the undrained shear strength of the embedding medium and d the diameter of the cylinder. N_{lim} obtained is the force needed to cause a complete full flow mechanism (bearing capacity failure).

5.2.3 Piles laterally loaded

If the boulder is loaded only with an in plane, normal force, the soil resistance is mobilized according to a flow-type mechanism. This failure mode has been already studied for laterally loaded piles (Randolph and Gourvenec, 2011) and it is represented in *Figure 40*:

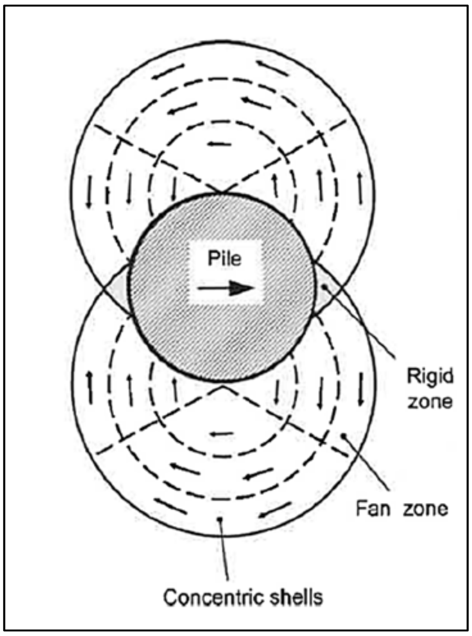

Figure 40. Flow around mechanism for deep lateral resistance (Randolph & Gourvenec, 2011)

If the soil is modelled as a perfectly plastic cohesive material then the calculation of this quantity reduces to a plane strain problem in plasticity theory, in which the load is calculated on a long cylinder which moves laterally through an infinite medium. By consequence, an exact calculation of the load on such a cylinder can be provided. Randolph and Housbly (1984) have derived the exact value of N_c by applying the classical plasticity theory, using both lower and upper bound solutions in a cohesive soil.

If this load is non-dimensionalized with respect to the soil strength and the diameter of the pile, is found that the load factor varies between 9.14 for a perfectly smooth pile and 11.94 for a perfectly roughly pile. The equation which governs the problem is:

$$N_{lim} = N_c \ S_u \ D \qquad 5.2$$

where D is the pile diameter. The form of this equation is equal to that used for the T-bar test (see eq. 5.1), since the problem is analyzed in the same way.

In conclusion, since the flint is modelled exactly as a pile laterally loaded or as a T-bar penetrometer, the numerical model may be validated with this simple equation, but only for a centered force. Then, the validated model will be used for more complex analyses (e.g. inclined forces).

5.3 Plane strain model

5.3.1 Introduction

The first analyses carried out ("Inclined force" model, see §5.4) are aimed at understanding the mechanical behavior of a circular flint loaded by an inclined force (normal and tangential components) at a fixed point; a failure envelope on the T-N (tangential-normal) plane will be then provided.

In a second stage ("Vertical displacements" model, see §5.5) the flint will be subjected to a pure vertical displacement, with the horizontal one fixed. The application point is varied and horizontal and vertical forces are found. This condition represents in a better way the action of the pile on the boulder.

Finally, a pile sheet is modelled ("Vertical displacements with pile" model, see §5.6) constrained to some horizontal springs, in order to simulate the circular stiffness of the pile in plane conditions. The forces acting on the pile can be obtained from the numerical model.

In the following sub-chapters, a detailed overview of the numerical models used is presented.

5.3.2 Geometry

The commercial finite element software used for the analysis is PLAXIS 2D.

The problem is modelled in a plane strain condition imposing a uniform state of stress (σ_1= σ_3=400 kPa). The dimension of the model is 10x10m, with 4 hinges at the corners and rollers on the sides as boundary conditions.

The nodule has a circular geometry (generated with the tunnel command) with a 0.2m-diameter (as already mentioned in Chapter 4, also the case of the 2m-diameter has been analyzed, with the same results) and it is located at the center of the model, so it is completely embedded in the soil.

The pile wall (only in "Vertical displacements with pile" model) is modelled as a steel plate element with a thickness of 70 mm. Horizontal springs are added as a fixed-end anchors in order to simulate the circular stiffness of the pile.

5.3.3 Mesh

Around the flint the mesh is refined by adding a series of polycurves to achieve the best quality of the finite elements. This procedure allows to refine the mesh only where high strain gradients are expected. In this way, the final number of elements will be lower while maintaining the same accuracy and by consequence the computational time will be reduced. In *Figure 41* the model mesh quality is shown.

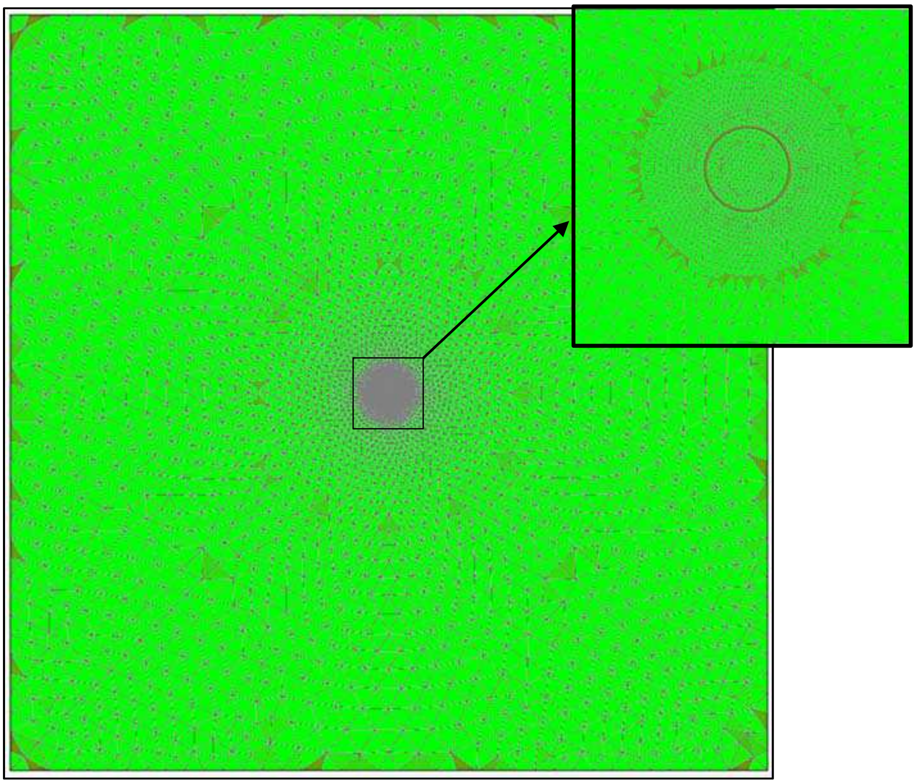

Figure 41. Mesh quality PLAXIS model

Multiple mesh densities have been investigated with a sensitivity analysis in order to find a good compromise between quality of the results and time consuming. Additional information is provided in *Table 6*:

Table 6. Mesh information

Model	Plane strain
Elements	15-noded
Nr of soil elements	20210
Nr of nodes	162529
Average element size	0.1014m
Maximum element size	0.2004m
Minimum element size	0.01054

The model size is chosen 50 times the flint diameter to ensure that the failure mechanism could develop within the soil model. However, this dimension could be reduced in order to decrease the computational time in more complex analyses (e.g. dynamic, see §7).

5.3.4 Soil model

A unique, uniform, homogeneous and isotropic soil is considered. The material model used for the chalk is a Guest -Tresca model with the following parameters (*Table 7*):

Table 7. Mohr-Coulomb parameters

S_u	100kPa
E_u	0,1GPa
ν_u	0,495

A total stress analysis is carried out, in which stiffness and strength are defined in terms of undrained properties. Excess of pore pressure are not explicitly calculated, but are included in the effective stresses (Undrained C in PLAXIS).

The properties of the chalk are chosen on the basis of a literature review presented in Chapter 2. As a consequence of undrained conditions, no elastic volumetric strains occur, and thus Poisson's ratio should be assumed to remain 0.5 throughout shearing. However, it is assumed equal to 0.495 for computational purposes, in order to avoid singularity in the stiffness matrix. Since all the results will be normalized with respect to the S_u, an average value of 100kPa is chosen.

The unit soil weight is not considered because, in this phase of the study, the initial stresses are generated by imposing a uniform field stress in all the model ($\sigma_1 = \sigma_3 = 400kPa$) and are not affecting the results in undrained conditions with constant S_u.

The flint was modelled as a linear elastic (infinite strength) non-porous material, with an elastic stiffness modulus of 80GPa (see §2.3.4). As the modulus is 800 times bigger than the chalk, flint can be considered as an infinite stiffness material.

Between the flint and the surrounding soil an interface is added in order to allow concentrated relative displacements between the two adjacent different materials. A sensitivity analysis is performed on the R_{inter} parameter in order to evaluate its influence. Three values are explored: 1 (fully rough), 0.75, 0.5.

5.3.5 Pile properties

In the 2D plane strain model a pile sheet of 5 m is modelled (*Figure 42*) by using plate elements, to simulate the presence of the pile. A linear elastic material is assigned with the typical steel parameters: Young's modulus E=210GPa and Poisson's ratio v=0.2. The thickness of the plate is assumed 70 mm and with this value the normal and the flexural stiffness can be calculated. Moreover, in order to simulate the circular stiffness of the pile, some springs (calibrated with a 3D model) are added to the model as fixed-end anchors (see §5.6). In this way the horizontal displacements of the wall during the advancement should agree with the real 3D geometry of the problem. The interface between the pile and the soil is considered smooth because for this type of analysis the shaft friction is not of interest.

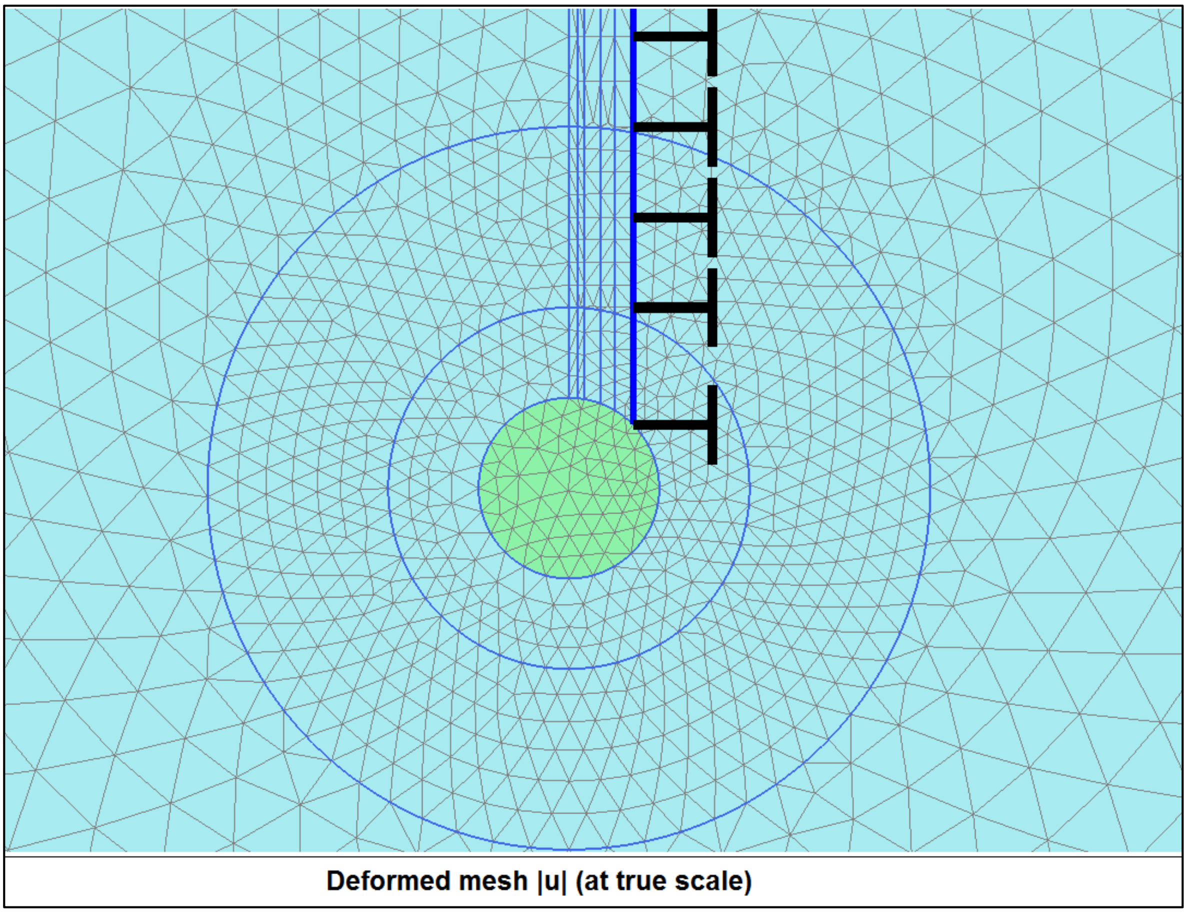

Figure 42. Pile-flint PLAXIS plane-strain model

5.4 Inclined forces

The flint is firstly approximate to a cylinder loaded in plane strain condition. In this way the closed-form solutions of laterally loaded piles and of T-bar can be used to have analytical formulas for the validation of the following numerical model. The analytical solution shows that N_c is dependent on the surface roughness α_R, which can vary between 0 (fully smooth) and 1 (fully rough), as is shown in *Table 8:*

Table 8. Analytical values of N_c for different roughness (Randolph & Houlsby, 1984)

	smooth		rough
α_R	0	0.5	1
Nc	9.142	10.82	11.94

On the contrary, if the cylinder is loaded only by a tangential force, the failure occurs in a rotational-sliding mode along the flint-soil interface. The limiting force is found by assuming the shear stress along the contact surface (assumed equal to a portion of S_u, i.e. adhesion factor equal to 0.5 and 1.0) completely mobilized at the interface and by integrating the tangential stresses all along the perimeter. As a result of this:

$$T_{lim} = \pi \ d \ \alpha_R \ S_u \tag{5.3}$$

Relying on these solutions, the goal is to combine the normal and the tangential force for providing a failure envelope, which shows the interaction between these two components. First of all, the diagram is built using the analytical solutions previously exposed and assuming a linear relationship. In *Figure 43* are reported two theoretical predicted failure envelopes for two different surface roughness.

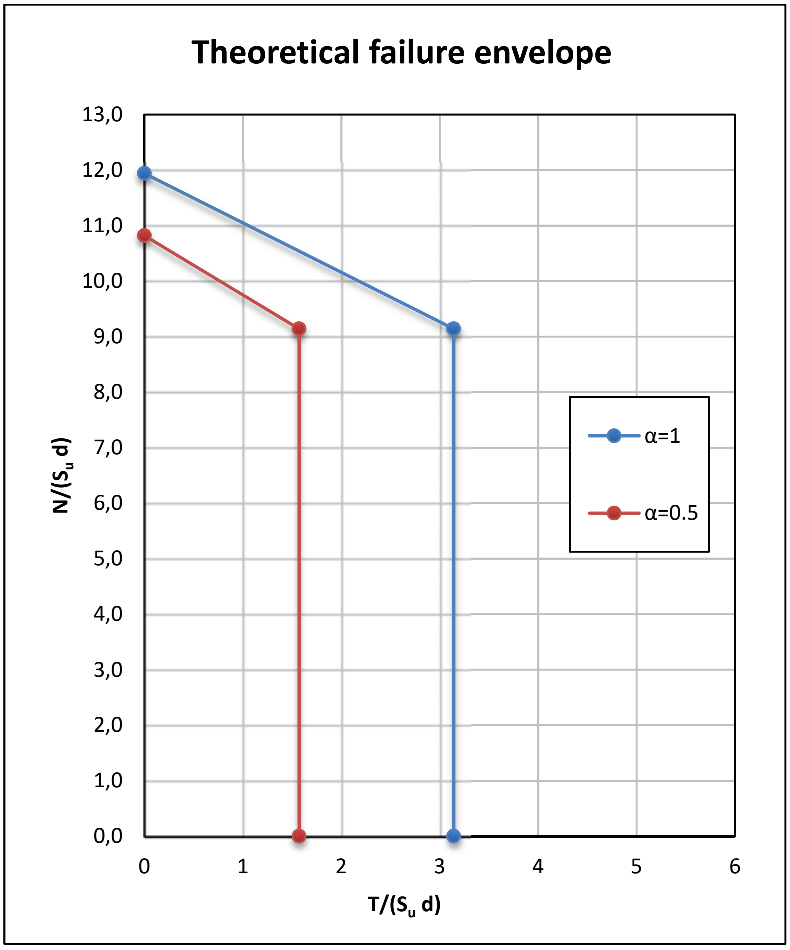

Figure 43. Theoretical failure envelope

The normal force gradually decreases the more the tangential force increases. The phenomenon is treated similarly to the bearing capacity of a direct foundation where the ultimate vertical pressure (N in this case) is reduced by an inclination factor (Vesic, 1975) which takes into account the horizontal component (T in this case).

The force N decreases until it reaches a lower limit, which is equal to N_{lim} calculated for a fully smooth pile (N_c=9.14). Indeed, the pile became "virtually" smoother the more than the tangential force is increased, because this latter force mobilizes a quote of available S_u. Before reaching the T_{lim}, a bearing capacity failure with a flow-type mechanism will occur. On the contrary, when T_{lim} is reached, a rotational-sliding mechanism prevails and the T become independent from the N.

This diagram has to be validated with finite element analyses, to see if the results of the numerical simulations are in agreement or not with the analytical prediction.

Initially an infinite strength and stiffness cylinder embedded in a clay is modelled, with the parameters previously described. The analysis is carried out considering a plane strain condition and an undrained behaviour. A parametric calculation is done in order to change gradually the inclination of the force and to plot all the domain, as it is shown for on case in *Figure 44*:

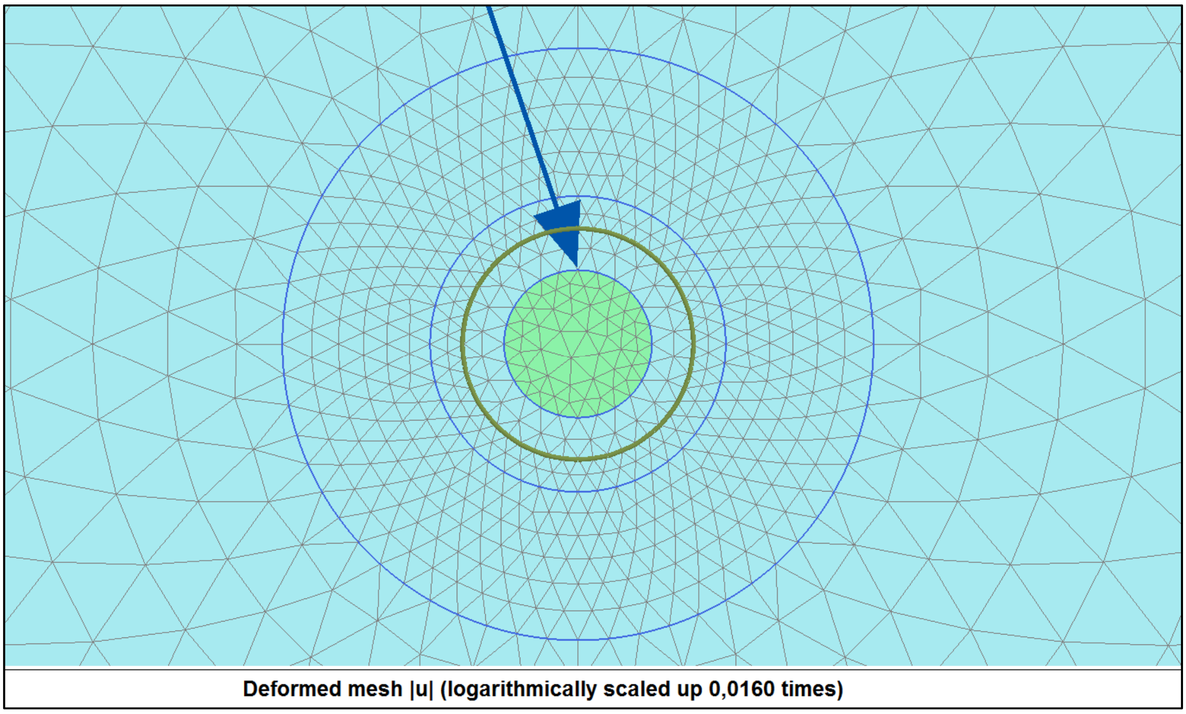

Figure 44. Inclined force in PLAXIS model

So, in each calculation phase of the analysis, the horizontal component is increased by keeping constant the vertical one (500kN); this means that the force is progressively inclined since the horizontal component is summed to the constant vertical one. The input values are high to ensure the full development of the failure mechanism. A typical load-displacement curve presents an initial linear part followed by a non-linear shape and finally a plateau, which correspond to the formation of a complete failure mechanism (Nicolini & Castelletti, 2017), as is shown in *Figure 45* for one of the cases.

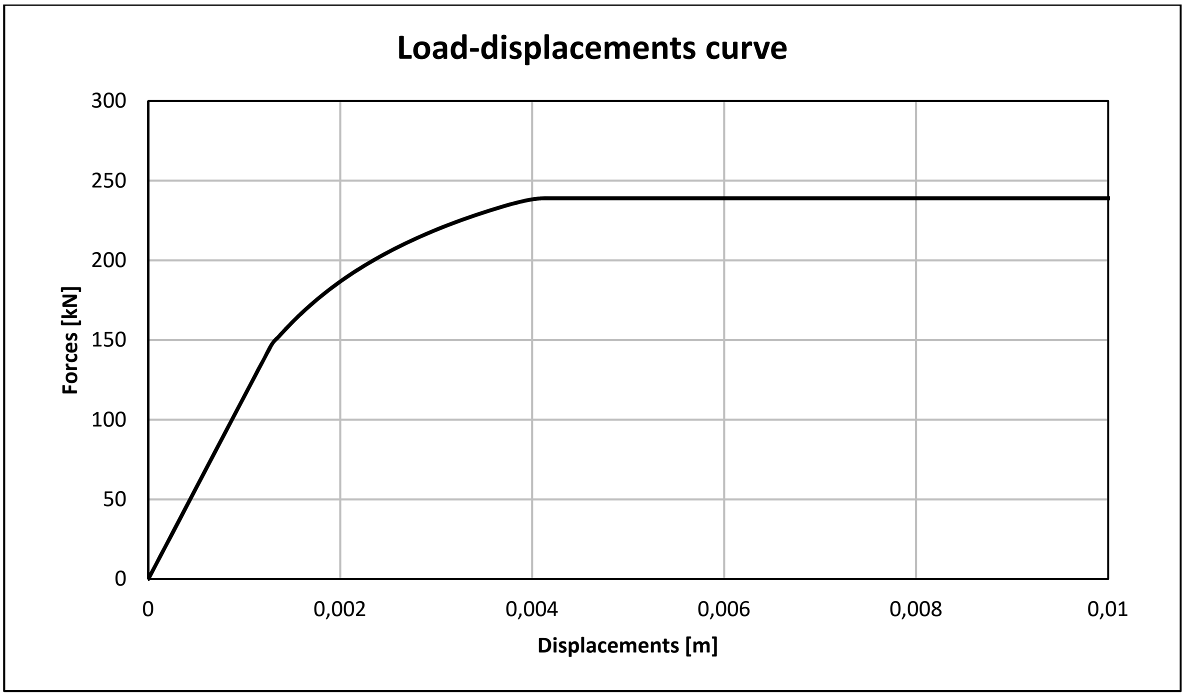

Figure 45. Load-displacements curve

On the y-axis the value of the resulting force of the calculation phase is plotted. In this reported case, only a vertical force of 500kN was applied and the multiplier obtained is 0.479. So the resulting force is:

$$F_{v,lim} = 0.479 \cdot 500 = 239.5\ kN$$

In order to validate the model, this force can be compared with the one resulting from the T-Bar equation, as explained before (see eq. 5.1):

$$N_{lim} = N_c\ S_u\ d = 11.95 \cdot 100 \cdot 0.2 = 239.0\ kN$$

The resulting forces are very similar except for small numerical approximations, so the model can be used to predict inclined limit forces for which there are no analytical solutions. *Figure 46* shows the total displacements ($|u|$) for a vertical force, with an evident flow mechanism developed.

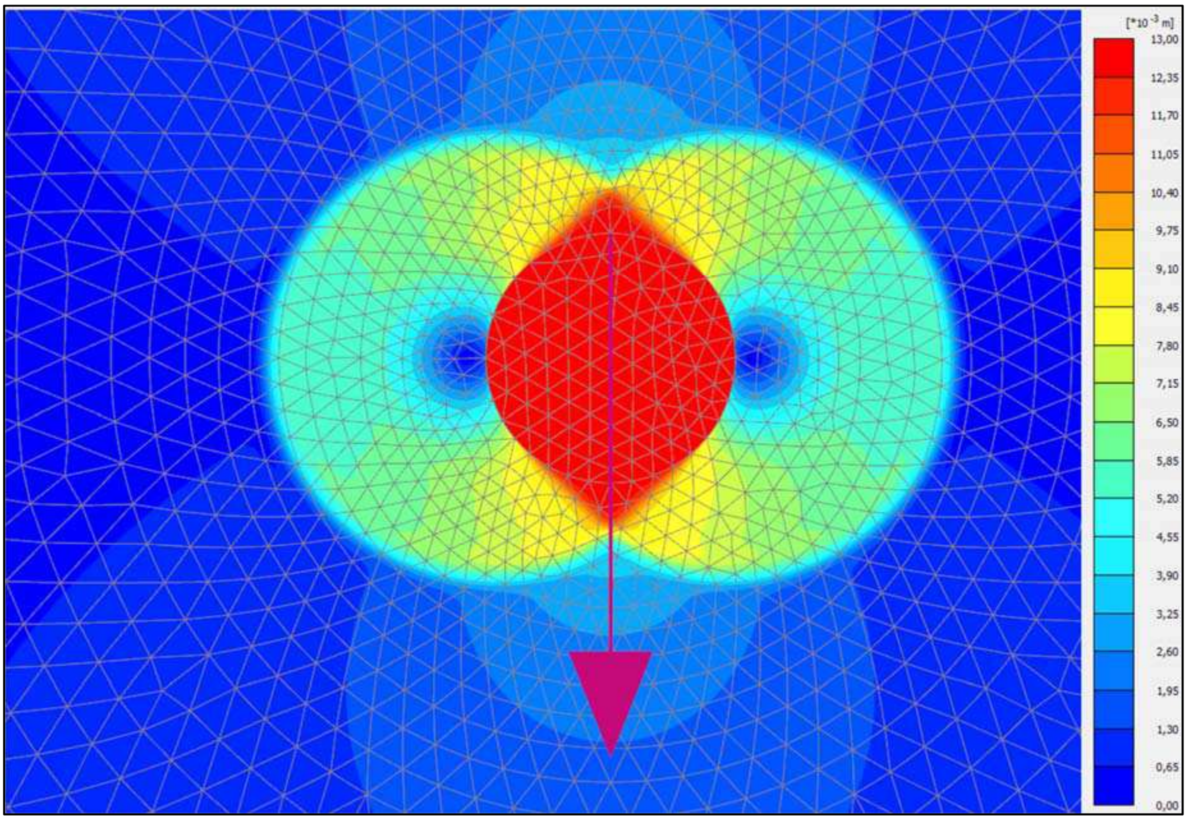

Figure 46. Total displacement of flow mechanism

The force reached on the plateau can be used to define a point on the failure envelope. By repeating this procedure for different inclinations the whole domain is built. On the domain the forces are reported normalized as follow:

$$N_{norm} = \frac{N}{S_u \ d} \tag{5.4}$$

$$T_{norm} = \frac{T}{S_u \ d} \tag{5.5}$$

A parametric analysis was performed in order to identify the influence of α_R factor. The three failure envelopes are shown in *Figure 47*, compared with the analytical ones.

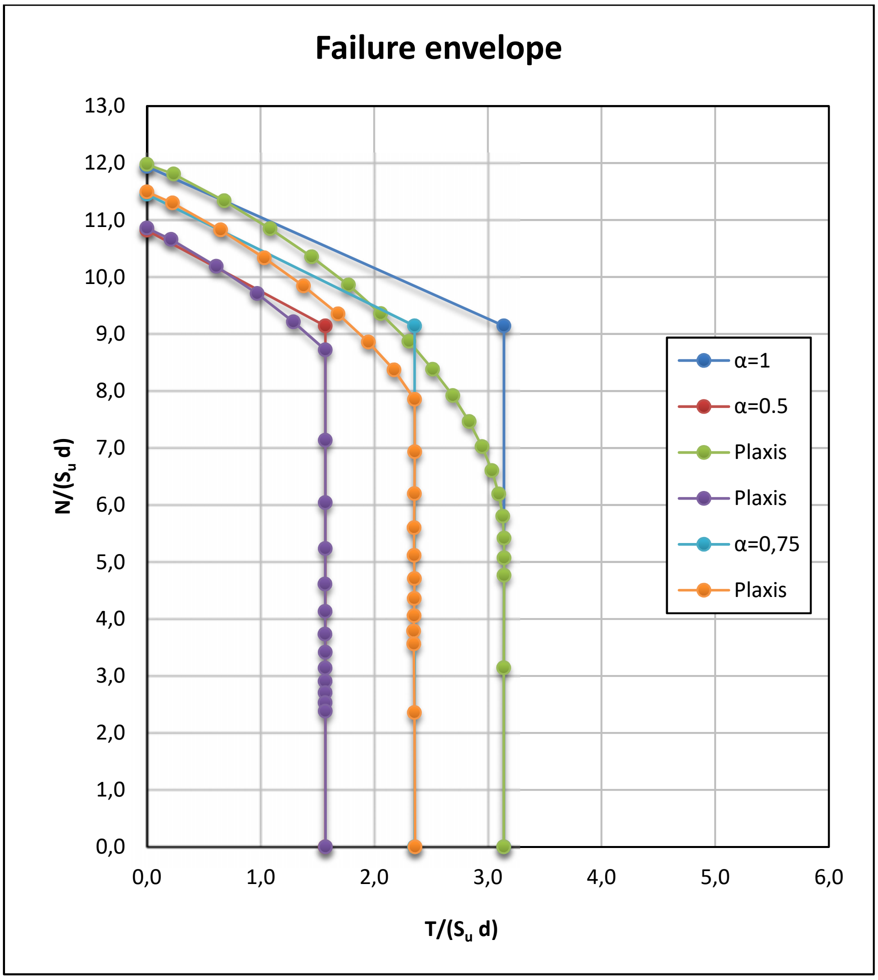

Figure 47. Numerical failure envelope

The numerical envelopes have a shape which is in agreement with other failure envelopes already provided by some authors for similar problems (Randolph, 2016). However, from this chart it is evident how the numerical data differ from the analytical predictions, the more that the roughness increases. The difference could be explained because the analytical envelope considers independent the bearing capacity failure and the rotational-sliding failure; as a matter of fact, until the T_{lim} is reached the rotation of the flint is not taken into account. Actually, the flint moves and rotates at the same time and, since the kinematism is roto-translational, it is not rigorous to consider independent the two mechanisms. However, if the roughness is reduced, the numerical diagram becomes more similar to the analytical one; this means that the more the flint is smooth the more the transition from the translational to the rotational failure mode is accentuated.

Figure 48 shows a roto-translational mechanism due to the application of an inclined force, by representing the total displacements vectors.

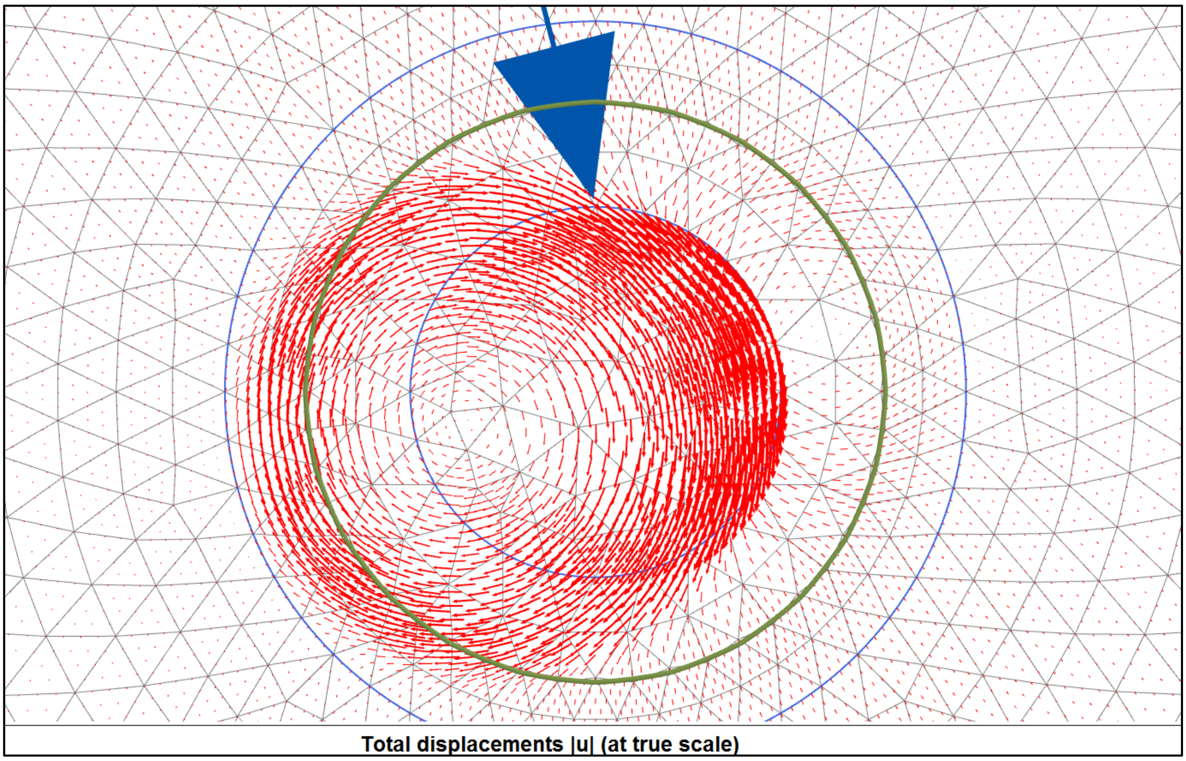

Figure 48. Total displacements vectors for inclined force

Thanks to the obtained diagram is possible to find the combination of normal and tangential forces that cause the failure (penetration or rotation) of an infinite strength and stiffness cylinder embedded in a softer soil in undrained conditions.

Since the pile is generally driven vertical, it could seem useless to investigate the behavior of a flint under an inclined force. However, since a homogeneous and isotropic soil and a circular flint are considered, there is an equivalence between an inclined and a vertical force, as it is clarified in *Figure 49*. The point of application is defined by the angle in the center, as indicated in the right flint.

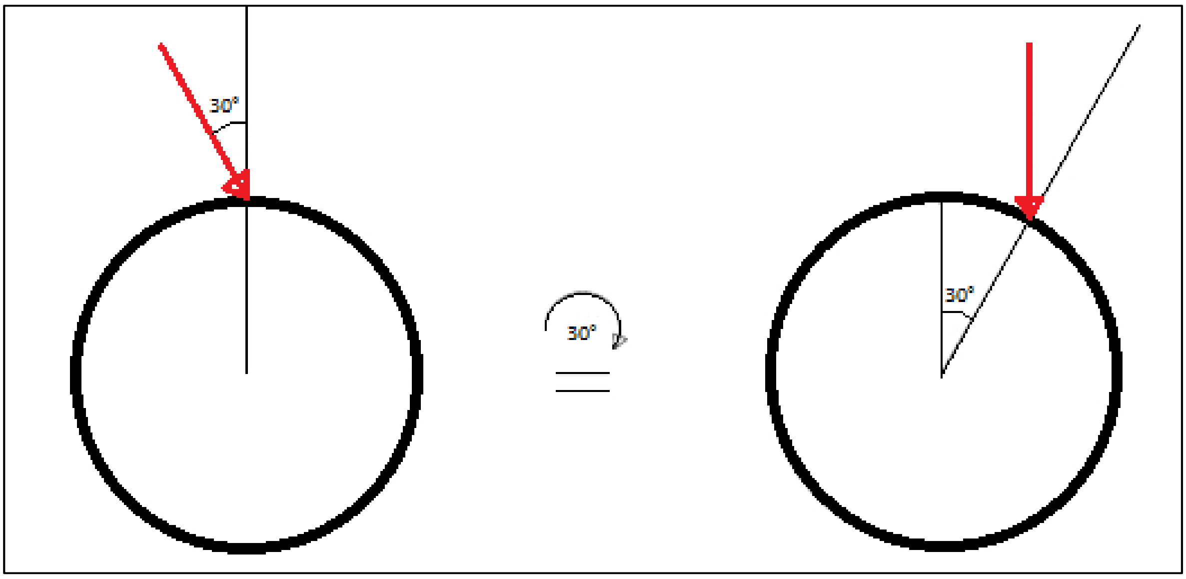

Figure 49. Equivalence between inclined and vertical force

Thus, if the vertical force (on the right in *Figure 49*) is decomposed in normal and tangential components, it is possible to use the same domain previously reported (*Figure 47*); instead, for a centered force the normal and tangential directions are equal to the vertical and horizontal ones.

Moreover, in order to find the combination of N and T which causes failure for a vertical force applied laterally, it is necessary to calculate the complementary center angle and to draw a line with that slope on the envelope. The intersection with the failure curve returns N and T normalized. By multiplying for the resistance and the diameter and by decomposing, it is possible to get the static vertical force needed to cause failure, as it is exemplified in *Figure 50* for a 10° inclination.

For angles bigger than 30° for an α_R=1, the normalized tangential component T remains constant (it is independent from the normal component) and by consequence the vertical force can be easily find by dividing π for the sine of the angle considered, and then by multiplying for the diameter and the S_u:

$$for\ \alpha > 30° \rightarrow \ \ F_{v,lim} = \frac{\pi}{\sin(\alpha)} d\ S_u$$

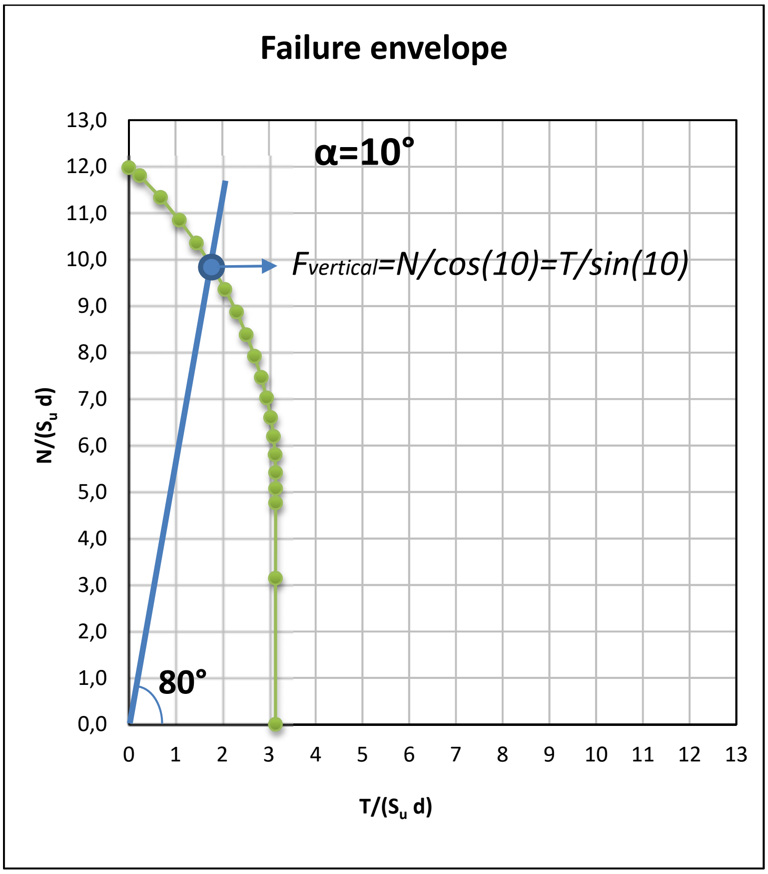

Figure 50. Graphical procedure for the determination of N and T for α=10°

In conclusion, it is demonstrated that the more the flint is hit laterally, the more the reacting vertical force is low. Moreover, for α_R=1 at 30° the failure mechanism passes from a bearing capacity to a rotational mode; for smoother interfaces (α_R<1), this transition occurs for lower angles.

5.5 Vertical displacements

Since a driven pile advances vertically except for small radial strains (because steel piles are open-ended and so the thin wall can experience deformations), it is interesting to explore what happens to a flint subjected to a pure vertical displacement, with the horizontal one fixed. In fact, it can be assumed as a first approximation that the pile does not deform when it hits an obstruction. By consequence, at the contact point it will be applied a pure vertical displacement or equally a force but with a horizontal constraint (vertical roller).

A parametric analysis is performed in order to investigate the different flint behaviours by changing at each phase the contact point, as it is shown in *Figure 51*.

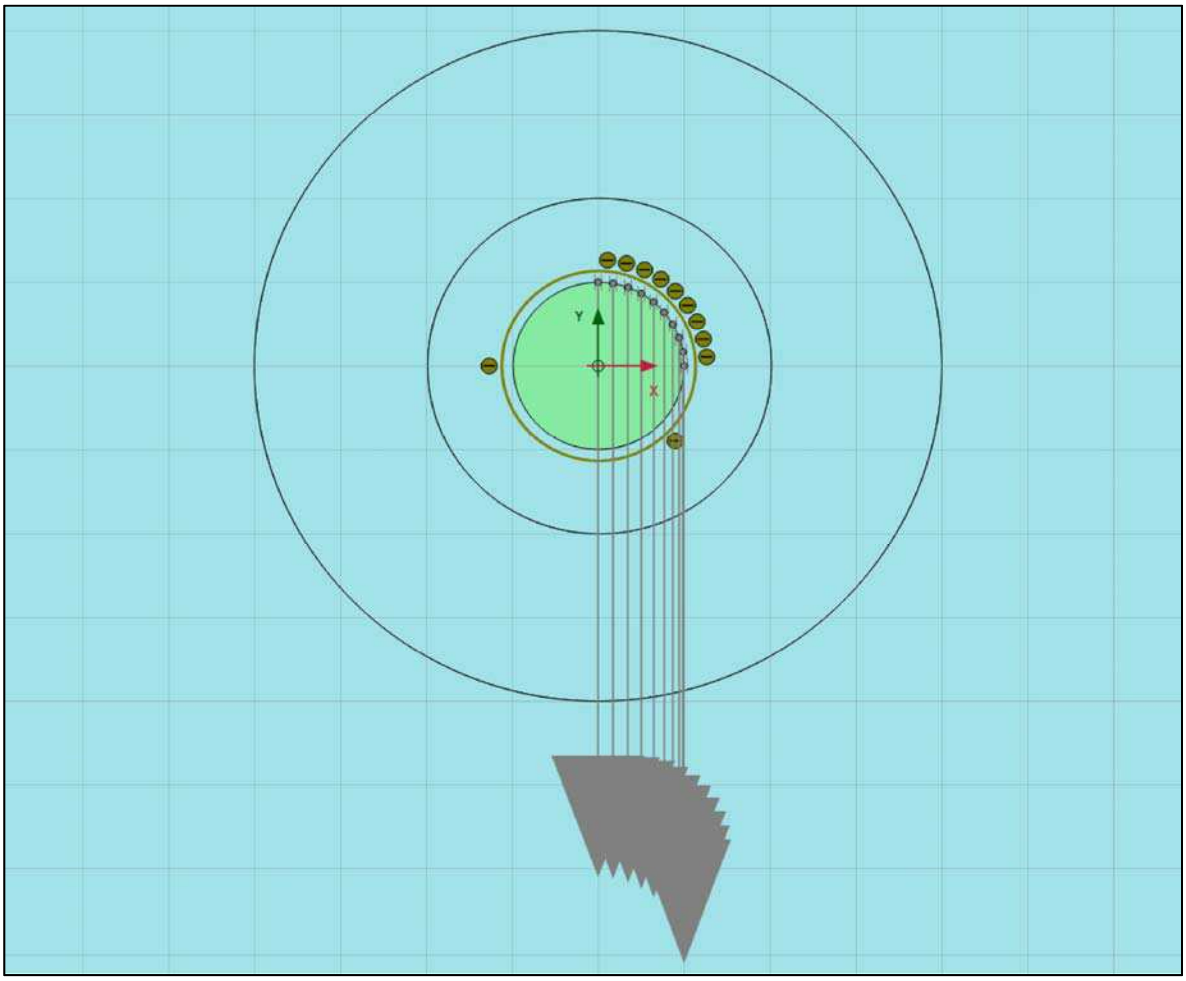

Figure 51. Vertical displacements PLAXIS model

A vertical displacement of 0.2 meters is imposed and a load-displacements curve is found as an output, both for the vertical and horizontal force. At each phase the point displacement is moved of 10°. Thus, for each angle two forces are extracted from the curve plateau. In *Figure 52* are reported the vertical force F_y, the horizontal force F_x and the vectorial sum $F_{inclined}$ obtained for a 0.2-meter diameter flint. The ones obtained for a 2m-diameter boulder are not reported in the text but they result exactly scaled by a factor of 10.

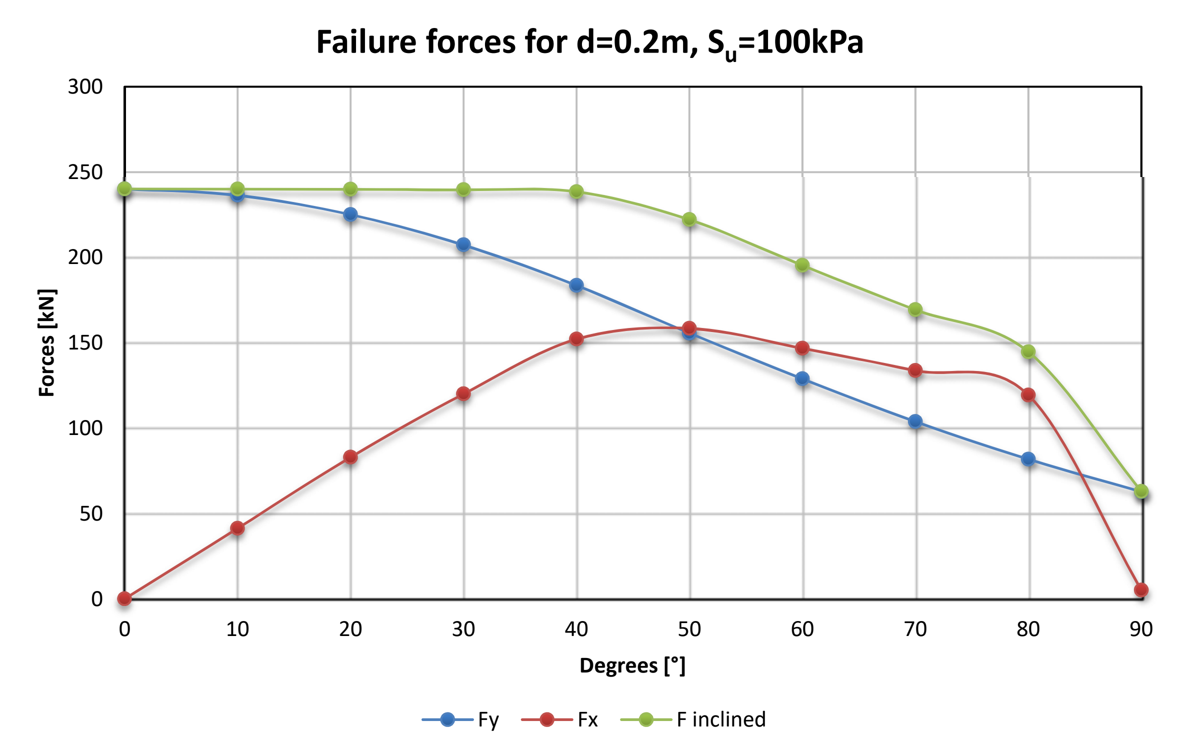

Figure 52. Resulting failure forces for different angles (imposed vertical displacement)

The kinematism is completely different from that obtained by applying a force because now the contact point can move only vertically; on the contrary, by applying a force the point could move freely.

Until about 45°, the more the displacement is applied laterally the more the vertical force decreases and by contrast the horizontal one increases. This means that if the pile hits the flint perfectly in the center, a high vertical force will arise. On the other hand, if the pile hits the flint laterally, the vertical force will be lower while a higher horizontal force will originate. After 45°, the two forces decrease simultaneously, thus the stress condition on the pile becomes less dangerous.

It is interesting that until 40° the resulting force $F_{inclined}$ does not change and it is equal to N_{lim} calculated in the previous chapter for a centered force (see §5.4). This means that until 40° no tangential force arises because the $F_{inclined}$ is inclined exactly of the corresponding angle in the center. Instead, beyond 40° the $F_{inclined}$ has a different inclination because of the arising of the tangential component. *Figure 53* clarifies this concept.

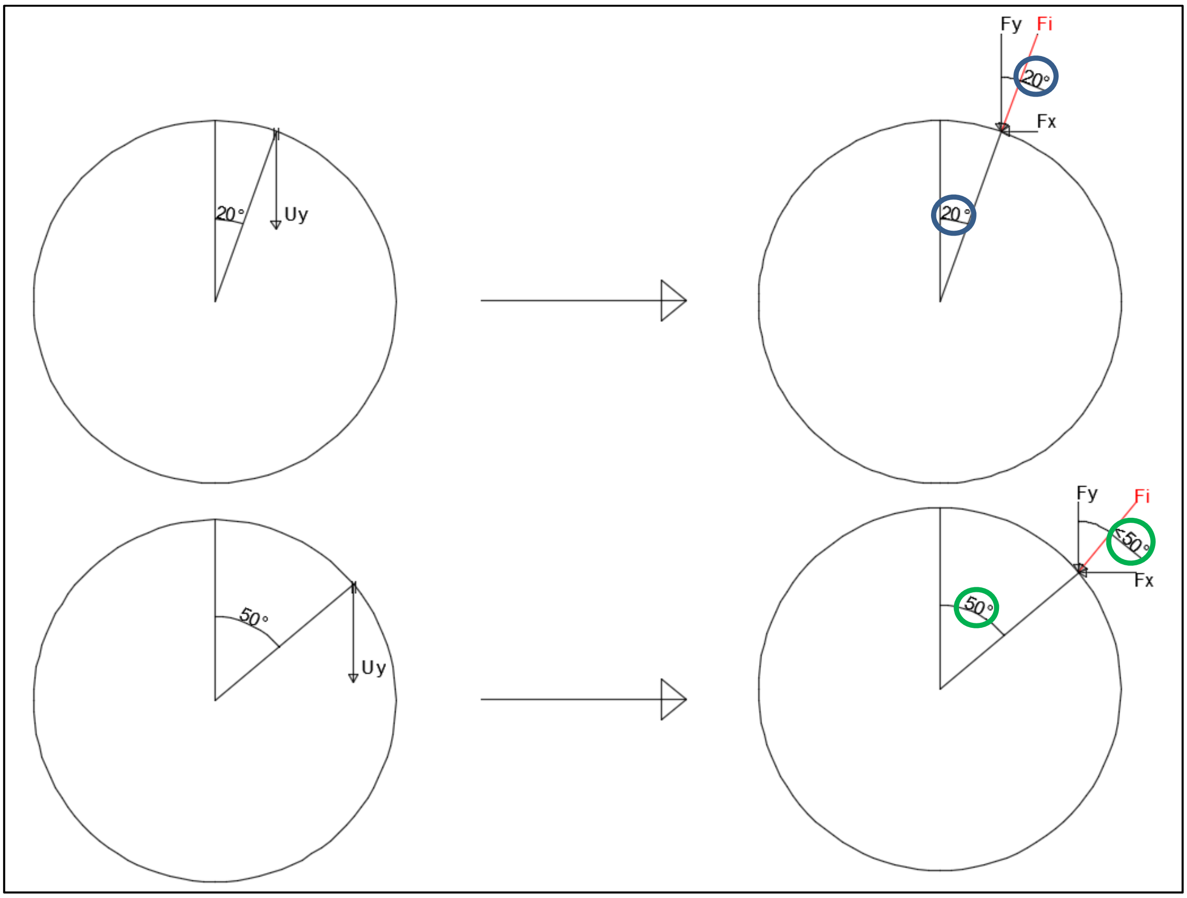

Figure 53. Inclination of resulting force for 20° and 50°

Thus, with a low angle (less than 40°), the failure mechanism will be for bearing capacity with a slight rotation in order to maintain the kinematic compatibility. After exceeding the 40° the mechanism becomes gradually rotational. *Figure 54* shows the total displacements for different angles (0°, 20°, 40°, 70°); the differences between the failure mechanisms are clearly appreciable.

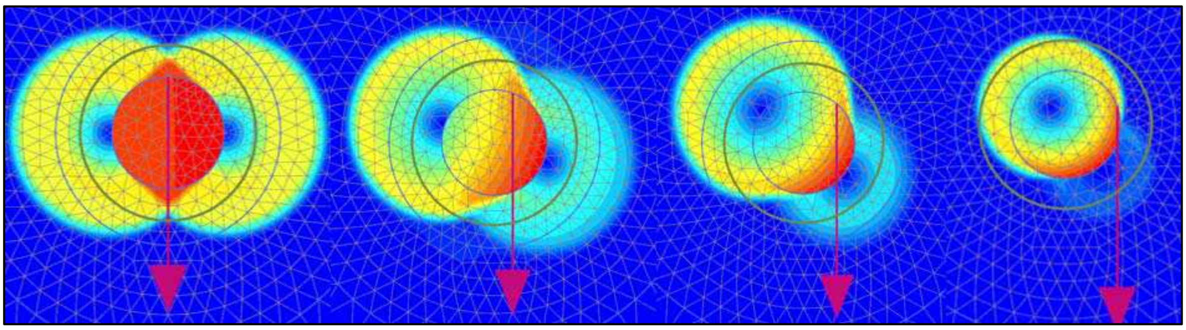

Figure 54. Failure mechanism for 0°, 20°, 40°, 70°

It is now possible to project these resulting forces on the normal and the tangential direction, in order to obtain a failure envelope (*Figure 55*) as already done in the previous chapter (see §5.4).

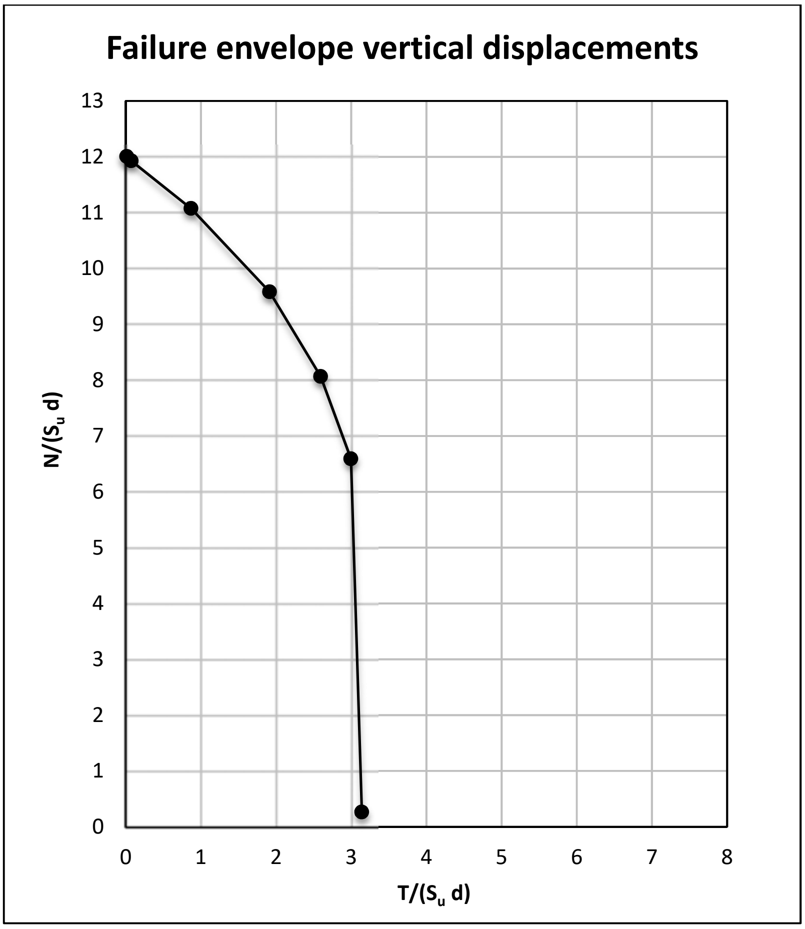

Figure 55. Failure envelope for vertical displacements model

It is remarkable that the envelope shape is similar to the one created by applying a force (see *Figure 47*). However, conceptually it is completely different because until 40° points are placed only at T=0; differently, on the other envelope points were more equally distributed along the curve. *Figure 56* clarifies this concept.

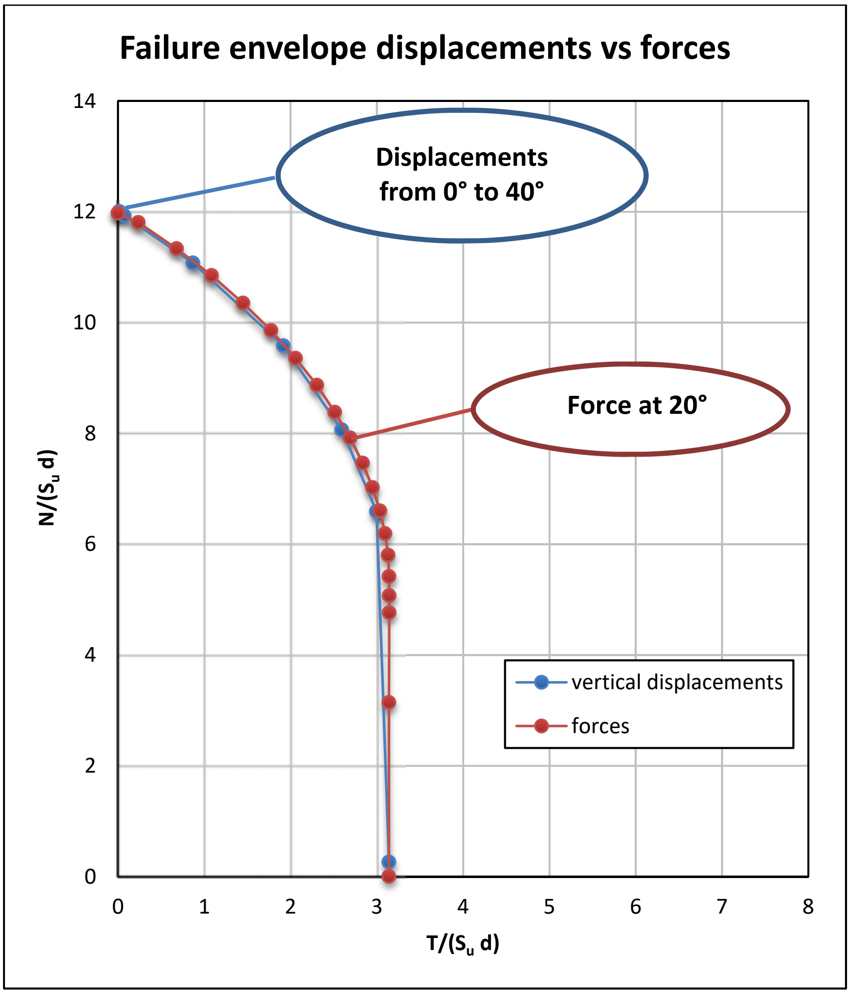

Figure 56. Comparison between forces and displacements envelopes

In conclusion, thanks to these numerical analyses it has been possible to determine the forces (vertical and horizontal) that act on a pile wall assumed non-deformable. It is important to underline that each force is referred to a flint long 1 meter because of the plane strain condition. For example, N_{lim}=240kN is the force needed to displace indefinitely a flint 1m long, with a 0.2m-diameter, within a chalk with a S_u of 100kPa.

5.6 Vertical displacements with pile

If a driven pile hits a flint during driving, it will certainly experience a deformation because of its non-infinite circular stiffness. Hence, it is not rigorous to model a pure vertical displacement as previously done. It could be necessary to introduce a horizontal spring with a stiffness comparable to that of the pile, in order to obtain consistent horizontal displacements. By consequence, the horizontal forces will be lower than that computed in the previous models.

Moreover, the presence of a wall could influence the flow of the soil around the flint. This phenomenon can be confirmed by some researches about the influence of the shaft on the resistance of the ball penetrometer (Randolph & Zhou, 2011). So, the presence of this element has to be investigated in order to understand its influence on the results. The output forces inside the wall are not so significant because the circular geometry of the pile can't be represented in plane strain. However, the contact forces computed are meaningful if a cylindrical geometry of the flint is assumed.

There is not a published solution for lateral loading on the end of a pipe, but Roark and Young (1975) give the deflection under a lateral load per unit length for a ring of diameter *D* and wall thickness *t*. Finite element analyses performed by Aldridge (2005) of the end section of a large diameter pile indicate that the lateral stiffness is similar to that derived for a ring of approximately *0.5D* length. Using this equivalent length and also taking a Poisson's ratio of 0.3 for the pile steel, the pile wall lateral deflection can be related to the force applied by the soil:

$$\rho_{lateral} = \frac{0.204\, F_{lateral}\, D^2}{t^3\, E_{pile}} \qquad 5.6$$

From this equation, the stiffness results equal to:

$$k_c = \frac{t^3\, E_{pile}}{0.204\ D^2} \qquad 5.7$$

For example, for a thickness of 70mm and a diameter of 4m the stiffness is:

$$k_c = 22068\ kN/m$$

A 3D model is done in order to confirm the circular stiffness of a pile loaded by a punctual force at the bottom. The model has the following characteristics:

- dimension: 50x50x50 m;
- properties of the soil: the same of the 2D model (see §5.3);

- properties of the pile: cylindrical plate of diameter of 4 m with a thickness of 70 mm and the properties of steel (E=210GPa, *v*=0.3);
- interfaces: positive interface around the pile with 0.5 R_{inter} factor, no soil inside the pile;
- mesh: fine mesh with a refinement around the pile;
- load: imposed horizontal increasing displacement up to 0.2 m at the bottom of the pile;
- stages: initial phase, pile installation, imposed displacement.

In *Figure 57* the described model geometry is illustrated:

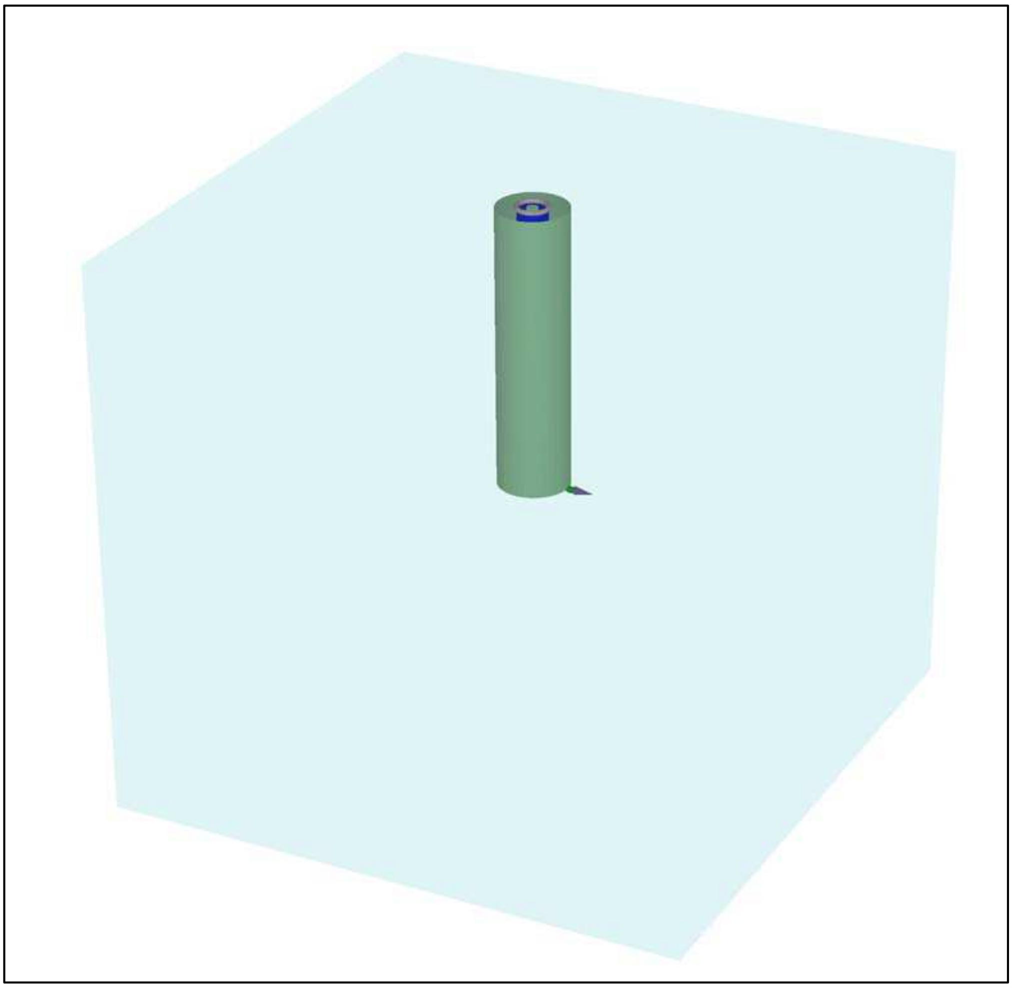

Figure 57. 3D pile model geometry

After the calculation it is possible to see the deformation of the pile caused by the applied displacement, as it is shown in *Figure 58* (deformed mesh).

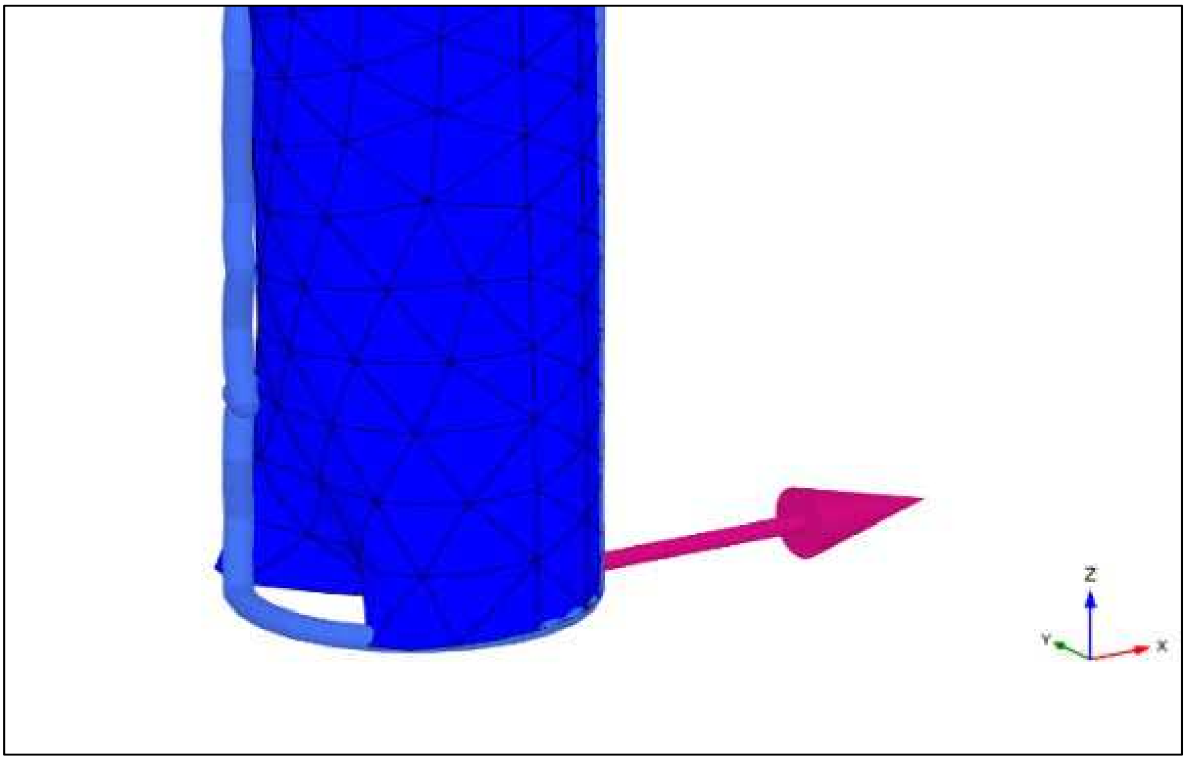

Figure 58. Deformed pile toe in 3D model

From this analysis, a load-displacement curve is generated. As it is possible to see in *Figure 59*, the behavior is slightly non-linear. So, in order to find a representative stiffness, it is necessary to select a reference displacement and linearize the curve. The chosen displacement is 0.1m because it is assumed that the pile will not deform more than 10cm in the contact with the flint. The corresponding approximated stiffness is:

$$k_c = 21500\ kN/m$$

This stiffness value is in agreement with the one calculated with the equation previously proposed (Aldridge, et al., 2005).

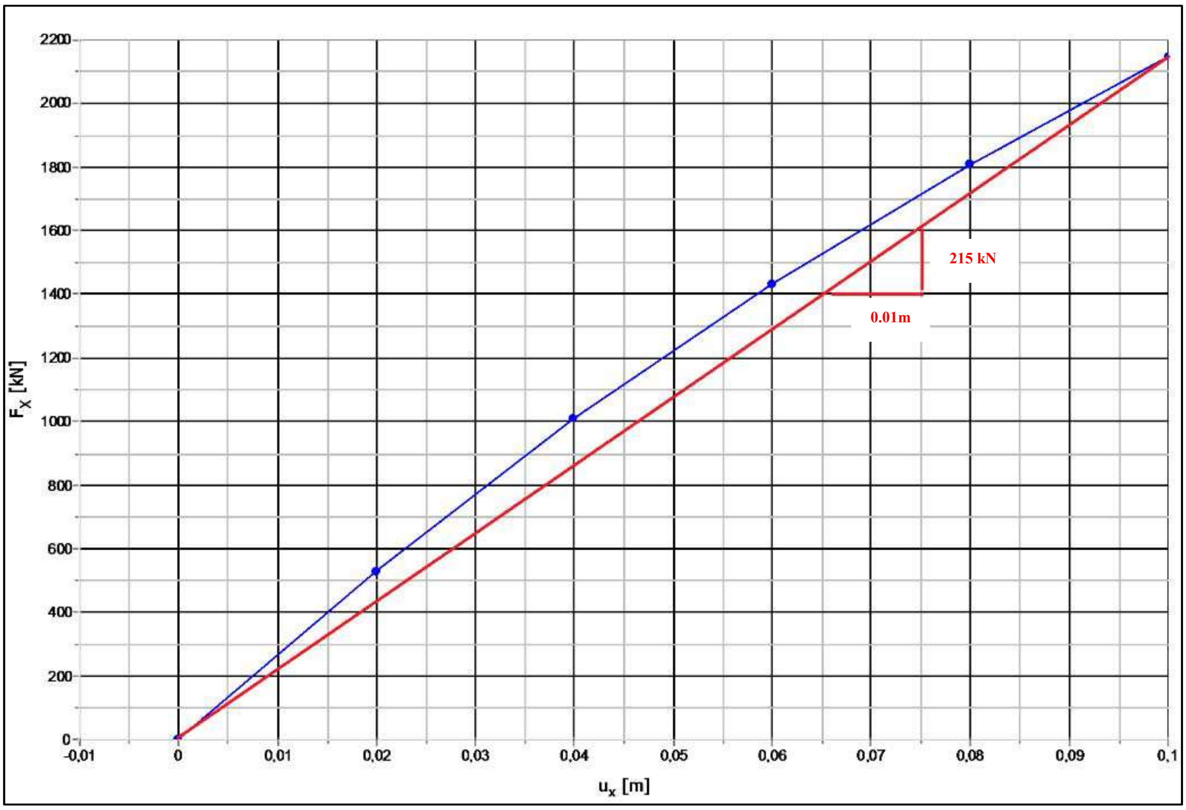

Figure 59. Pile circular stiffness linearization

If this stiffness is assigned on a horizontal fixed-end anchor in a plane strain model, the experienced horizontal displacement will be similar to the one of the 3D model, as well as the horizontal developed force. This has been verified with a simple 2D model (*Figure 60*) by applying a horizontal displacement at the bottom of a plate and by checking if the force obtained inside the spring was in according with that of the 3D model.

To a 0.05 m displacement corresponds a 1075 kN force inside the fixed-end anchor, which is perfectly in agreement with:

$$F = k_c \ u_x = 21500 \cdot 0.05 = 1075 \ kN$$

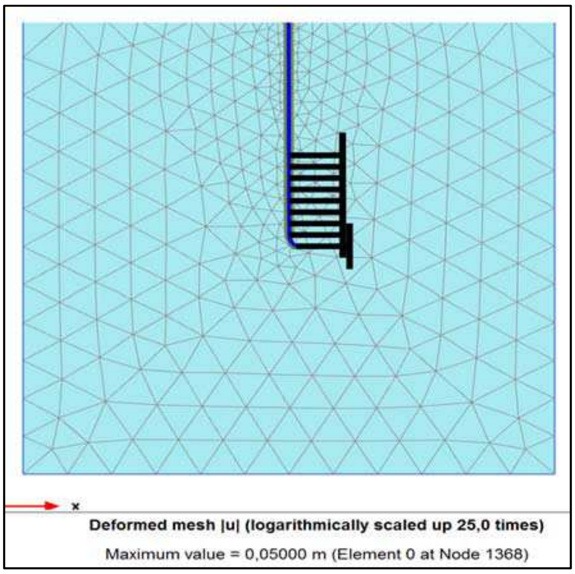

Figure 60. Pile model with fixed-end anchor

Thus, after this calibration it has been possible to perform the analyses on the 2D model, in order to find the forces that act on the pile depending on the contact position.

The model adopted is similar to the one already described in the previous chapter (see §5.3) but with the addition of a plate 4m long and 70 mm thick, which is in contact with the flint. In each calculation phase, the contact point is changed for the positions of 0°, 5°, 10°, 20°, 30°, 45°, 70°, 90°, as it is shown in *Figure 61*.

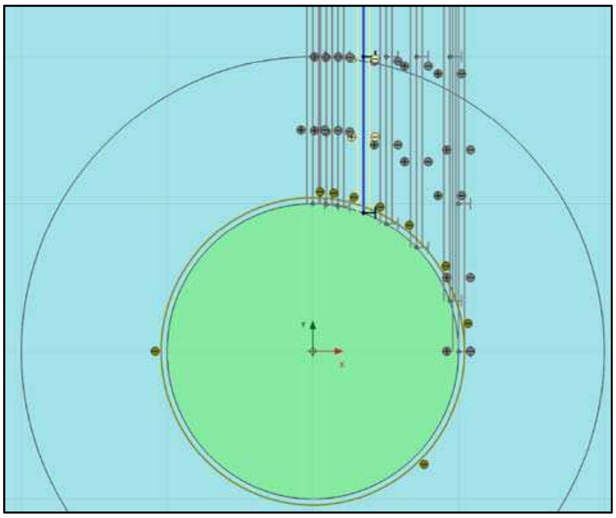

Figure 61. Pile-flint interaction with different contact points

A vertical displacement of 0.2m is imposed on the top of the plate in order to produce a complete failure in the soil. After the calculation, the vertical force is extracted by the load-displacements curve of the contact point, while the horizontal one is directly found as the reacting force inside the bottom spring.

The resulting forces are reported in *Figure 62*, as already done for the "Vertical displacement" model (see §5.5).

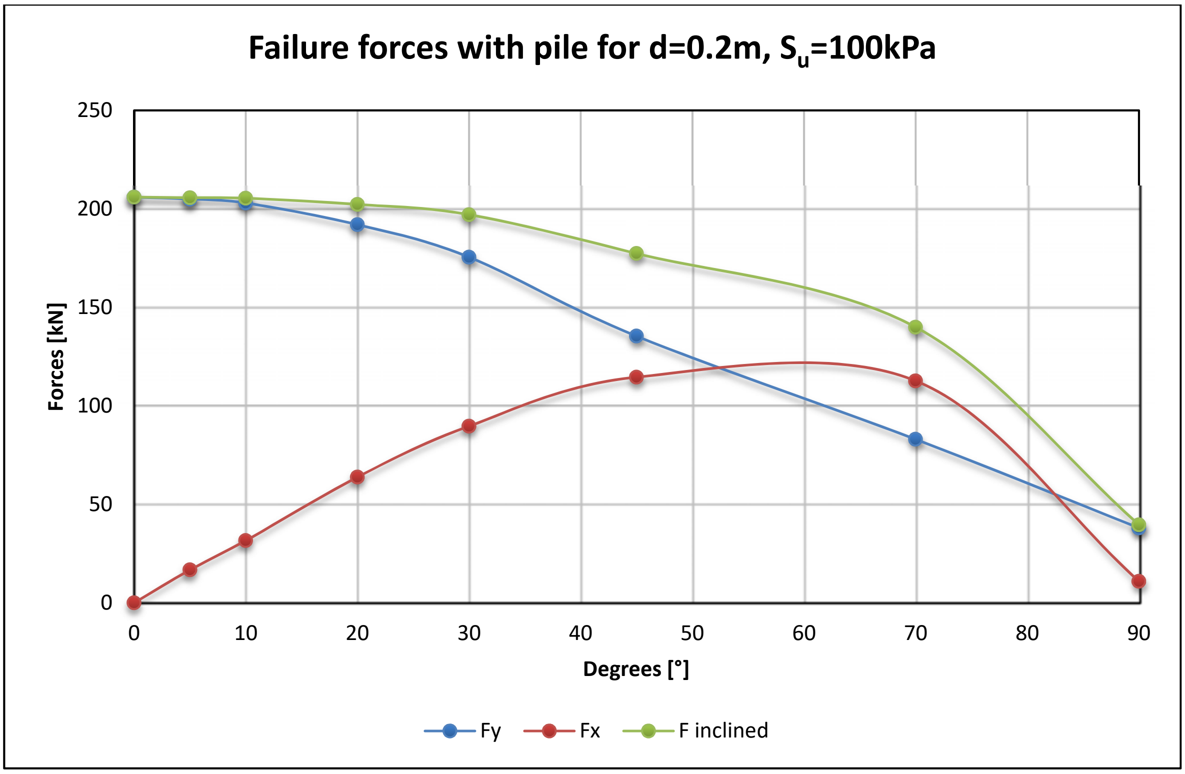

Figure 62. Resulting failure forces for different angles (Pile wall)

As expected, the vertical force decreases the more that the pile hits the flint laterally. On the contrary, the horizontal force increases. The trend is comparable to that of the previous model, where only vertical displacements were applied without the wall. In *Figure 63-64-65* are reported the comparisons of the two different models, the "Vertical displacements" model versus the "Vertical displacement with pile" model.

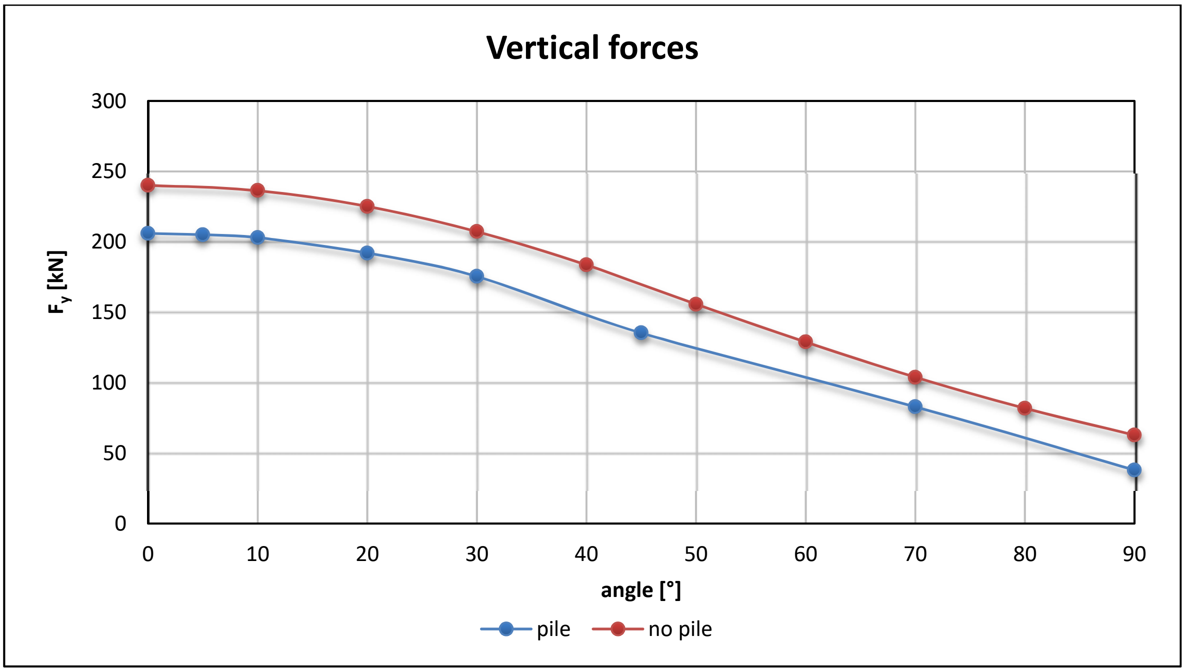

Figure 63. Comparison of resulting vertical forces

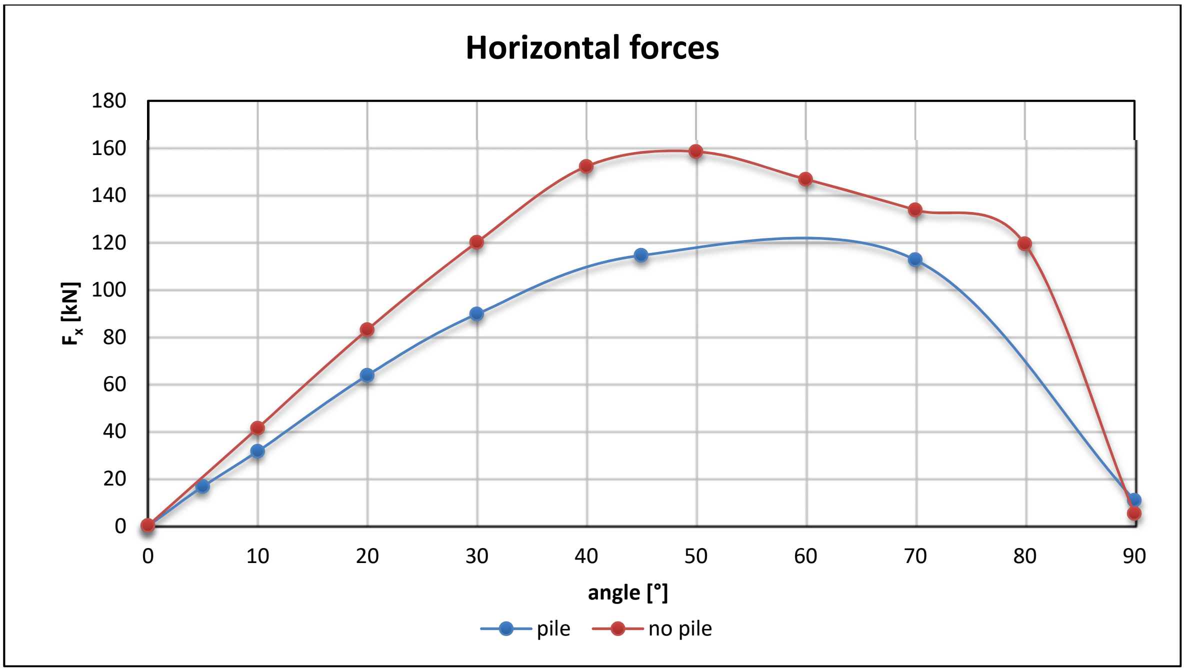

Figure 64. Comparison of resulting horizontal forces

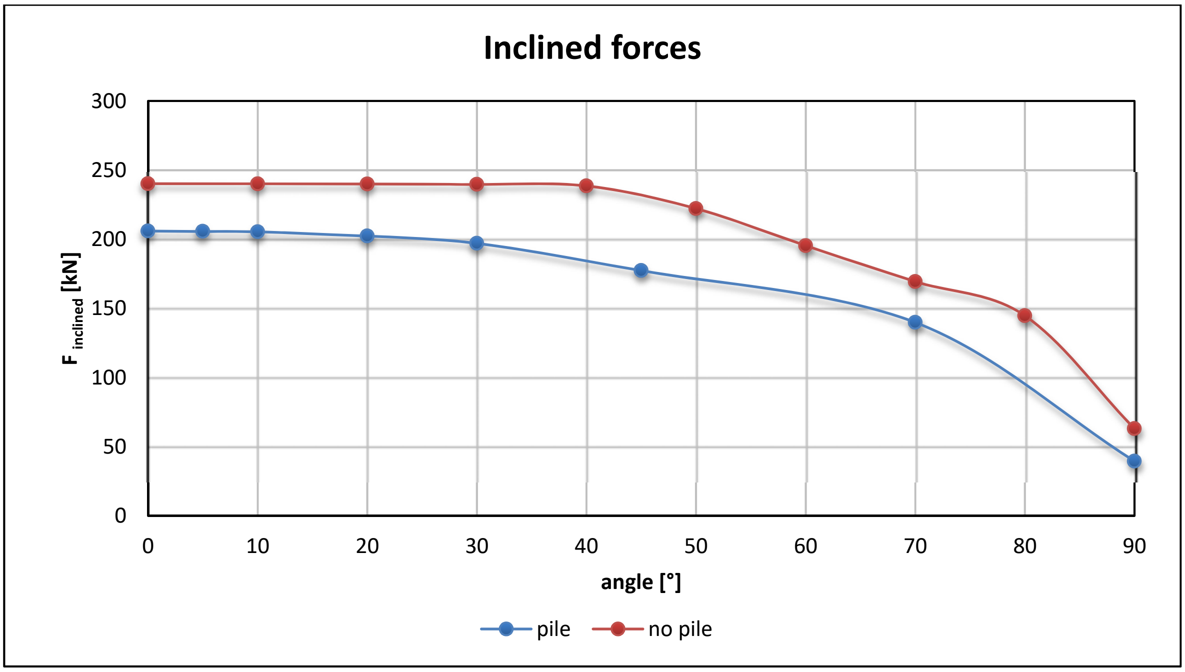

Figure 65. Comparison of resulting inclined forces

It is remarkable that the two trends are comparable. The forces resulting from the latter model (with pile) are lower basically for two main reasons, explained as follow.

The horizontal forces result lower because the introduction of the horizontal spring allows a small deformation of the pile. By consequence, the generated force at the contact decreases while a little horizontal displacement occurs.

The vertical forces result lower because the introduction of the shell in the model modifies the flow of the soil around the flint. By consequence the failure mechanism changes and the vertical force necessary to produce failure is reduced. In *Figure 66* the different flows are displayed, with and without the pile.

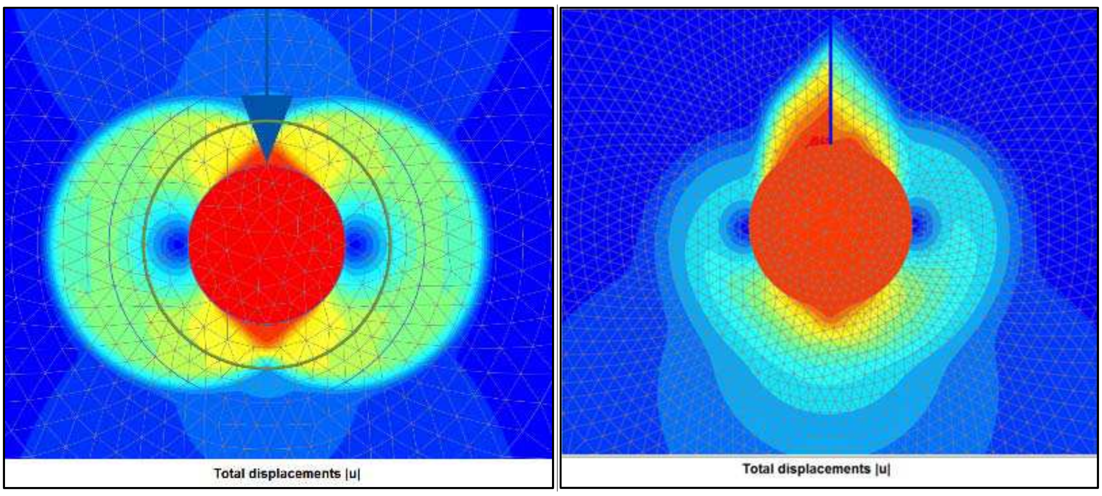

Figure 66. Flow with and without pile modelling

Finally, after these analyses, it can be concluded that the forces resulting from the two models have a difference of about 10-15%. Therefore, it could be not strictly necessary to model the pile wall but only to impose a pure vertical displacement. This simplification could be useful in a more complex analysis (e.g. 3D), in which the discretization of the contact between a cylinder and a flint could require a very fine mesh and by consequence a high time consuming.

5.7 Equivalent spring calibration

Since usually driveability analyses are based on 1D-stress wave theory where the soil is modelled as a spring, it is interesting to calibrate an equivalent spring which reproduces the mechanical impedance of the boulder embedded in a soil medium.

This stiffness depends on different factors such as the boulder size (diameter) and the deformation properties of the soil matrix (Young's modulus of soil). The S_u has no influence because the soil remains in an elastic condition.

A parametric analysis is performed in order to find different stiffnesses for different diameters and elastic modulus. The boulder diameters analyzed are 0.2, 0.4, 0.8. The stiffness modulus analyzed are 0.1, 0.5, 1 GPa. For each analysis a load displacements curve is found and the stiffness is obtained by calculating the slope of the first part of the curve, which is linear and follows this law:

$$F = k\ u_y \tag{5.8}$$

Figure 67 shows 3 load-displacements curves for different diameters and the same E. The more the diameter increases, the more the stiffness increases, as it is possible to notice from the slope of the first part of the curve.

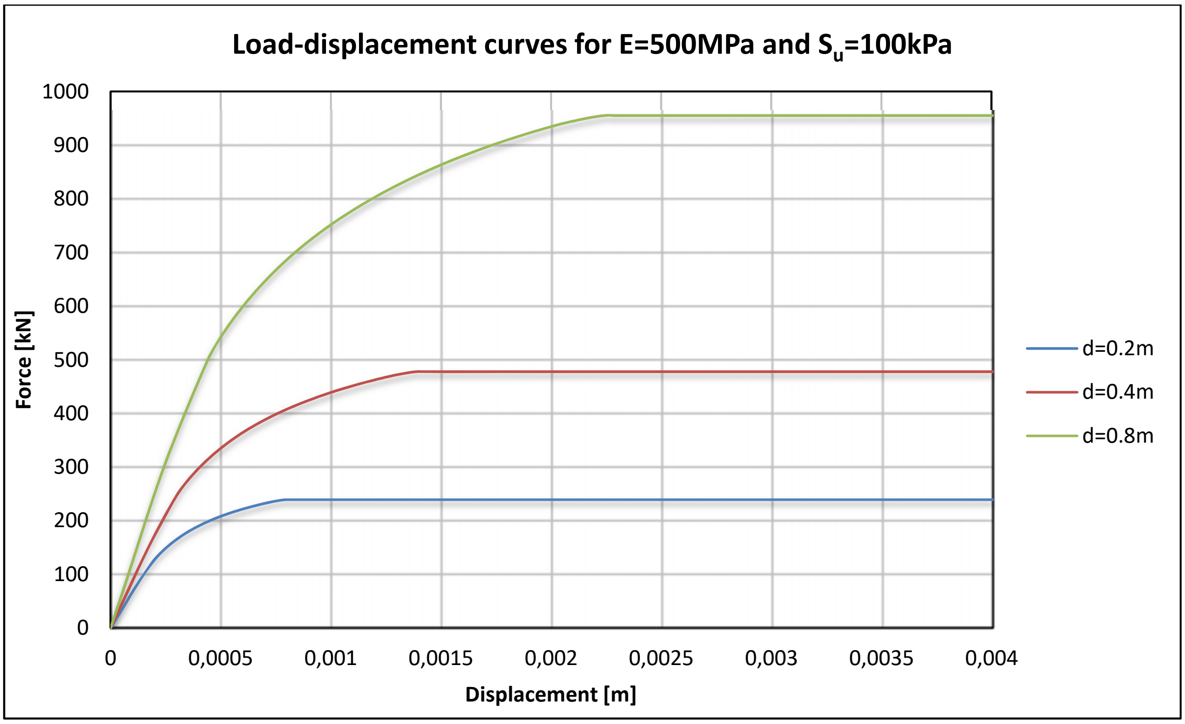

Figure 67. Load-displacements curves for different diameters(E=500MPa)

The results of the analyses are reported in Appendix A 10.1. From that database, a relationship between *k*, *E* and *d* can be found.

First of all, the relation between *E* and *k* is analyzed, by assuming a power law like:

$$k = a\ E^b$$

The exponent *b* is found by a trial and error procedure which aims to have a good fit between the data and the interpolating line. In statistic, a value is often required to determine how closely a certain function fits a particular set of experimental data. R^2 value computed in Excel is selected to determine how closely the data conform to a linear relationship. R^2 values range from

0 to 1, with 1 representing a perfect fit and 0 representing no statistical correlation between the data and a line. A value of $b = 1$ gives an $R^2 = 1$.

Secondly, the relation between d and k is found by assuming a power law like:

$$k = a \ d^b$$

A value of $b = 0.4$ gives an $R^2 = 0.99$.

Finally, by plotting $E \ d^{0.4}$ on the x-axis and k on the y-axis, an interpolating linear law is found (*Figure 68*).

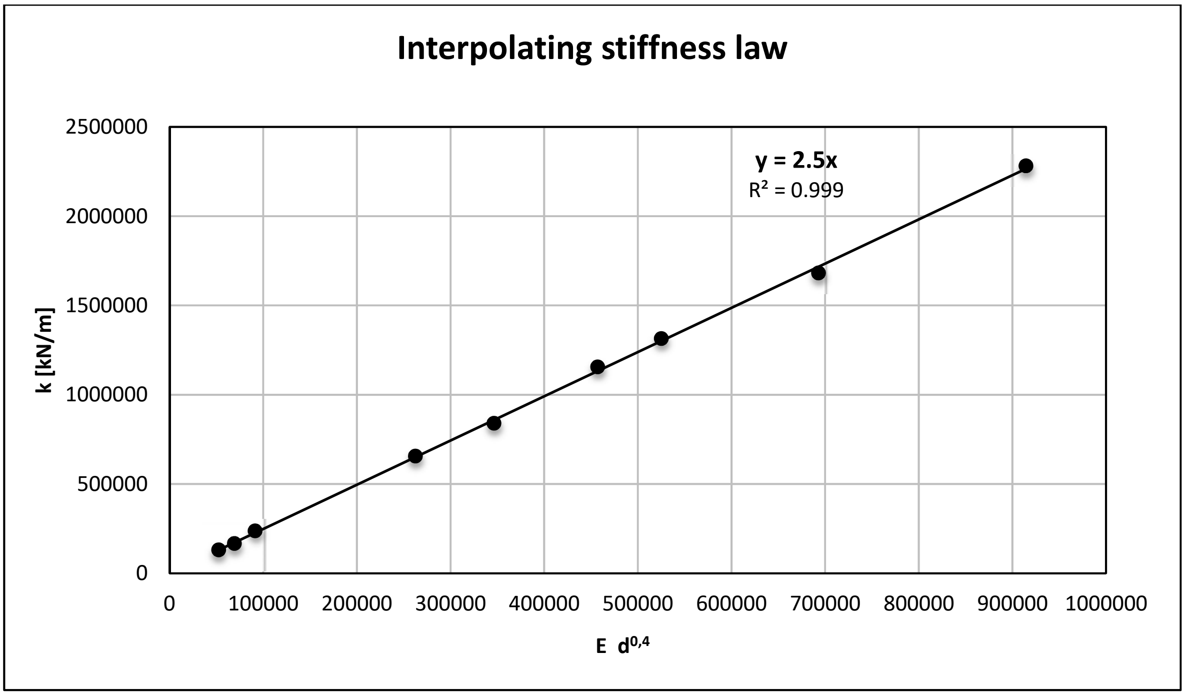

Figure 68. Linear trendline of stiffness vs E and d

By inserting a *E* value in kPa and a *d* value in meter, an approximate stiffness *k* in kN/m can be obtained using the following equation:

$$k = 2.5 \ (E \ d^{0.4}) \qquad 5.9$$

$$E \ in \ [kPa], d \ in \ [m], k \ in \ \left[\frac{kN}{m}\right]$$

6. Flint resistance to displacement: 3D static analyses

6.1 Introduction

Since the flint has not an infinite length, a plane strain condition could be not fully representative of the problem in exam. In fact, plane strain models can typically be used if one dimension is very large compared to the others. For this reason, a 3D analysis is done in order to identify if the trends of the failure envelopes/forces are comparable to that of the plane strain model. Since 3D analyses require a greater computational effort, the aim of these simulations is to understand if the 2D geometry can simulate in a reasonable way the problem in exam or if the 3D is strictly needed for the following analyses (i.e. dynamic) to correctly represent the studied phenomena. The flint will be modelled as a sphere and subjected to forces and vertical displacements, as in the 2D analyses. For the validation of the model some analytical solutions are adopted (like the one for the ball penetrometer). A preliminary axisymmetric analysis is done to have a numerical solution as a benchmark. The aim is to obtain the same load-displacements curve for a centered force, both in the axisymmetric that in the 3D model. Then, the 3D results will be compared to that of the 2D plane strain model previously exposed (see §5.3).

6.2 Benchmarks

6.2.1 Ball penetrometer

The piezoball penetrometer (*Figure 69*) is used to downhole testing of soft seabed, where the cone penetrometer may prove inadequate. It is also better suited respect to the T-bar penetrometer because of the smaller protrusion relative to the shaft. Diameters vary between 60 and 80 mm, with the shaft just behind the ball sized so that the ball area is approximately ten times that of the shaft. The filter for the pore pressure sensor can be placed either at mid-depth (as indicated), or at discrete points elsewhere on the lower half of the ball. Again, the ball resistance factor is based on plasticity solutions (Randolph & Gourvenec, 2011).

Figure 69. Piezoball penetrometer

The solution leads to a non-dimensional bearing capacity factor, N_b, that varies in the range from 11.80 to 15.54 (Tresca yield criterion) as the ball interface condition varies from fully smooth to fully rough. Corresponding lower bound solutions derived using the method of characteristics, and a Tresca yield criterion, range from 10.98 (smooth) to 15.10 (rough). Comparisons with results from finite element analyses show excellent agreement with the plasticity solutions (Randolph, et al., 2000).

In conclusion, the force can be calculated from this simple formula, in which N_b could be assumed in a range between 15.1 and 15.5 for a rough interface:

$$F = N_b \ \pi \ r^2 \ S_u \qquad 6.1$$

6.3 Axisymmetric model

6.3.1 Introduction

In the 2D model, a sphere is modelled in an axisymmetric conditions and subjected to a vertical centered force. In this way a numerical reference solution is provided. This model is validated with the ball penetrometer solution previously exposed. The only aim of this analysis is to validate the analytical solution of the ball penetrometer and to obtain a load-displacements curve to be compared with the one resulting from the 3D model. In fact, an axisymmetric model cannot be used to investigate lateral forces or displacements because of the symmetrical condition.

6.3.2 Model

Only half circumference is modelled in an axisymmetric condition. All the results obtained will be referred to a slice of a radian, so they will be multiplied by 2π in order to provide the force relevant a whole sphere (3D). The sphere has a diameter of 2m, the model size is 50x100m and the force is applied centrally. An isotropic state of stress is applied ($K_0 = 1$). A rigid interface element is added to allow sliding between flint and soil ($R_{inter} = 1$).

The soil is modelled as in the 2D plane strain model, with the only difference of the unit weight (because in the following 3D model it was not possible to apply easily a uniform field stress): γ_s is set at 19kN/m^3. In this way the state of stress is not uniform but it varies with the depth. The S_u is assumed equal to 200kPa.

A total stress analysis is carried out, in which stiffness and strength are defined in terms of undrained properties. Excess of pore pressure are not explicitly calculated, but are included in the effective stresses (Undrained C in PLAXIS).

Since the reduction factor is set to R_{inter}=1, the interface elements have the same properties of the surrounding soil. A pure vertical centered displacement of 1m is applied and the load-displacements curve is obtained. From *Figure 70*, it can be noted the developed flow around the ball (boulder/flint) at the failure step.

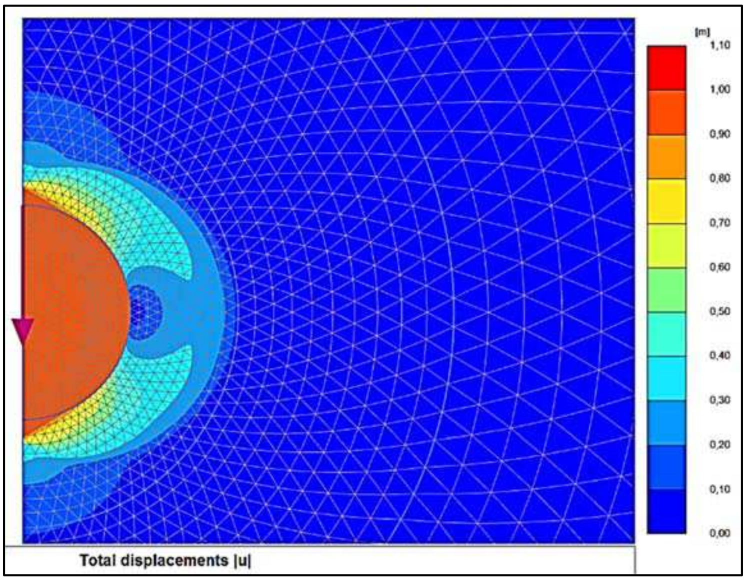

Figure 70. Model of sphere in axisymmetric conditions

The resulting force at failure is equal to *1513 kN* which should be multiplied for 2π in order to refer it to the whole sphere. So, the force becomes *9500 kN*.

The force obtained by the ball penetrometer analytical equation is (Randolph et al., 2000):

$$F = 15.1 \cdot 3.14 \cdot 200 \cdot 1^2 = 9480\ kN$$

Since the two forces are almost equal, the model is validated and the load-displacements curve can be used as a numerical benchmark for the 3D model.

6.4 3D model

6.4.1 Introduction

A sphere of 2m-diameter with an infinite stiffness and strength has been modelled, embedded in a soil in undrained conditions. Since PLAXIS did not work well with a perfectly spherical geometry, the sphere has been approximated by a polygon of 12 sides rotated around his axis. The geometry has been imported from AutoCAD as a *.dwg* file. With this modelling solution, the simulation works. The size of the model is 100x100x100m. Interface elements are added in order to allow sliding between flint and soil.

In the numerical analyses, a vertical force is applied at different positions to obtain a failure envelope ("Inclined forces 3D" model, see §6.4.3). The model is validated by comparing the load-displacements curve derived for a centered force to that obtained from the axisymmetric model.

Secondly, a pure vertical displacement (horizontally restrained) is applied in different positions in order to simulate the circular pile stiffness and to find a horizontal and vertical failure force ("Vertical displacements 3D" model, see §6.4.4).

6.4.2 Geometry and mesh

At the initial model study stage, the boulder was modelled with the command “sphere” of PLAXIS, which creates a spherical volume automatically. From that volume, a surface was created in order to insert an interface. However, even if the geometry was correct and the mesh very fine, the results were not so accurate. In fact, the load-displacements curve did not reach a plateau but it continued to increase indefinitely.

The solution of this problem was to change the geometry. Probably, a spherical geometry embedded in a soil caused some numerical issues to the software and so, an approximated geometry was introduced. A polygon with 12 sides inscripted in a circle of 2m-diameter was adopted to generate the sphere. Then, by rotating it around its axis, the volume was created. This geometry was imported in PLAXIS with the command “Import soil volume”. From this volume a surface was created in order to insert an interface around the boulder.

Then, the results have been compared to that of the axisymmetric analysis and to the analytical solution. As it can be seen from *Figure 71*, the 3D results are in agreement with those obtained with the 2D axisymmetric model, and thus with the analytical result.

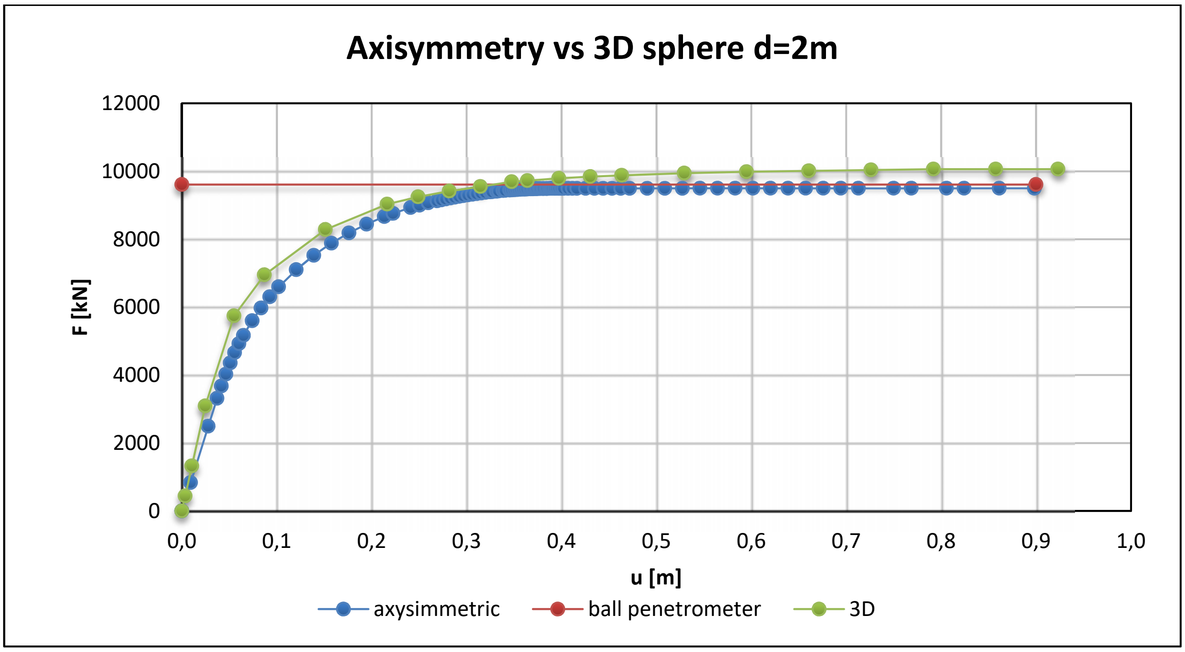

Figure 71. Comparison between axisymmetric and 3D load-displacements curves

After this calibration of the model, more complex analyses with no reference solutions can be done.

Concerning the mesh, the basic soil elements of the 3D finite element mesh are the 10-node tetrahedral elements. In PLAXIS the user may select an element distribution to make the mesh globally finer or coarser. In order to increase the mesh locally, 5 volumes with the same shape of the boulder but with different sizes are added, as it is shown in *Figure 72*.

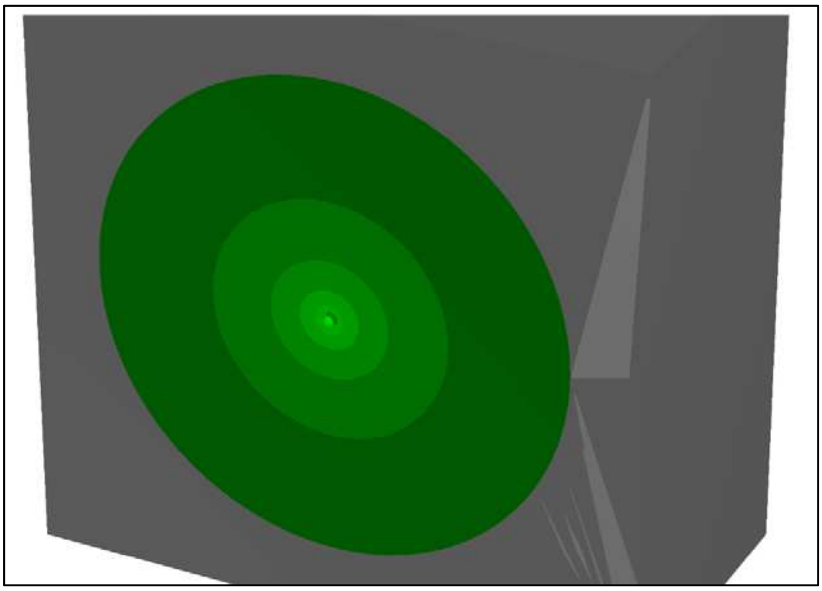

Figure 72. Mesh refinement with sphere volumes

This allows to increase the mesh quality only in the zones where high gradients of deformation are expected, reducing the computational time by avoiding an unnecessary discretization far from the flint. So, the density of the mesh is decreased with the distance from the boulder.

From a sensitivity analysis, the size of the mesh is chosen in order to reach a good compromise between time-consuming and quality of the results. In *Table 9* the mesh details are summarized:

Table 9. Mesh information 3D model

Model	3D
Element	10-noded
Average element size	2.791 m
Maximum element size	12.43 m
Minimum element size	0.07 m

6.4.3 Inclined forces 3D

To provide a failure envelope as already done in the 2D plane strain model, a vertical force is applied on the flint by changing the position of the point load (or indifferently a centered force is applied by changing the inclination). In the point load, no horizontal restrains are applied. From the load-displacements curve is possible to get the value of the force reached on the plateau, which corresponds to the failure force. This is done for all the different positions and consequently 10 forces are found. By simply projecting these forces, the normal and the tangential components are obtained and a failure envelope is plotted (*Figure 73*).

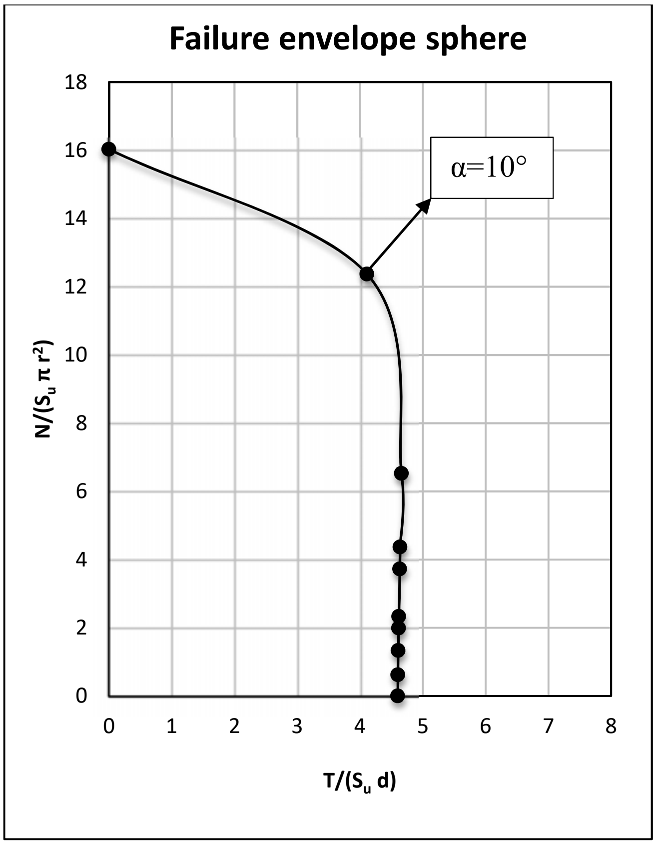

Figure 73. Sphere failure envelope

The envelope has a shape similar to the one related to the plane strain geometry. From this chart it is possible to conclude that for a force with an inclination bigger than 10° the failure happens in a rotational way (vertical line on the envelope). On the contrary, for lower angles, a bearing capacity failure occurs (already explained for plane strain model, see §5.4).

6.4.4 Vertical displacements 3D

Since the pile, when it hits the boulder, applies a restraint to the horizontal displacement due to its circular stiffness, it is more interesting to analyze what happens to the flint under prescribed pure vertical displacements. By consequence, a horizontal force will arise due to the presence of the restraint. To find its value, it is necessary to add a fixed-end anchor with an infinite stiffness (*EA=100E33*) as a horizontal restrain and then to apply a vertical displacement. This is repeated for 10 different points on the sphere, as shown in *Figure 74*.

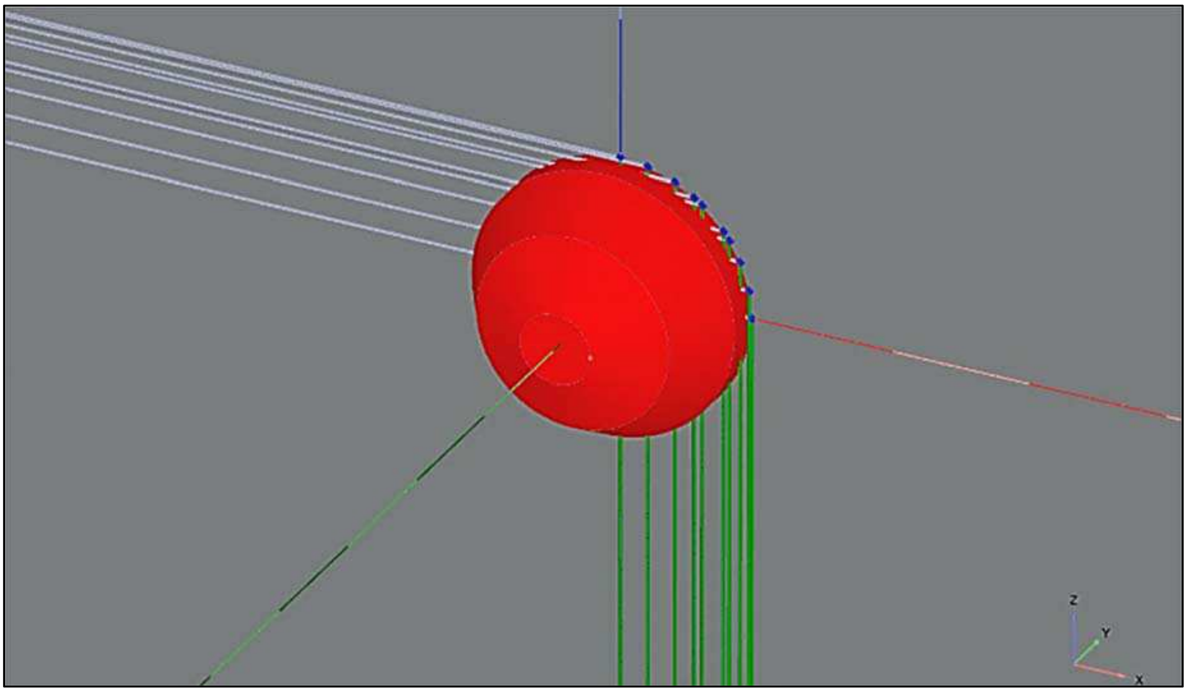

Figure 74. 3D model with displacements applied in different positions

For each point a horizontal and vertical failure force is obtained, and so a plot can be created to understand the trend. The vertical (F_z), the horizontal (F_x) and the inclined force (F_i) which is the vectorial sum of the previous two, are plotted in *Figure 75*.

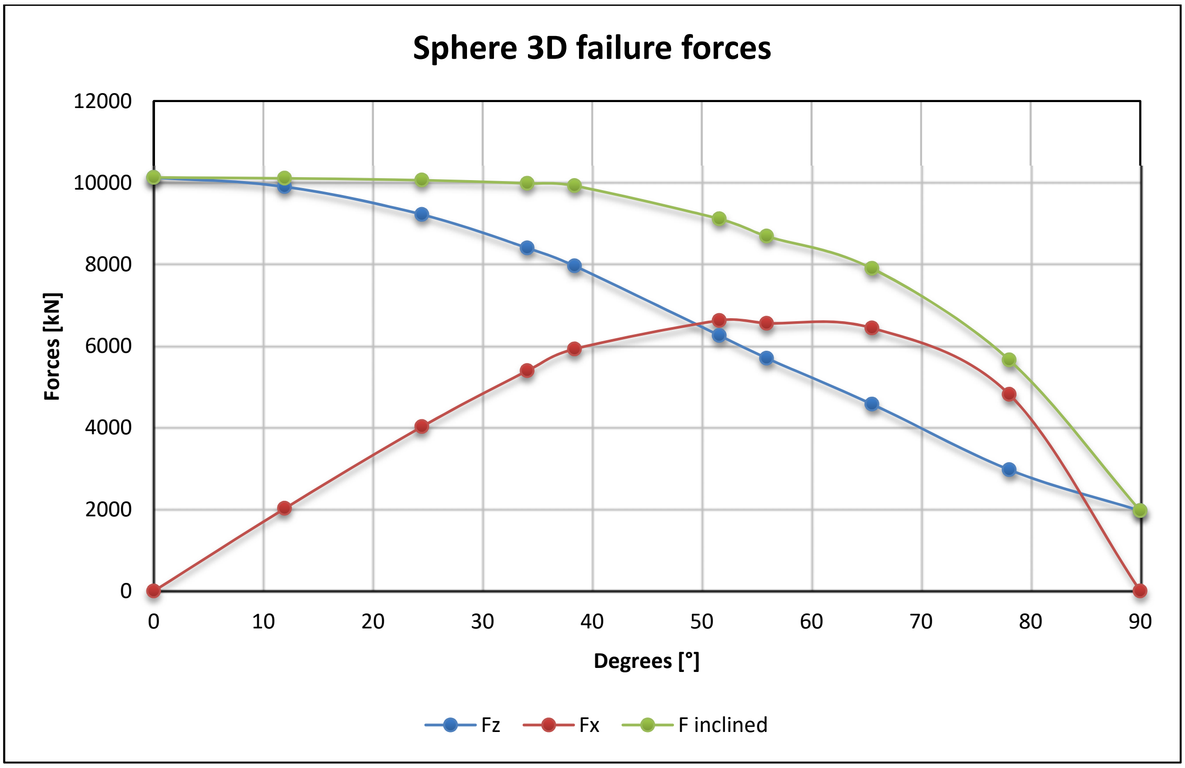

Figure 75. Sphere failure forces

Obviously, the vertical force is maximum in case the pile hits the boulder centrally, while the horizontal one reaches its maximum at about 50°.

Differently from the previous case (no horizontal restraints, see §6.4.3), a bearing capacity failure mechanism occurs until about 40°.

Figure 76-77 show the total displacements in a vertical sections and in a 3D view, for 0° and 50°, which are the most interesting points. In the left figures, it can be clearly seen a bearing capacity failure mode with a flow around the sphere. On the contrary, in the right ones it is showed a rotational failure mode, since the displacement is imposed laterally.

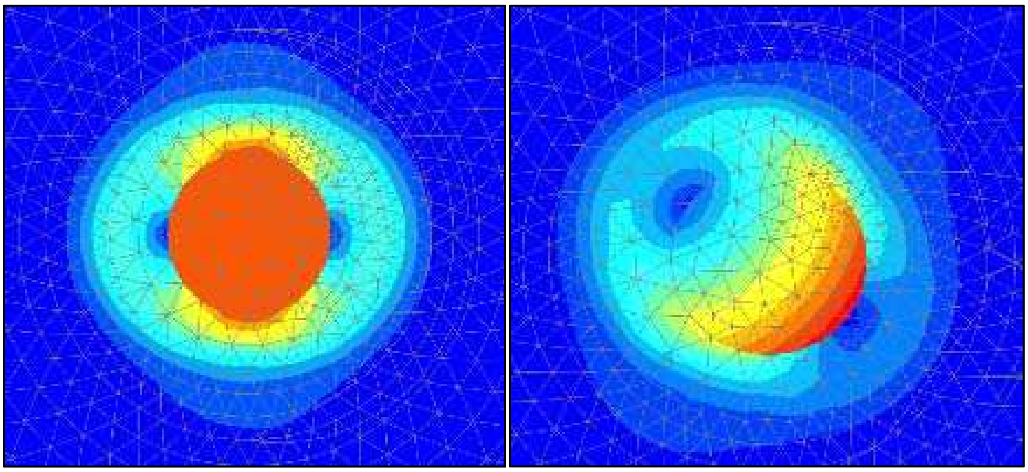

Figure 76. Total displacements in vertical section (passing through the center and the point displacement) for 0° and 50°

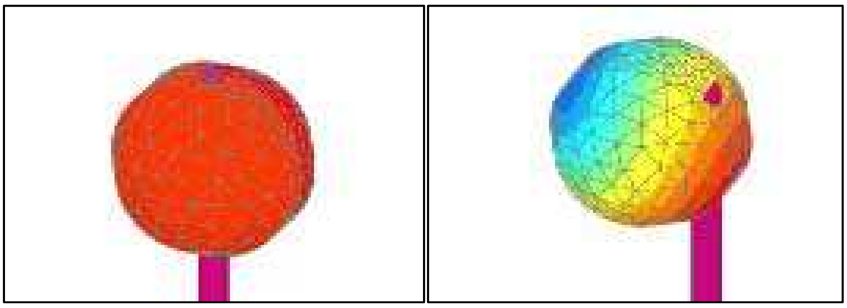

Figure 77. Flint total displacements for different contact point

6.5 Comparison of results

It is interesting to compare the 3D graph (*Figure 75*) with the one found for the 2D plane strain model for a 2m-diameter boulder. To do this, the 3D forces are scaled (divided for themselves and multiplied for 2400kN which is N_{lim} in plane strain condition) in order to match with the ones of the 2D model and the graphs are superimposed (*Figure 78*). In blue are plotted the scaled forces related to the 3D analysis and in red the ones related to the 2D plane strain analysis. It is possible to affirm that the trend is analogous. In both the cases, the maximum horizontal force is reached if the pile hits the boulder at about 50°.

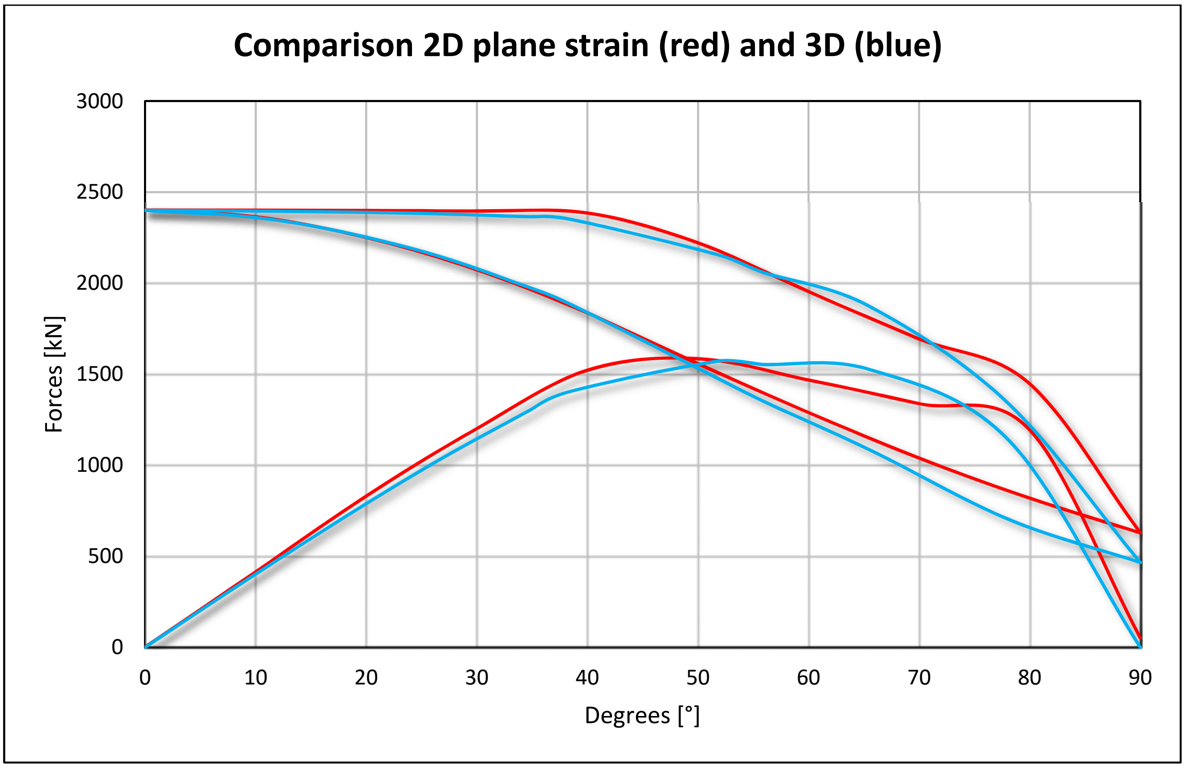

Figure 78. Comparison between 2D and 3D resulting forces

Thus, the main conclusion is that a spherical flint could be modelled in plane strain as a cylinder with the same diameter (the forces obtained will be related to a cylinder of 1m length). In fact, by multiplying these forces for the diameter it is possible to pass from a cylindrical to a spherical geometry. This notion can be demonstrated analytically for a centered vertical force, by equalizing the ball penetrometer solution with the T-bar penetrometer solution; then, it is extended to lateral forces since it has been shown that the trend of the arising forces for different angles is comparable.

$$15.1\ \pi\ r^2\ S_u = 11.9\ S_u\ 2\ r\ L$$

$$\rightarrow\ L = 1.98r \sim 2r = d$$

In conclusion, the analyses in the following of this study will be done only on the 2D plane strain model, since the computational time is lower and the results are in agreement with the 3D, which still represents in a better way the real geometry.

7. Flint resistance to displacement: 2D dynamic analyses

7.1 Introduction

The Finite Element Method (also noted FEM) can be considered a complete and reliable tool to investigate the propagation of ground vibrations due to pile driving. Indeed, an adequate soil constitutive model and a correct definition of the input are required. As well, in modelling the dynamic response of a soil, the inertia and the time dependency of the load are considered. Also, damping due to material and geometry has to be taken into account. With the PLAXIS Dynamic analysis module it is possible to analyze the effects of the vibrations in the soil. The most relevant aspects related to this type of projects are:

- the definition of an appropriate geometry and the corresponding required lateral boundary conditions;
- the selection of the most representative constitutive models for the soil involved and the calibration of the model parameters;
- the application of the input motion;
- the appropriate selection of the calculation parameters for the time-step integration;
- the dimension of the element in the finite element mesh.

The basic relation for the time-dependent movement of a volume under the influence of a dynamic load is given by equation 7.1:

$$[M]\ddot{u}(t) + [C]\dot{u}(t) + [K]u(t) = F(t) \qquad 7.1$$

where *M* is the mass matrix, *C* is the damping matrix and *K* is the stiffness matrix. Vectors $u, \dot{u}, \ddot{u}$ represent the displacement, the velocity and the acceleration at a given instant respectively. The vector *F(t)* corresponds to the system excitation at that time *t*.

In a static analysis acceleration and velocity are equal to zero. Hence, in comparison with a static model, in a dynamic problem the mass of the structure assumes a singular relevance. In particular, in geotechnical models special attention should be given to the definition of the phreatic level and to the selection of the soil unit weights.

7.1 Soil dynamics

7.1.1 Wave propagation

When a hammer strikes a pile during driving, the energy is transmitted from the hammer to the pile and travels down along the pile in the form of compressive waves, called the primary body waves or P-waves. A large portion of this energy is used for advancing the pile and is transmitted to the soil in two ways (see *Figure 79*): firstly, due to the friction along the soil-pile interface in form of shear waves (S-waves) propagating in a complex wave front and secondly, due to compression by penetration at the pile toe in the form of P-waves propagating on a spherical wave front (Serdaroglu, 2010). Thus, the velocity-dependent soil stress acting along the pile shaft and at the pile toe causes ground vibrations during impact pile driving (Massarsch & Fellenius, 2008).

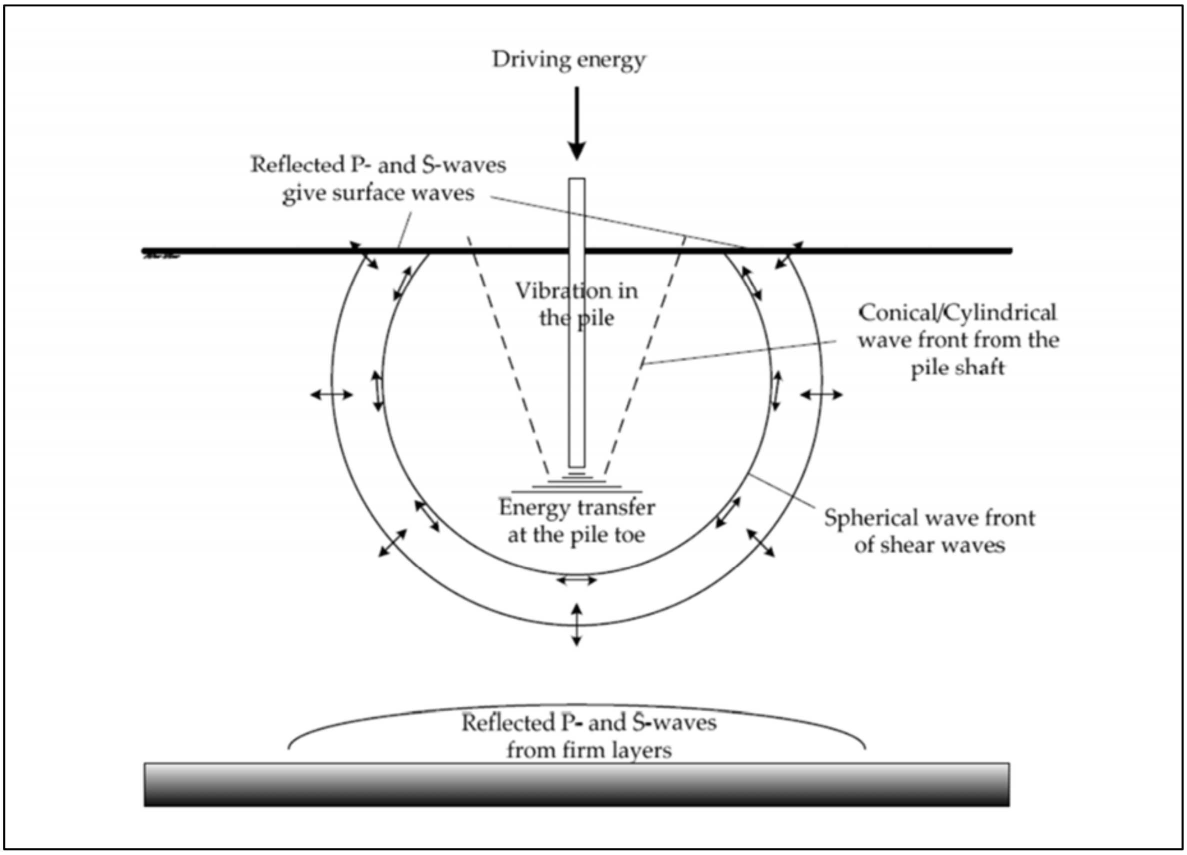

Figure 79. Schematic representation of different wave types in pile driving (Attewell & Farmer, 1973)

This resulting ground motion depends on many factors including source parameters (method of pile driving, energy, and pile depth), the interaction between the pile and the soil, and the propagation of the waves through the geological structure at the site (Masoumi & Degrande, 2008).

In presence of an obstruction, when the pile hits the boulder mainly P-wave are transmitted to the soil due to the boulder displacements. In fact, the mechanism is similar to an enhanced pile end bearing capacity. In this case vibrations are emitted and propagate as body waves, mainly in the form of compression waves, towards the ground surface where they are transformed to surface waves.

P-waves, also known as primary, longitudinal or compressional waves are associated to changes in volume from successive compression and dilatation. These waves can be referred to as longitudinal waves, because the particle displacements are parallel to the direction of propagation (Kramer, 1996).

Compression waves travel through both solid and liquid materials. For saturated soils, water modifies the characteristics of the wave propagation. The compression waves velocity in saturated soils is influenced by the velocity of compression waves in water, which is typically assumed about 1500m/s. Nevertheless, the ground water conditions influence the propagation of compression waves only, since the water does not have shear stiffness. For P-waves, the propagation velocity through loose soils depends on the degree of saturation; S-waves and R-waves are not influenced by the ground water.

The velocity of propagation of waves is influenced also by the characteristics of the skeleton (or matrix) of the material the waves travel through. The P-waves and S-waves velocities depend on the density and on the stiffness of the material. The soil, in particular when fully saturated, has higher stiffness in compression than in shear so that P-waves have a higher velocity than S-waves.

7.1.2 Soil damping

The pile driving process generates dynamic soil stresses along the pile shaft and at the pile toe during the propagation of the stress wave. Thus, the prediction of the oscillation of a boulder within the soil requires the modelling of the dynamic response of the soil around.

The amplitude of a stress wave decreases as the wave travels through the soil. There are two primary mechanisms that cause this attenuation of wave amplitude:

- material damping, which is due to absorption of energy by the materials the wave is traveling through;
- geometric attenuation, due to the spreading of wave energy as it travels away from its source.

Viscous damping, by virtue of its mathematical convenience, is often conventionally used to represent the dissipation of elastic energy.

In simplified approaches, the soil response can generally be represented by a combination of a spring and a dashpot. However, it is also necessary to consider limiting values of soil resistance, which is accounted for by means of a slider.

Smith (1960) presented the one-dimensional wave equation based on solution algorithm for dynamic pile driving. In that model, the soil resistance to driving is provided by a series of spring and dashpots (*Figure 80*). The soil springs are assumed to behave in an elastic perfectly plastic manner, and the spring stiffness is defined by a ratio of the maximum elastic deformation or quake Q. Damping coefficients were introduced to account for the viscous behavior of the soil. The total soil resistance to pile driving is given by:

$$R_t = R_S \ (1 + J \ v) \qquad 7.2$$

where R_t is the total soil resistance to driving, J is the damping coefficient, v is the velocity of the toe of the pile, R_S is the static soil resistance. The viscous enhancement of the soil resistance was taken as a linear function of the velocity (Smith, 1960).

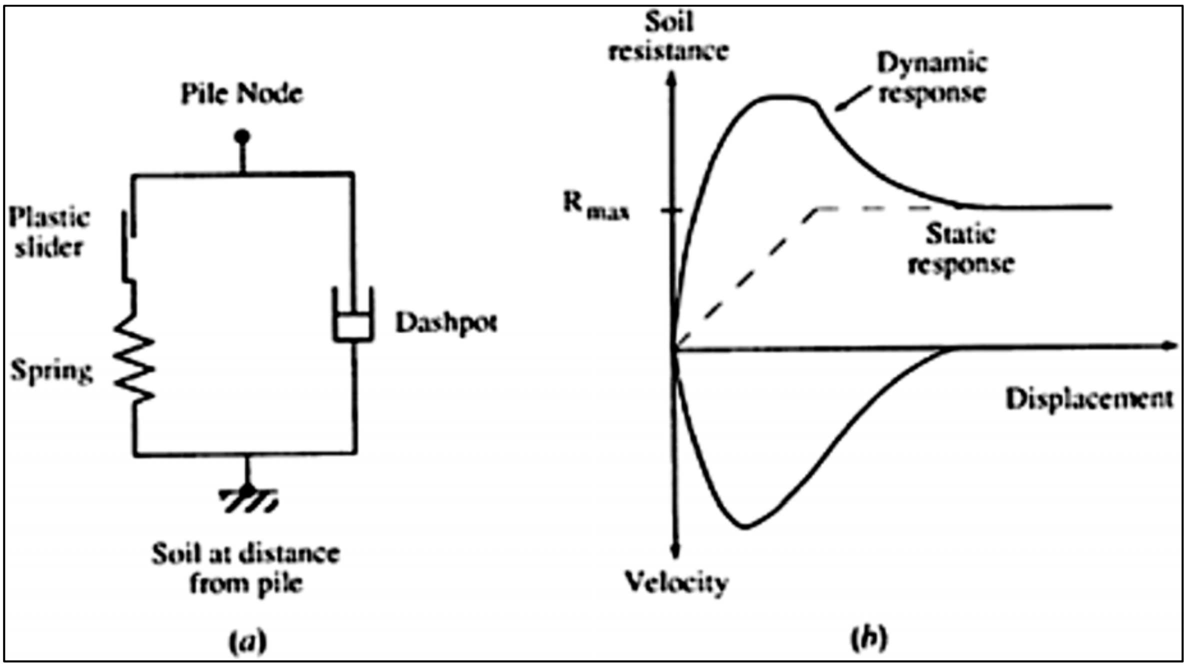

Figure 80. Scheme of dynamic soil resistance

In Smith's original work, the dashpot was introduced to allow for viscous (or material) damping, and no consideration was given to radiation. Having regard to the importance of radiation damping, most commercially available programs for pile driving analysis still consider all damping effects into the parameters *J*.

In real soil, since the soil particles move due to the propagating of the wave, part of the elastic energy of a travelling wave is always converted to heat by the slippage of grains with respect to each other's. This leads to a loss of energy due to internal hysteretical dissipation inside the material and by consequence a decrease in the amplitude of the wave it is produced. As a result of this process, the energy dissipation characteristics are insensitive to frequency.

Since material damping absorbs some of the elastic energy of a stress wave, the specific energy decreases as the wave travels through a material. The reduction of specific energy causes the amplitude of the stress wave to decrease with distance.

Moreover, there is also a reduction in amplitude due to spreading of the energy over a greater volume of material. In this geometric attenuation the elastic energy is conserved and so it should be distinguished from material damping in which elastic energy is actually dissipated by viscous, hysteretic, or other mechanisms.

For problems in which energy is released from a finite source, radiation damping can be extremely important (Kramer, 1996). If the rupture zone can be represented as a point source, the wave fronts will be spherical and by consequence the geometric attenuation causes the amplitude to decrease at a rate of $1/r$.

In conclusion, when a flint oscillates within the soil, it transmits energy to the adjacent soil. Part of this energy is stored in the soil in the form of elastic energy and the remaining part is lost being transformed into heat (material damping) or radiated to infinity in the form of stress waves (geometric attenuation).

Damping is required in all dynamic analyses because it represents the resistance to deformations when velocities are present. In numerical calculations three types of damping exist: numerical damping, due to finite element formulation, material damping, due to viscous properties, friction and development of plasticity, geometric attenuation due to energy spreading.

Referring to material damping, in PLAXIS most soil models do not include viscosity as such. Instead, a damping term is assumed, which is proportional to the mass and the stiffness of the system. Thus, the material damping is simulated with the well-known Rayleigh formulation (Liu & Gorman, 1995).

According to Rayleigh damping formulation, the damping matrix *C* is given by a portion of the mass matrix *M* and a portion of the stiffness matrix *K*, as a function of the Rayleigh coefficients α_R and β_R:

$$[C] = \alpha_R[M] + \beta_R[K] \tag{7.3}$$

Despite the absence of Rayleigh damping, the vibration of the boulder is anyway damped due to soil plasticity and the fact that wave energy is absorbed at the model boundaries (PLAXIS, 2014).

As already mentioned, in the cases in which energy is released from a finite source the effect of geometric attenuation often dominates those of material damping. In order to simulate this type of damping in a numerical model, special boundary conditions should be added to avoid that the stress or displacement boundary condition cause the reflection of the wave back, which is non realistic.

Lysmer and Kuhlemeyer (1969) investigated the use of special boundaries to suit the finite dimension of the model and avoid wave reflection, which is necessary to reproduce the behaviour of an infinite system. In their work, they analyzed the different possibilities for expressing this boundary condition analytically and found that normal and shear stresses, respectively, must be expressed by:

$$\sigma = -C_1 \, \rho \, V_P \, \dot{u_h} \tag{7.4}$$

$$\tau = -C_2 \, \rho \, V_S \, \dot{u_v} \tag{7.5}$$

These expressions depend on the normal and tangential velocities and on the domain border; parameters ρ, V_P, and V_S denote the local values of the density and the longitudinal and shear wave velocities, respectively. Equations 7.4 and 7.5 define a physical border supported on distributed stress dashpots oriented normally and tangentially with respect to the boundary (*Figure 81*).

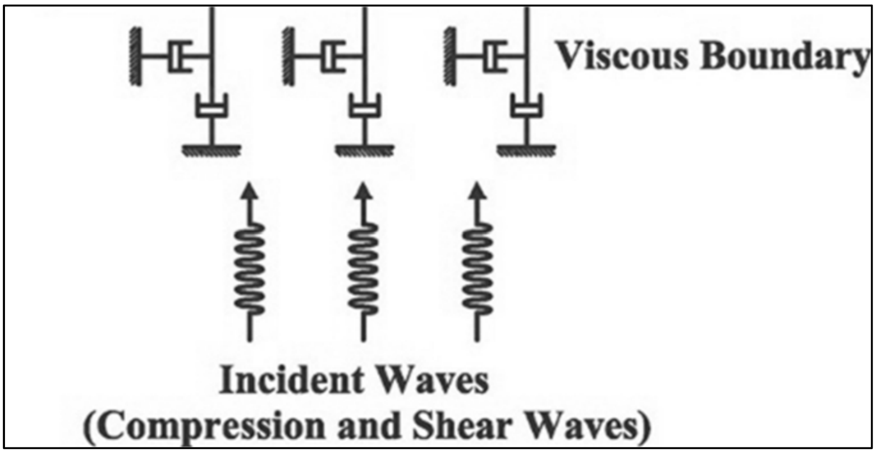

Figure 81. Viscous boundaries

The authors proposed a study on the reflection and refraction of the body waves at the viscous border to show that the latter is able to absorb impact elastic waves, which for the model is perfectly equivalent to a wave continuing its propagation outside. The analysis is based on the effective energy ratio, defined as the ratio of the reflected to the impacting energy by unit of surface. By varying the dimensionless parameters C_1 and C_2, the authors show that C_1=1 and C_2=0.25 lead to nearly perfect absorption, defining the case of efficiency boundary conditions (nonreflecting conditions).

The use of absorbing boundaries in PLAXIS is based on the method previously described. So, selecting absorbent boundaries, a damper is used instead of applying fixities in a certain direction. The damper ensures that an increase in stress on the boundary is reasonably absorbed without rebounding. The boundaries then start to move. C_1 and C_2 are relaxation coefficients that have been introduced in order to improve the effect of the absorption. In fact, in the presence of shear waves, the damping effect of the absorbent boundaries is not sufficient without relaxation. The effect can be improved by adapting the second coefficient in particular.

In the numerical implementation of dynamic problems, the formulation of the time integration constitutes an important factor for stability and accuracy of the calculation process. Explicit and implicit integration are two commonly used time integration schemes. In PLAXIS, the Newmark type implicit time integration scheme (Newmark, 1959) is implemented. The implicit method is more complicated, but it produces a more reliable and stable calculation process and usually a more accurate solution. With this method, the displacement and the velocity at the point in time $t + \Delta t$ are expressed respectively as:

$$u_{t+\Delta t} = u_t + \dot{u}_t\,\Delta t + \left[\left(\frac{1}{2} - \alpha_N\right)\ddot{u}_t + \alpha_N\,\ddot{u}_{t+\Delta t}\right]\Delta t^2 \tag{7.6}$$

$$\dot{u}_{t+\Delta t} = \dot{u}_t + [(1-\beta_N)\ddot{u}_t + \beta_N \ddot{u}_{t+\Delta t}]\Delta t \tag{7.7}$$

The coefficients α_N e β_N, which should not be confused with Rayleigh coefficients, determine the accuracy of the numerical time integration. For determining these parameters, different suggestions are proposed.

In order to keep a second order accurate scheme and to introduce numerical dissipation, a modification of the initial Newmark scheme was proposed by Hilber et al. (1977) introducing a new parameter γ (α in the notation of the author), which is a numerical dissipation parameter. The original Newmark scheme becomes the α-method or Newmark HHT modification. The α-method leads to an unconditionally stable integration time scheme and the new Newmark parameters are expressed as a function of the parameter γ, according to:

$$\alpha_N = \frac{(1+\gamma)^2}{4} \qquad \beta_N = \frac{1}{2} + \gamma \tag{7.8}$$

where the value of γ belongs to the interval $\left[0;\frac{1}{3}\right]$. By assuming γ=0 the modified Newmark methods coincides with the original Newmark method with constant average acceleration. Moreover, in order to obtain a stable solution, the following condition must apply in the PLAXIS code:

$$\alpha_N \geq \frac{1}{4}\left(\frac{1}{2}+\beta_N\right)^2 \qquad \beta_N \geq 0.5 \tag{7.9}$$

The standard setting of PLAXIS is the damped Newmark scheme with $\alpha_N = 0.3025,\ \beta_N = 0.6$, that correspond to $\gamma = 0.1$. Those values ensure that the algorithm is unconditionally stable, while being dissipative only for the high-frequency modes.

7.2 Impact load

In the analysis of the dynamic response of piles during driving, the pile is generally treated as an elastic bar along which the stress-waves travel axially. Numerical solutions of the one-dimensional wave equation with simple spring and dashpot soil models distributed along the pile are commonly available (Randolph, 1991).

Thus, during pile driving, the pile behaves like an elastic spring and by consequence the impact from the hammer does not act on the whole pile instantaneously, but rather takes a finite time to arrive at the pile tip.

The hammer impact creates a force pulse which travels down the pile at a speed $c = \sqrt{\frac{E}{\rho}} = 5122m/s$ for steel. This phenomenon is governed by one dimensional wave theory.

A downward stress wave is generated by the impact of the hammer and travels down the pile. The downward wave is modified and also partially progressively reflected upwards by the soil resistance. When the downward wave reaches the bottom end of the pile (at $t = l/c$), it reverses direction and becomes an upward wave. The amount and type of reflection depends on the soil behavior and strength at the tip of the pile.

The upward wave then travels up the pile and becomes a downward wave again when it reaches the top end of the pile (at $t = 2l/c$).

The first part of the downward wave, before the wave reaches the mud line, is only affected by the hammer and pile top characteristics. The second part of the signal shows the accumulated shaft skin friction. The portion just after $2l/c$ is related to the end bearing resistance.

Analysis of the dynamic response of a pile during driving requires, as input, the force-time signal generated by the hammer impact. In dynamic testing of piles, this signal may be measured directly by means of strain sensors attached near the head of the pile. Such data are not available at the design stage, however, it is necessary to assess an appropriate size and type of hammer in order to drive the piles to the required penetration, within a reasonable blow count and without generating excessive compressive or tensile stresses in the pile. This aspect of design is known as a “driveability study”.

Usually, the force response at the head of a pile for a drivability study is computed through a numerical model of the hammer. However, Deeks and Randolph (1993) have proposed relatively simple hammer models which provide a sufficiently accurate representation of the force-time response (*Figure 82*).

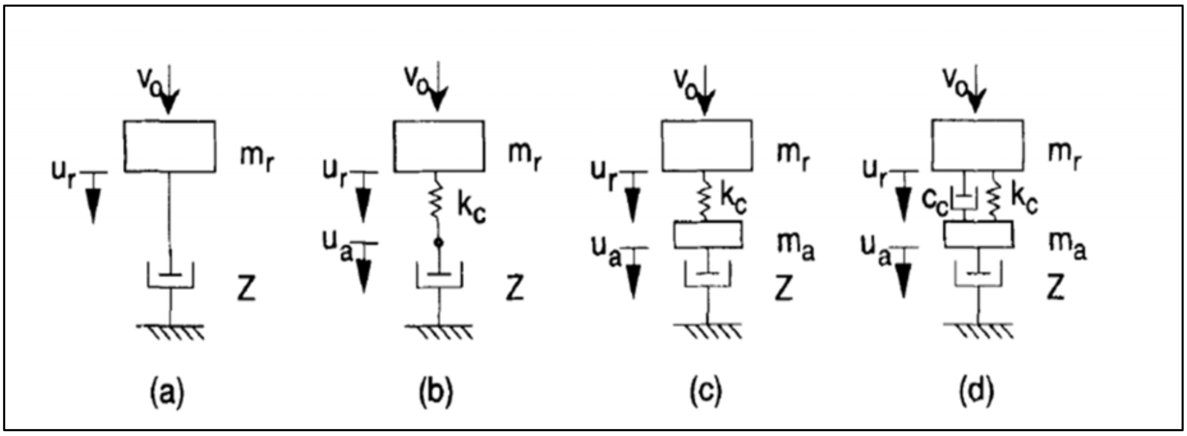

Figure 82. Analytical pile hammer models (Deeks & Randolph, 1993)

These models are useful to understand the influence of the various parameters involved in the generation of the signal.

For example, a variation in V_0 (ram velocity) changes the vertical magnitude of the stress wave while the wave shape remains the same; a changing in m_r (ram mass) makes the stress pulse decay more slowly with time while it has no effect on the initial slope of the wave; an increasing in Z (pile impedance) makes the peak stress pulse higher and decay more rapidly with time.

Since the goal is to have the shape of a force-time signal which arrives at the bottom of the pile in order to apply it on the flint, it is necessary to use a software based on the one dimensional wave theory as GRLWEAP (Goble & Rausche, 1999).

Thanks to this software it is possible to extract a variable versus time in any section of the pile. The engineering elements needed are the soil, the hammer, and the pile properties. *Figure 83* shows the interface of the software with the used parameters.

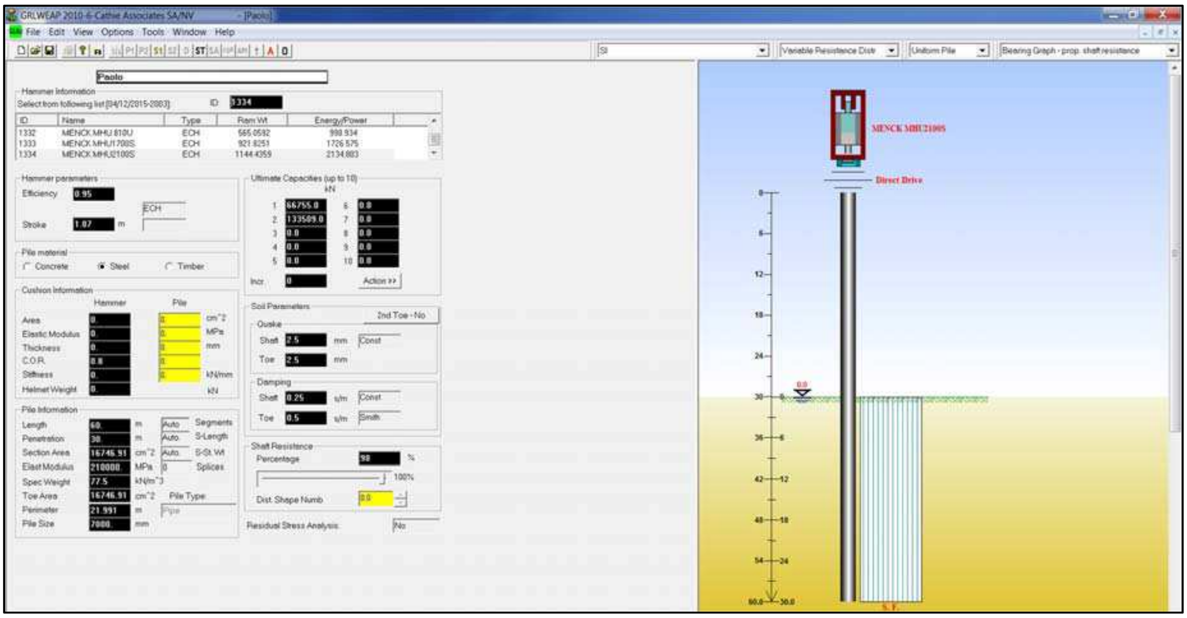

Figure 83. GRLWEAP screenshot

Referring to the soil resistance, the total capacity of the pile has to be calculated in order to perform the analysis. The method used is based on API recommendations (API, 2011):

- unit shaft resistance: $f_s = \alpha\, S_u$ (α is a factor which should be taken as 0.5 for $Su > 72kPa$ according to the alternate method, API);
- unit toe resistance: $q_t = 9\, S_u$.

An undrained shear strength is assumed equal to 100 kPa for this calculation.

Moreover, the quake and the damping parameters has to be added inside the model, both for the shaft that for the toe. The damping coefficients and quake factors used for the analyses have been selected according to the recommendations by Roussel (1979). For the side damping, Roussel provides damping values for different soil types ranging from 0.1s/m to 0.26s/m, excluding soft clay. Side damping equal to 0.25s/m (on the high side of the provided range) has been selected in the absence of specific recommendations for chalk.

Concerning the pile, a diameter of 7m is assumed (monopile) and a minimum wall thickness is assigned based on the API recommendations. In fact, the *D/t* ratio of the entire length of a pile should be small enough to preclude local buckling at stresses up to the yield strength of the pile material. For piles that are to be installed by driving where sustained hard driving is anticipated, the minimum piling wall thickness used should not be less than:

$$t = 6.35 + \frac{D}{100} \qquad D = diameter\ in\ mm;\ t = thickness\ in\ mm$$

A thickness of 77 mm is obtained.

The Menck MHU 2100S hydraulic hammer (*Figure 84*) is chosen based on previous experiences of large pile driving in similar conditions.

Figure 84. Menck MHU 2100S (menck.com)

In *Table 10* the parameters used are summarized.

Table 10. GRLWEAP input parameters

Hammer	Menck MHU
Unit shaft resistance	50 kPa=0.5 Su
End bearing resistance	900 kPa=9 Su
Side quake	2.5 mm
Toe quake	2.5 mm
Side damping	0.25 s/m
Toe damping	0.5 s/m
Pile diameter	7 m
Thickness	77 mm
Shaft Resistance	97.7 %
Length	60 m
Penetration length	30 m

With this data, the analysis has been performed and the top and bottom force are found, which are reported in *Figure 85-86-87*.

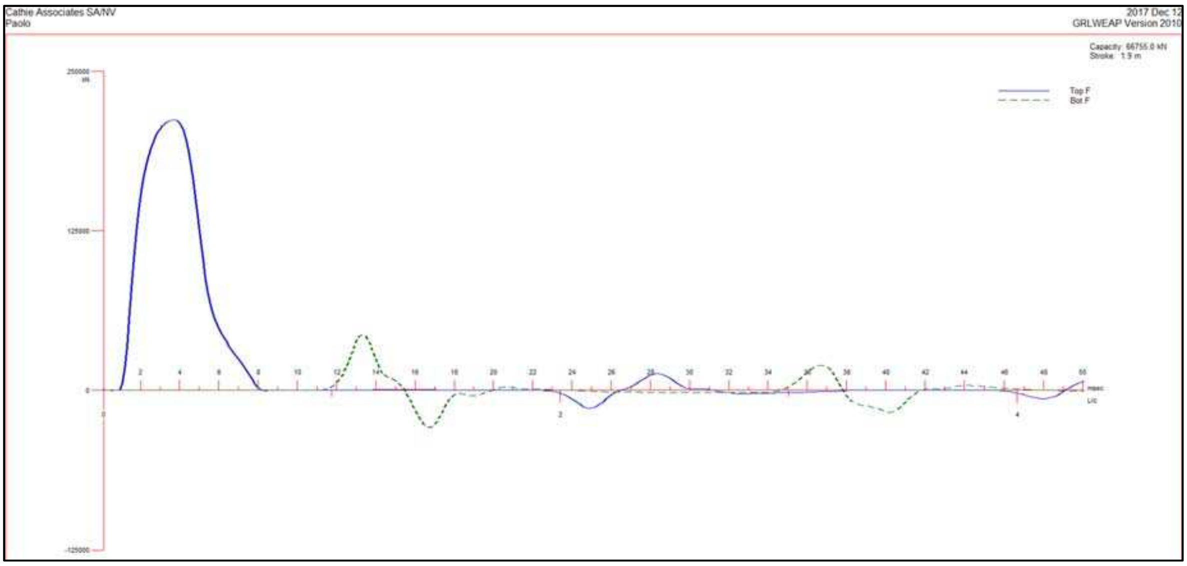

Figure 85. GRLWEAP Top and Bottom force vs. time

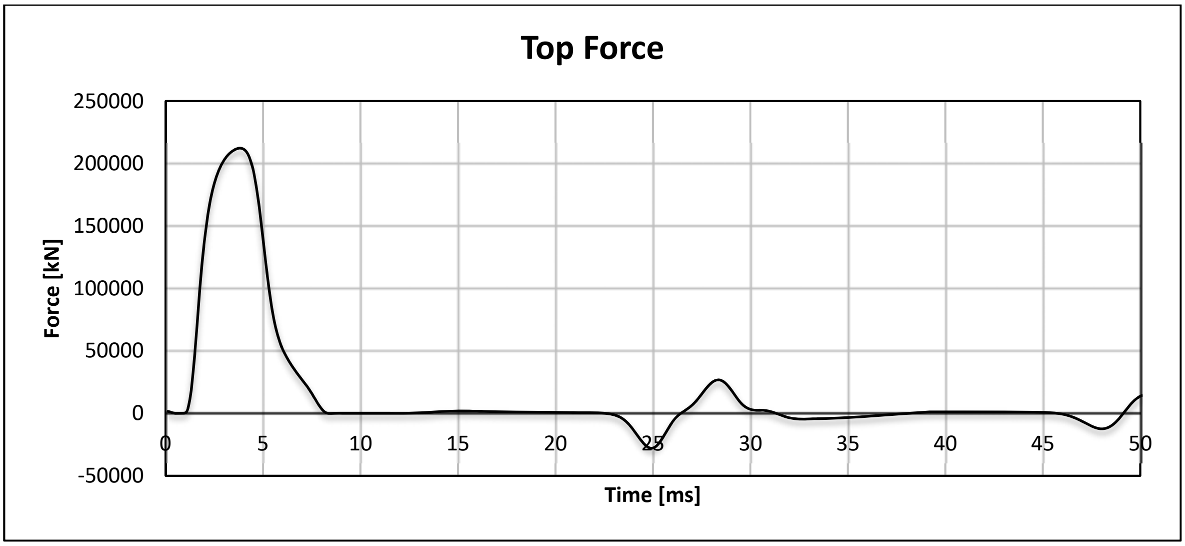

Figure 86. Top force vs. time

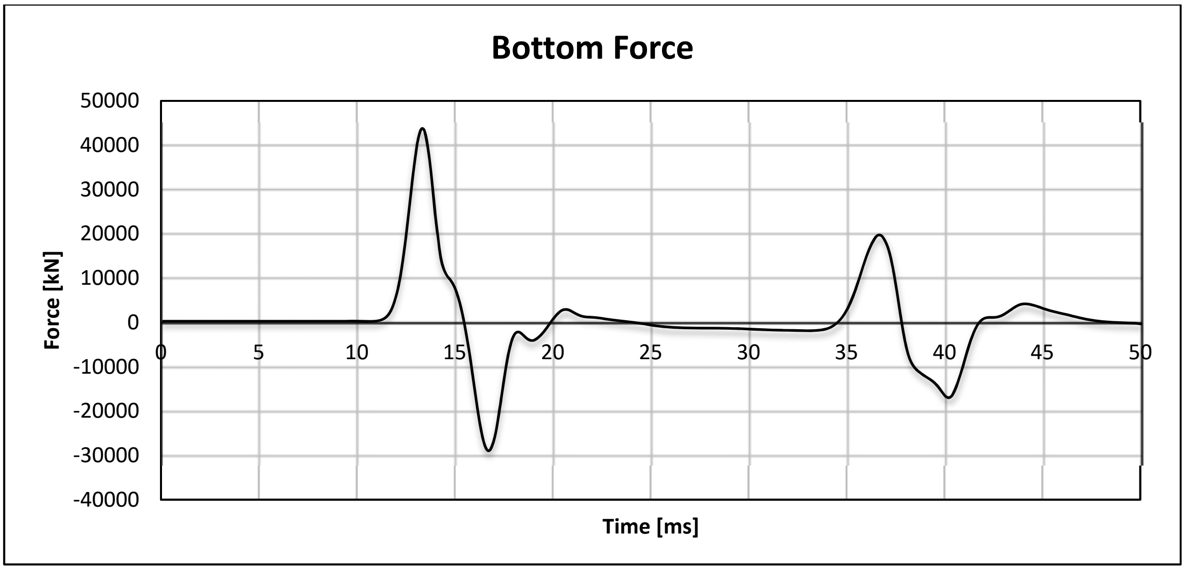

Figure 87. Bottom force vs. time

The compression force that arrives at the bottom of the pile during driving is transmitted by contact to the flint, with a similar shape. This is justified if it is assumed that the boulder interaction does not affect the global behaviour of the pile but only the local one (see §7.4.3). Otherwise, the bottom signal could be influenced by the significant toe resistance increasing, and by consequence the presence of the boulder should be considered even in the GRLWEAP analysis. So, the first part of the curve in *Figure 87* (compression/positive force at the bottom) is then isolated and normalized in order to use it as the input shape force to apply on the flint (*Figure 88*).

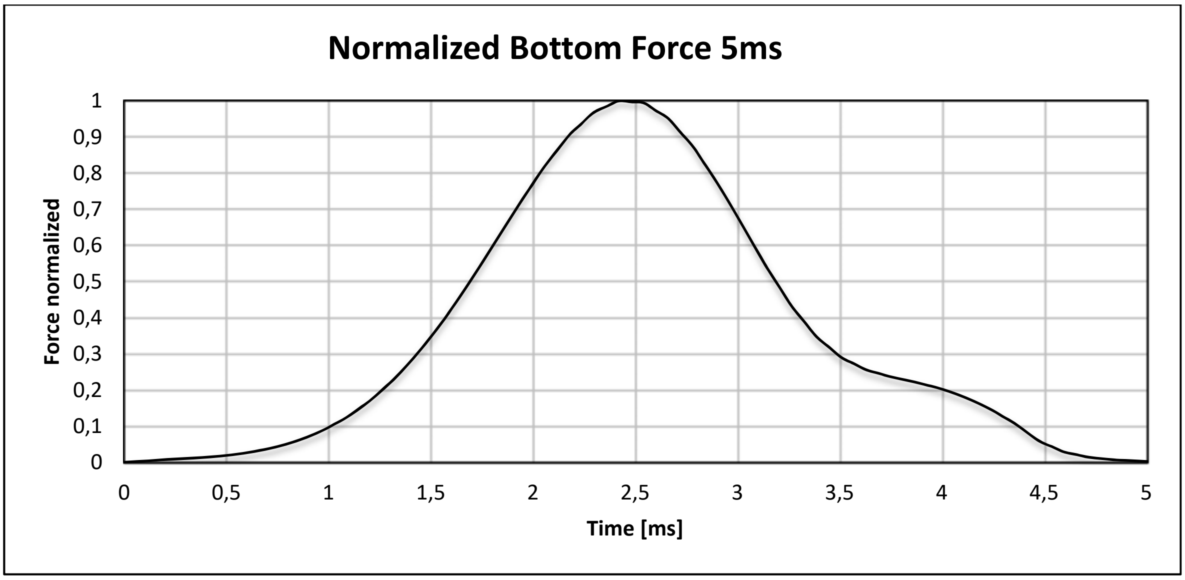

Figure 88. Input dynamic multiplier/normalized bottom force vs. time

In PLAXIS, the dynamic load is activated by means of dynamic load multipliers which can be read from a ASCII file containing time and load multiplier in two columns separated by a space (see Appendix B 10.2). The active load that is used in a dynamic calculation is the product of the input value of the load and the corresponding dynamic load multiplier:

$$active\ load = input\ load \cdot dynamic\ multiplier$$

Thus, by changing the input load it is possible to scale the active load by using the same shape.

7.3 Numerical model

7.3.1 Geometry and analysis

The size of the model should be chosen big as much as to avoid influences from boundary restraints. From the previous static analysis (see Chapter 5), it is found that only a zone of 1.5 diameter from the center of the flint is involved in the soil flow and plasticizes. Since a dynamic finite element analysis requires a high computational time, it is important to reduce as possible the dimension of the model. So, for the following analyses the side of the model is chosen equal to 20 flint diameters, which results enough to not affect the results by boundary restraints.

The static boundary conditions are set as normally fixed. So the top of the model results free, the bottom vertically fixed and the two sides horizontally fixed.

In the middle of the model a circular embedded flint is built with rigid interface elements (R_{inter}=1) around in order to allow relative displacements. A sensitivity analysis on the interface thickness has been performed to assess its influence on the results. Each interface has assigned to it a "virtual thickness" which is an implicit dimension used to define the global behaviour of the interface; the higher it is and the more elastic displacements are generated. In general, interface elements are used to model contacts and material discontinuities which supposed to generate limited deformation in the normal direction and therefore the virtual thickness should be kept small. On the other hand, if the virtual thickness is too small, numerical ill-conditioning may occur. Since the thickness is calculated based on a virtual thickness factor, two values are explored: the default value 0.1 and the lowest value 0.01. Three analysis has been compared and the results show differences lower than 1% (see Appendix C 10.3). Thus, it can be concluded that the interface thickness has not a great influence on this model and that the default value can be acceptable.

The analyses have been done in a plane strain condition. Thus, the flint is considered as an infinite long cylinder and by consequence all the results will be referred to a 1 m length. The outputs are obtained from the curve of the dynamic-time versus vertical-displacements, as the permanent displacement of a point on the flint (where the force is applied) when the oscillation is ended.

A parametric analysis is done to obtain a database of peak forces and related permanent displacements, from which derive a law by an interpolation. Three different flint diameters are analyzed (0.25m, 0.5m, 1m) and by consequence 3 different models are built in order to guarantee a correct dimension. Then, 3 embedding materials are used (Chalk 1, Chalk 2, Chalk 3), with different strength and stiffness characteristics (see §7.3.3) based on the data found in literature (see §2.2.4). Finally, 5 peak forces are adopted (1000kN, 2000kN, 3000kN, 4000kN, 5000kN), by scaling the same shape of the force multiplier provided with GRLWEAP (see §7.2).

The combination of the above results in a database of 45 permanent displacements versus peak forces, both for a centered force and for a lateral force, as summarized in *Table 11*.

Table 11. Parametric analysis data

	D [m]	Dimension	Material	Peak forces [kN]	Output
Model 1	0.25	5x5 m	Chalk 1, 2, 3	1000 2000 3000 4000 5000	15 permanent displacements for each model→45
Model 2	0.5	10x10 m	Chalk 1, 2, 3		
Model 3	1	20x20 m	Chalk 1, 2, 3		

Regarding the lateral force, an angle of 45° was chosen because from the static analyses it is shown that it is the conditions with the highest horizontal force (see §5.6); moreover, it is also an intermediate condition between a centered and a tangential contact (0° and 90°). Only 2 positions are analyzed because, since it is not possible to know where the pile will hit the flint, only the worst conditions should be taken into account. In fact, the highest vertical force arises if the pile hits the flint perfectly in the middle. On the contrary, the highest horizontal force arises if the pile hits the flint at about 45-50°. In order to compute the horizontal force in the lateral contact, a fixed-end anchor with an infinite stiffness ($EA = 100E33$) is added to the model at the point load. This simulates the horizontal restrain provided by the pile and it allows to obtain easily the value of the horizontal force.

7.3.2 Mesh

The accuracy of the calculation results depends both on the size and distribution of the elements in the mesh. In PLAXIS the mesh generation is based on a robust triangulation procedure. In the case of a dynamic analysis, the size of the elements needs to be chosen based on the characteristics of both the soil and the input signal.

Kuhlemeyer and Lysmer (1973) suggest to assume an average element size less than or equal to one-eight/one-ten of the wavelength associated with the maximum frequency component of the input wave (i.e. the highest frequency component that contains appreciable energy).

Figure 89 shows the frequency content of the impact force, which is obtained by doing the Fourier transform of the relative time-history. The energy in the spectrum is spread out continuously over a range of frequencies rather than being concentrated only at specific frequencies. This is a characteristic of transients signals. Since the shorter the impulse the greater its high frequency content, if the impulse were infinitely short (the so-called delta function, in mathematics), then its spectrum would extend from 0 to infinity in frequency. In this case, it can be seen that the frequency content of the force is mainly dominated by frequencies below 300Hz.

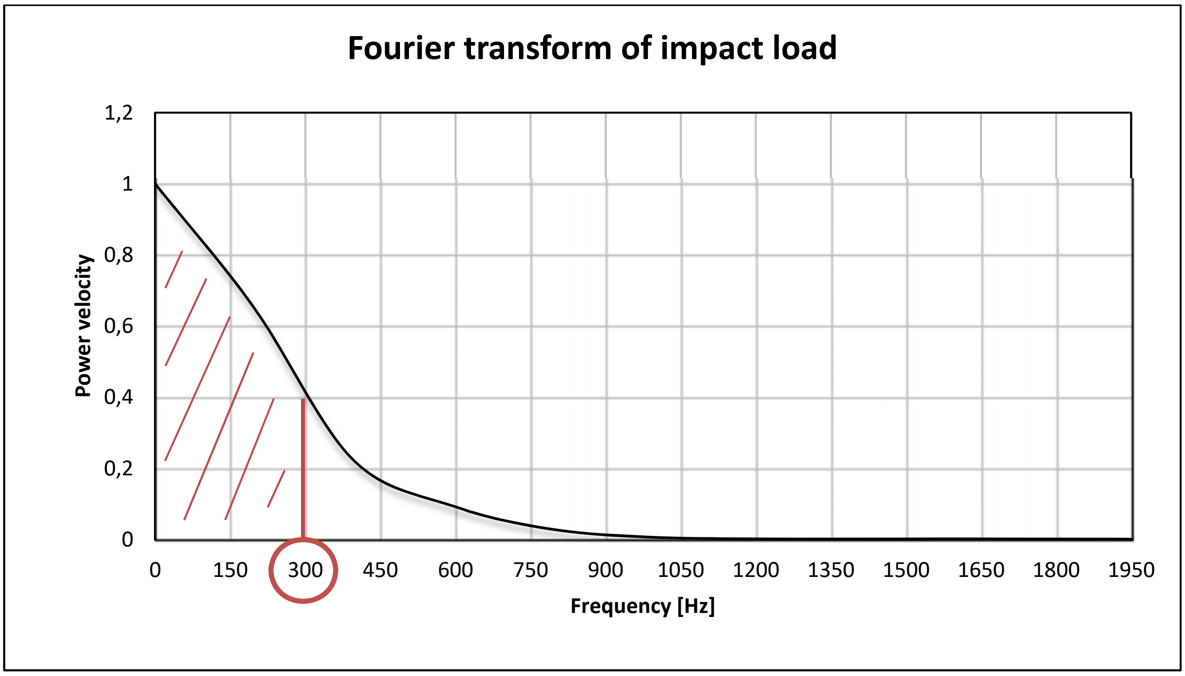

Figure 89. Fourier transform of impact load

The $V_{S,min}$ is related to the less stiff embedding material (Chalk 1) which has a Young's modulus of 100 MPa. By consequence the shear wave velocity is equal to 150 m/s ($V_S = \sqrt{G/\rho} = \sqrt{33500/1.5} = 150$).

So, near the flint (at least until 2 diameters around) the average size should be lower than:

$$\frac{\lambda}{10} = \frac{Vs_{min}}{10\ f_{max}} = \frac{150}{10 \cdot 300} = 5\ cm \qquad 7.10$$

The size of the triangular elements needs to be controlled and the mesh refinement allows to get a specific value for the average length of the element side.

The mesh generator requires a global meshing parameter that represents the target element size I_e. In PLAXIS this parameter is calculated from the outer geometry dimensions (x_{min}, x_{max}, y_{min}, y_{max}) and the element distribution selected. The target element dimension is calculated according to the formula:

$$I_e = \frac{n_c}{12}\sqrt{(x_{max} - x_{min})(y_{max} - y_{min})} \qquad 7.11$$

In this case, the target element has to be maximum 5cm and since the geometry is known, the relative element size factor n_c can be calculated for each geometry model. The values are reported in *Table 12*:

Table 12. Relative element size for different model

	Model 1	**Model 2**	**Model 3**
n_c	0.03	0.06	0.12

Around the flint the mesh is refined by adding a series of polycurves (*Figure 90*) to achieve the best quality of the finite elements and to refine the mesh only where high strain gradients are expected. The mesh is then defined by using Expert setting which allows to specify the value of the relative element size factor previously calculated; this value is gradually decreased with the distance from the flint. *Figure 91* shows the resulting generated mesh.

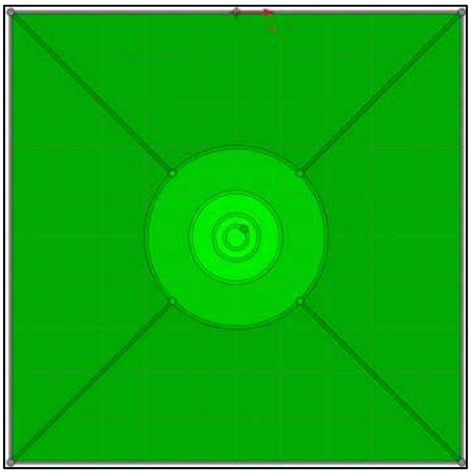

Figure 90. Mesh refinement with polycurves

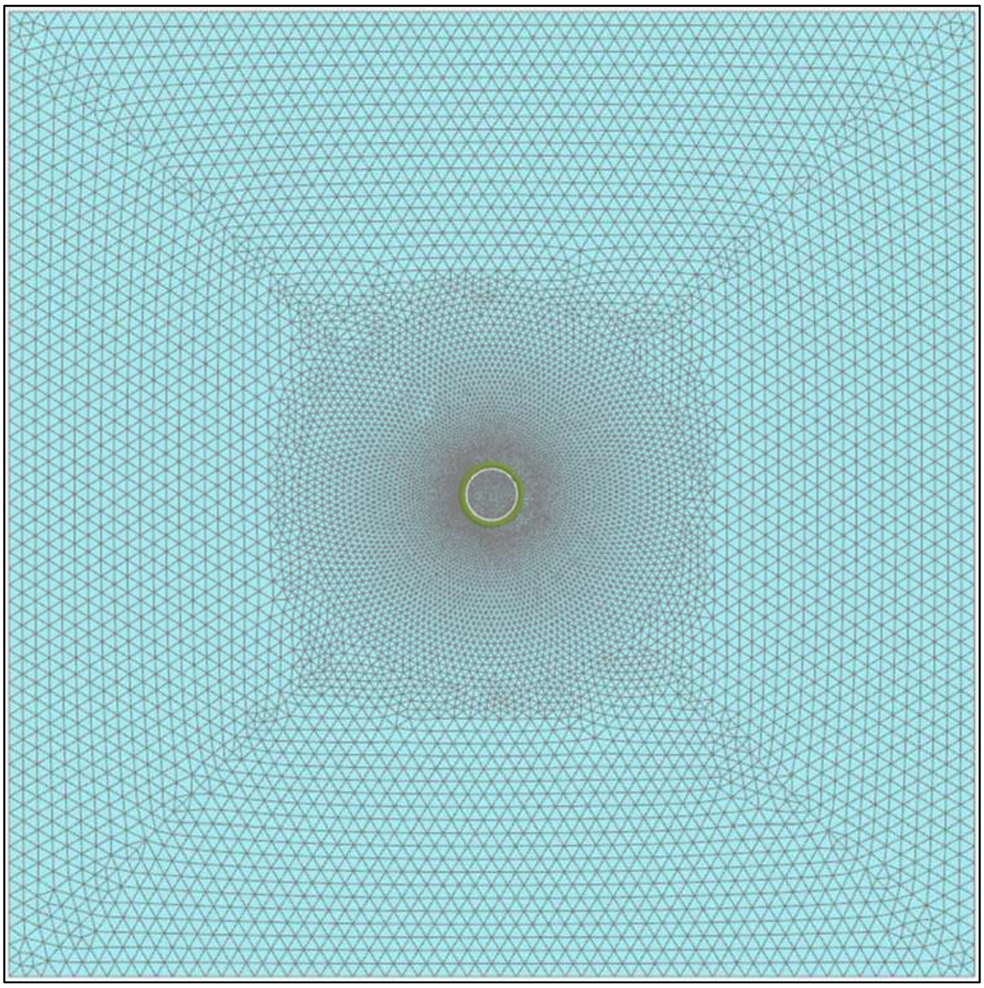

Figure 91. Generated mesh

7.3.3 Material

In Chapter 2, the properties of chalk and flint are described based on a literature review. The obtained parameters are now used in the finite element model.

Referring to the chalk, a grade D (i.e. low density, high porosity) is considered. This is a weathered chalk which is usually found in subsea layers where piles are installed. Pile driving in this type of soil does not present particular problems and it is relatively easy. Anyway, the presence of the flint could seriously damage the pile wall.

The dry density of this type of material is lower than 15.5 kN/m and in this study is assumed equal to 15 kN/m. Since its high porosity (around 40%), the saturated unit weight is:

$$\gamma_{sat} = 15 + 0.4 \cdot 10 = 19\ kN/m^3$$

The initial state of stress is obtained with a K_0=1, since this value has no influence on the problem studied.

The chalk is modelled in PLAXIS with the Mohr-Coulomb model in an Undrained C conditions. The undrained condition is justified by the fact that during the driving process the load is applied very fast and so the pore pressure generated cannot dissipate. Moreover, the reported strength parameters for intact chalk tested in the Hoek triaxial cell (Saffari-Shooshtari, 1989) show that porosity chalks behave as undrained clay (see *Figure 8*).

In this model (Undrained C) there is no difference between the dry and saturated unit weight. Since the study is done for offshore purpose, the unit weight considered will be the saturated one.

The Undrained C model enables simulation of undrained behaviour using a total stress analysis with undrained parameters. In that case, stiffness is modelled using undrained Young's modulus E_u and an undrained Poisson's ratio ν_u, and strength is modelled using an undrained shear strength S_u.

The value of UCS for a grade D chalk should be lower than 3000 kPa (Lord, et al., 2002) and by consequence the S_u lower than 1500 kPa. So, 3 different undrained shear strengths are explored: $S_{u,1}$=100kPa, $S_{u,2}$=500kPa, $S_{u,3}$=1MPa. Regarding the stiffness, a ratio E_u/S_u=1000 is assumed. This it is consistent with the order of 1 GPa of the intact Young's modulus for high porosity chalk provided by Lord (2002) and also with the correlations for clay with IP<30 (Jamiolkowski, 1979). Thus, $E_{u,1}$=0.1GPa, $E_{u,2}$=0.5GPa, $E_{u,3}$=1GPa are the used values.

Concerning the Poisson's ratio, in an Undrained C analysis is typically selected a value close to 0.5 (between 0.495 and 0.499) because a value of exactly 0.5 is not possible, since this would lead to singularity of the stiffness matrix. However, when using the Mohr-Coulomb model in dynamic calculations, the stiffness parameters need to be selected such that the model predicts the correct wave velocities in the soil. In fact, P-wave velocity in a linear elastic material depends on the constrained modulus and on the density:

$$V_P = \sqrt{\frac{E_{oed}}{\rho}} \qquad E_{oed} = E\,\frac{1-v}{(1+v)\,(1-2v)} \qquad 7.12$$

In a saturated porous media, according to Biot theory[4] (Biot, 1956) and assuming the incompressibility of the grain, the velocity could be calculated as:

$$V_P = \sqrt{\frac{\left(K_{Sk} + \frac{4}{3}G\right) + \frac{K_W}{n}}{\rho}} \qquad \rho = (1-n)\rho_s + n\rho_w \qquad 7.13$$

In an Undrained C model in PLAXIS, only E_u and v_u are entered as stiffness parameters and the P-wave velocity is calculated as:

$$V_P = \sqrt{\frac{E_{oed,u}}{\rho_{sat}}} \qquad E_{oed,u} = E_u\,\frac{1-v_u}{(1+v_u)\,(1-2v_u)} \qquad 7.14$$

Since the compressibility of the water and the porosity (n) of the soil are not taken in account in the calculation, this could lead to velocities which are not representative of the problem. For example, for a chalk of an E_u=500MPa and a ρ=1900kg/m^3, if a v_u=0.499 is assumed the resulting V_P would be equal to 6629 m/s, which cannot be real.

[4] "A theory is developed for the propagation of stress waves in a porous elastic solid containing a compressible viscous fluid. The emphasis of the present treatment is on materials where fluid and solid are of comparable densities as for instance in the case of water-saturated rock". Biot, 1956

P-wave velocity measurements have been reported by Masson (1973) and these indicate values which vary between 1300 to 2800 m/s. In the water V_p=1500 m/s, so in a porous saturated soil, velocities higher than 1500 m/s (water wave propagation) are expected and they cannot be lower than that value even in low stiffness soil.

The V_p is very sensitive to the variation of Poisson's ratio and in this way it is possible to calibrate correct velocities without changing a lot other parameters and by consequence without having a significant influence in the deformation response of the soil.

So, in order to obtain consistent velocities, the Poisson's ratio is slightly decreased. This is justified because, according to Skempton's theory (Skempton, 1954), the undrained Poisson's ratios could be calculated as:

$$v_u = \frac{3v' + B(1-2v')}{3 - B(1-2v')} \qquad B = \frac{1}{1 + \frac{n\,K'}{K_w}} \tag{7.15}$$

B is approximately equal to 1.0, since the bulk modulus of the soil structure K' (order of MPa) is negligible with respect to that of the fluid K_w (order of GPa). Thus, in saturated soft and medium soils, B is increasing until it becomes equal to 1.0, meaning that all load is taken by the pore fluid and the specimen is fully saturated. However, for rock, K' could be on the order of GPa and it is comparable to the bulk modulus of the saturating fluid, such as water ($K_w = 2.24\ GPa$). It means that rock stiff framework feels the applied mean stress at least as much as the pore fluid, hence the Skempton's coefficient for rock can be significantly smaller than one (Skempton, 1954).

In conclusion, if the porosity is zero and/or if the soil structure is weak, B becomes equal to 1 and by consequence $v_u = 0.5$, while if the porosity and the skeleton stiffness increase B becomes lower than 1 and this corresponds to a smaller v_u.

If for the same chalk previously considered (E_u=500 MPa and a ρ=1900 kg/m^3) a v_u=0.490 is assumed instead of 0.499 (this corresponds to consider the porosity and the stiffness of the chalk), the resulting V_P becomes equal to 2100 m/s, which could be acceptable according to Biot theory (>1500 m/s) and experimental values.

Table 13 summarizes the selected properties of the 3 different materials:

Table 13. Chalk properties for numerical analysis

	γ_{unsat} [kN/m³]	S_u [kPa]	E_u [GPa]	ν_u	V_P [m/s]
Chalk 1	19.0	100	0.1	0.496	1475
Chalk 2	19.0	500	0.5	0.490	2102
Chalk 3	19.0	1000	1	0.485	2443

Concerning the flint, the modeling results more simple. In fact, the strength of this material is not taken into account since the aim of the project is to study the penetration inside the chalk and not the breakage of the flint. Thus, the flint is modelled as an infinite strength material by assigning a linear elastic non porous model. The stiffness parameters assumed are $E = 80\ GPa$ and $\nu = 0.125$ (see 2.3.4). The Young's modulus is different orders of magnitude higher respect to the chalk and so a variation of this value has no influence. Around the flint an interface is added in order to allow relative displacement. Its properties are assumed rigid ($R_{inter} = 1$), i.e. the same properties of the around chalk, and with a standard virtual thickness (see §7.3.3 and Appendix C 10.3 for thickness influence).

7.3.4 Damping

In dynamic engineering problems, the soil is subjected to cyclic shear loading, showing a nonlinear dissipative behaviour. Its stiffness decays with the increasing strain level induced by the loading, and the sequence of loading and unloading paths generates a hysteretic loop with dissipation of energy and consequent damping, as it is shown in *Figure 92*.

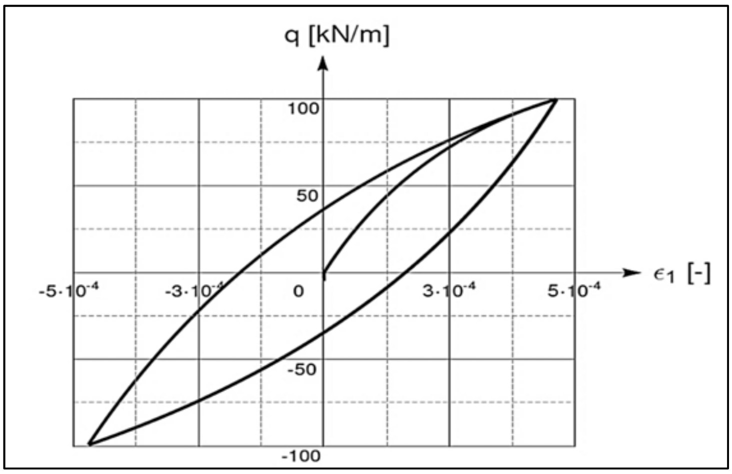

Figure 92. Hysteretic material behaviour (PLAXIS, 2014)

Some of the traditional constitutive models, as for example Mohr-Coulomb, cannot describe the hysteretic damping. Instead, the total amount of damping is introduced through the frequency-dependent Rayleigh formulation in terms of viscous damping, that has to be consistent with the level of strain induced by the dynamic load.

In PLAXIS it is possible to calculate the Rayleigh coefficients by entering proper values for the damping ratios and the target frequencies. To calibrate these two coefficients, it is necessary to define the target damping ratio and the related frequencies. Several strategies can be found in literature to select the appropriate frequencies (Laera & Brinkgreve, 2015).

Amorosi, Boldini and Elia (2010) suggest to consider the frequency interval characterized by the highest energy content. The procedure used is explained below.

If an impact load (5ms in this case) is applied on a flint embedded in a material without Rayleigh damping, a time-velocity curve can be provided from a numerical analysis. The vibratory motion consists of different frequencies occurring simultaneously and in the frequency spectrum the vibration signal is divided into individual components.

The frequency content is estimated by performing a Fast Fourier Transform (FFT). The frequency spectrum represents the frequency domain containing the intensity of all frequencies. The frequency content gives information about how the amplitude of a ground motion is distributed among different frequencies. This information is necessary since the dynamic response depends on both the amplitude of the applied loads and the frequency range in which the energy content is concentrated.

Thus, by applying the Fourier transform on the free oscillation part (after the impact) of the time-velocity curve (see Appendix D 10.4) the spectrum is obtained and the frequency content of the flint oscillation can be analyzed.

The power spectrum depends on the stiffness of the material and on the flint diameter. *Figure 93-94-95* show the obtained spectrums:

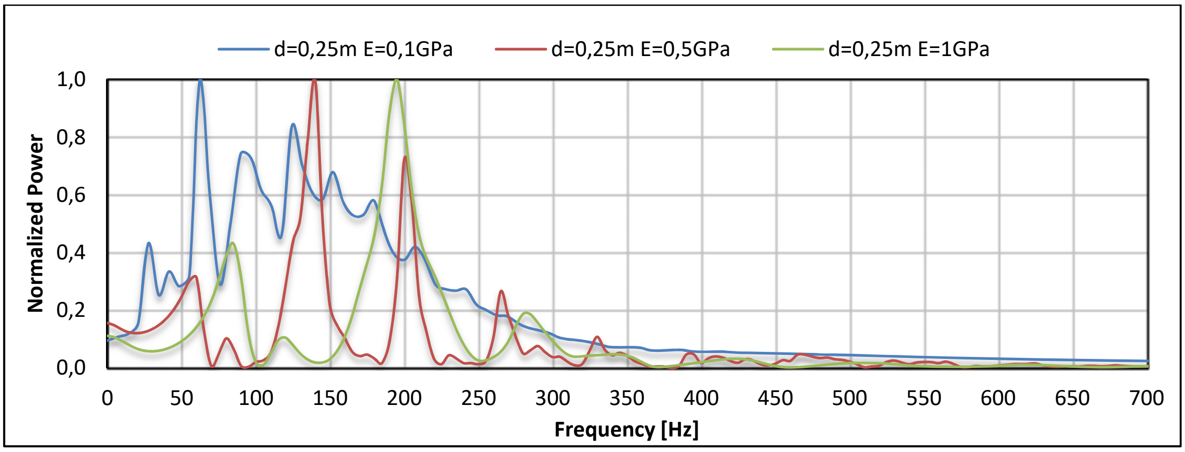

Figure 93. Power spectrum d=0.25m

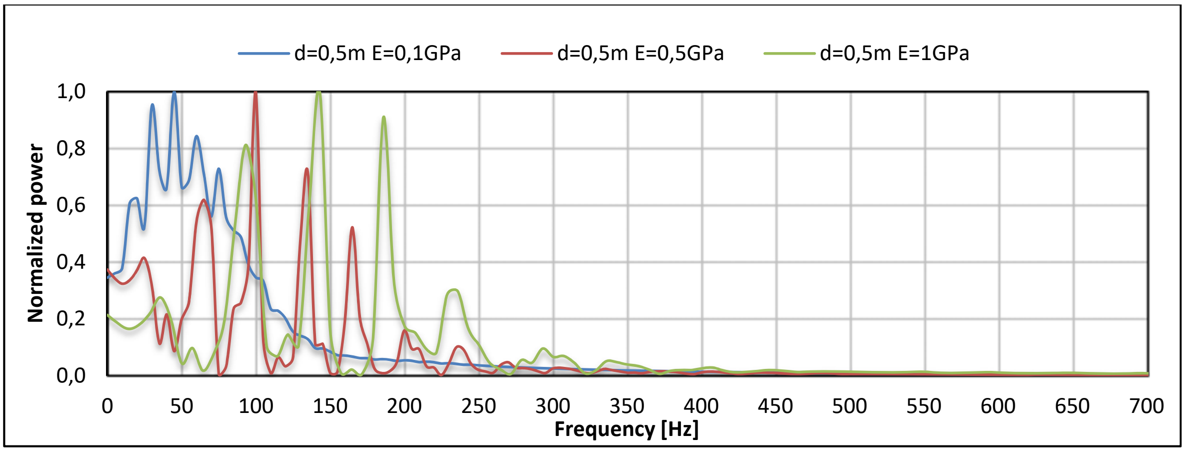

Figure 94. Power spectrum d=0.5m

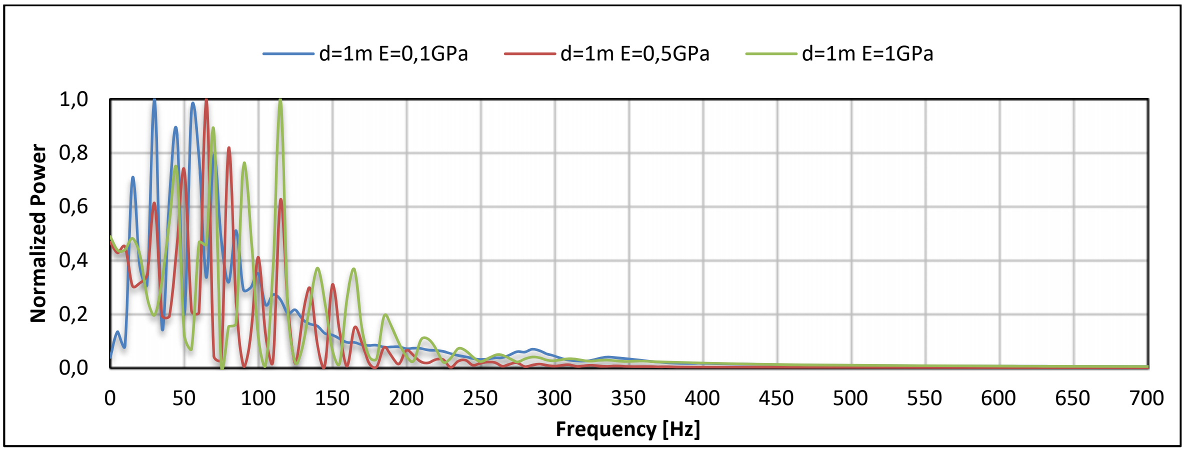

Figure 95. Power spectrum d=1m

It is notable that if the diameter increases the range moves to lower frequencies. This means that a big flint oscillates with a lower frequency than a small one. On the contrary, if the elastic modulus increase, the range moves to higher frequencies. So, in a stiff chalk, an impacted flint will oscillate with a higher frequency than in a softer one.

In this work, for each diameter a different frequency range is assumed, in order to include the majority of the energy content of the three-modelled materials. A band of 150 Hz is selected on the basis of the spectrums and translated where the energy content is more important.

It is extremely difficult to define correct values for the Rayleigh damping because it is not known the exact damping that is introduced in the model by numerical damping and irreversible soil deformations. Nevertheless, the same Rayleigh damping parameters were defined and numerical damping was also introduced in the model. Thus, Rayleigh damping values equal to 5% are assumed for both the target frequencies, which is a value typically used (Amorosi, et al., 2010) in absence of specific recommendations for chalk.

Table 14 summarizes the frequencies and the Rayleigh parameters obtained from the power spectrum of the three different geometries (d=0.25, 0.5, 1 m) and materials.

Table 14. Rayleigh parameters

d [m]	f_n [Hz]	f_m [Hz]	D_R [%]	α_R	β_R
0.25	**45**	**195**	**5**	**22.9**	**0.066E-3**
0.5	**30**	**180**	**5**	**16.2**	**0.074E-3**
1	**15**	**165**	**5**	**8.6**	**0.088E-3**

The corresponding Rayleigh coefficients α_R and β_R are derived from equation, for the frequency interval $f_n - f_m$ (they are the target frequencies for which a damping value has to be specified in order to calibrate Rayleigh parameters) characterized by the highest energy content.

The coefficients are obtained considering the following relationship with the damping ratio D (Clough & Penzien, 1993):

$$\begin{Bmatrix} \alpha_R \\ \beta_R \end{Bmatrix} = \frac{2D_R}{\omega_n + \omega_m} \begin{Bmatrix} \omega_n \omega_m \\ 1 \end{Bmatrix} \qquad 7.16$$

where ω_n and ω_m are the angular frequencies related to the frequency interval $f_n - f_m$ in which the viscous damping is equal to or lower than D.

The damping parameters can be automatically calculated by the software when the target damping ratio and the target frequencies are specified. *Figure 96* shows the damping ratio as a function of the frequency.

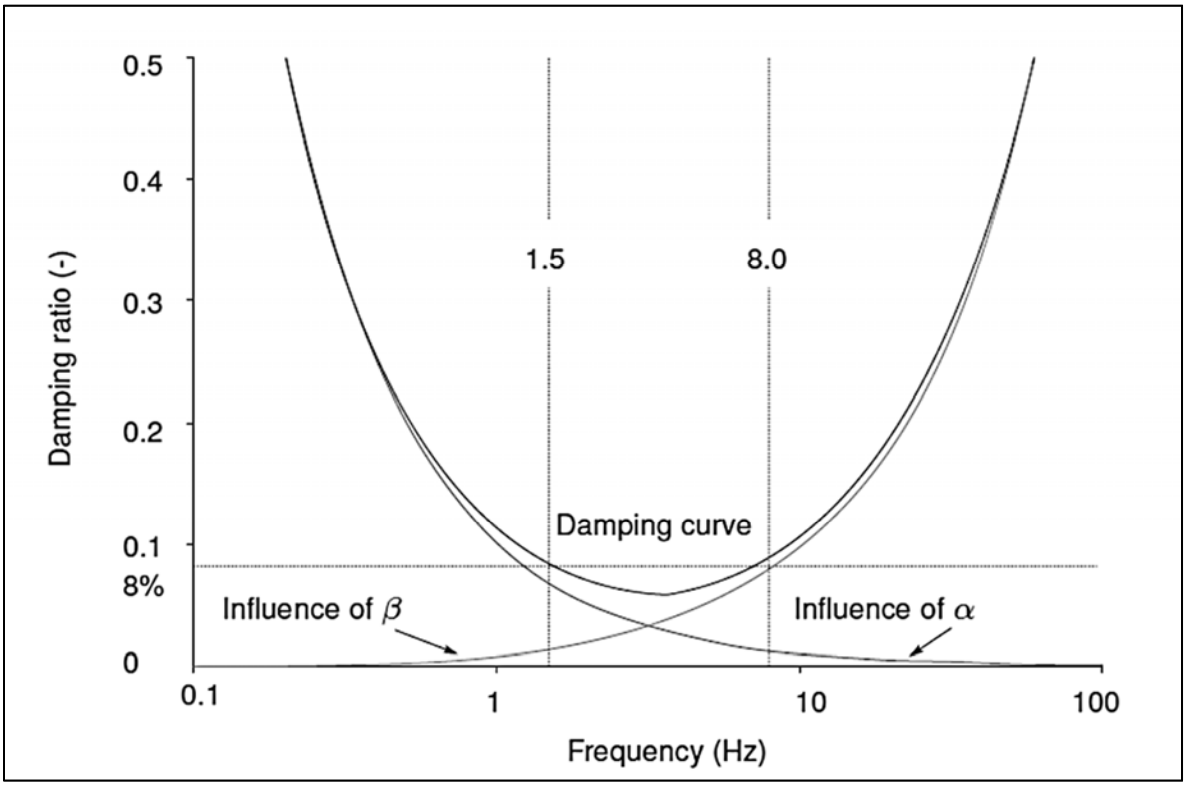

Figure 96. Rayleigh damping parameters influence (PLAXIS, 2014)

α_R is the parameter that determines the influence of the mass in the damping of the system. The higher it is, the more the lower frequencies are damped. β_R is the parameter that determines the influence of the stiffness in the damping of the system. The higher it is, the more the higher frequencies are damped. The same plot is reported in *Figure 97* for the specific frequencies of a 0.25m-diameter and for a damping value of 5%.

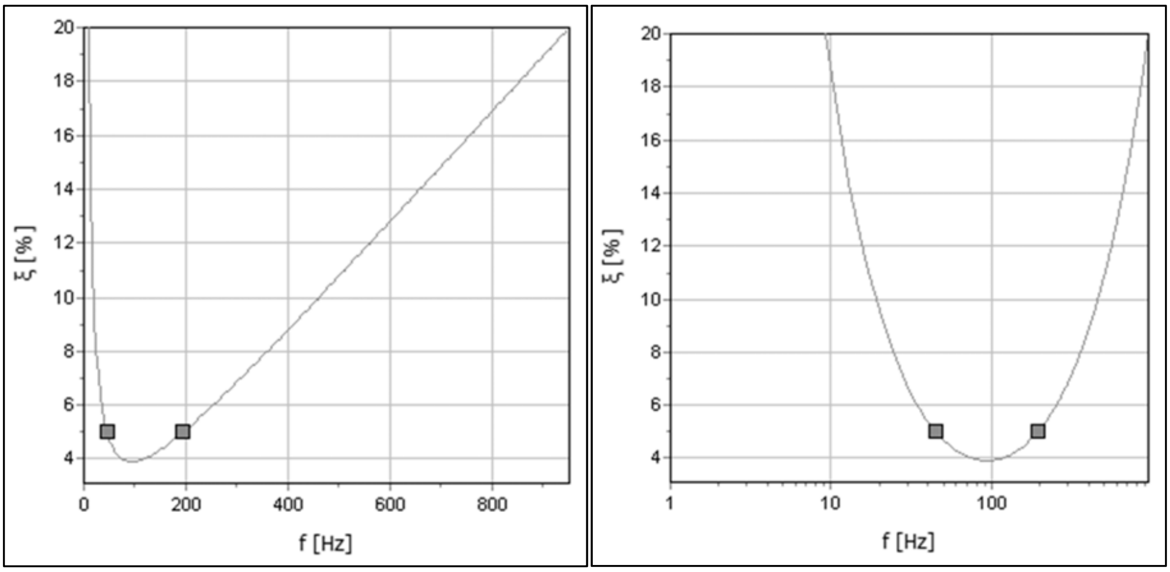

Figure 97.Rayleigh damping curves for d=0.25m

Another damping is also introduced in the model in order to provide accurate results on the first oscillations modes, to dissipate high frequencies oscillations and to reduce numerical instabilities in the soil: the numerical damping. In fact, the direct integration of the equilibrium equations originates high frequency modes overlapped with the main solution, so called numerical noise. As implicit integration methods try to provide accurate results of the first vibration modes, the high frequency modes should be interpreted as spurious reflections. Thus, it is advantageous to include some numerical damping in order to dissipate the high frequency oscillations. Despite that, numerical damping should only be added if the accuracy of the results is reduced. According to literature studies, in the Newmark implicit method (Newmark, 1959), numerical damping is imposed in the model when the Newmark parameter β_N is larger than 1/2.

The standard setting of PLAXIS is the damped Newmark scheme with $\alpha_N = 0.3025,\ \beta_N = 0.6$.

Finally, radiation damping at the boundaries shall be considered. Viscous boundaries are therefore used to represent the radiation damping (wave propagations for the far field). They are introduced at the 2 sides and at the bottom in order to avoid the effect of the reflection of waves, assuming the standard values of the Lysmer and Kuhlemeyer relaxation factor $C_1 = 1,\ C_2 = 0.25$ (Lysmer & Kuhlemeyer, 1969).

7.3.5 Dynamic stages

The dynamic equations of motion are integrated based on time-step schemes characterized by calculation features related to the accuracy, numerical damping and stability (the number of steps and substeps, the Newmark damping coefficients and the mass matrix, among the others). The automatic procedure implemented in PLAXIS ensures that a wave does not cross more than one element per time step: the critical time step is first estimated according to the element size and the material stiffness, then the time step is adjusted based on the number of data points specified as dynamic multipliers.

The time step used in a dynamic calculation is given by:

$$\delta t = \frac{\Delta t}{m\ n} \tag{7.17}$$

where Δt is the dynamic time interval parameter, i.e. the duration of the impact load (5ms in this case), n is the number of dynamic sub-steps and m is the number of maximum steps. PLAXIS automatically calculates the proper number of sub-steps n, for a given number of steps m. It is advised to set the number of maximum steps at least equal to the number of multipliers that define the input signal (it is defined by a multiplier for each time step). For each time step PLAXIS calculates the number of sub-steps necessary to reach the estimated end time with a sufficient accuracy.

Each analysis consists mainly in three calculation phases. In the first phase the flint is created within the chalk and the initial stresses are generated. In the second phase the flint is subjected to a single stroke, which is simulated by activating the dynamic multiplier previously defined (see §7.2). In the third phase, the load is kept zero and the dynamic response of the flint and soil is analyzed in time. The last two phases involve dynamic calculations.

The first dynamic phase has a time interval Δt of 5ms which is the duration of the stroke, a number of steps m equal to 100 (the input signal is defined by 85 multiplier) and a number of sub-steps equal to 1. The second dynamic phase has a time interval Δt of 200ms because after no more flint oscillation are present (from preliminary analysis), a number of steps m equal to 1000 and a number of sub-steps equal to 2 (parameters suggested by the software).

A total of 45 analyses are performed because 3 diameters, 3 chalk types and 5 peak forces are explored ($3 \cdot 3 \cdot 5 = 45$). For each of these analyses a permanent displacement can be obtained. The aim is to found a law which allows to predict displacements for given peak force and material characteristics.

The analyses have been done for a centered force (the pile hits the flint in the middle) and for a lateral force (the pile hits the flint on the side placed at 45°).

7.4 Results

7.4.1 Time-displacement curves

From the numerical analyses, it is possible to plot the dynamic time versus the displacement of a point on the flint selected before the analysis, for example as reported in *Figure 98* for different peak forces. In the first part of the curve, until 5ms, the displacement is due to the application of the load. Then, the load is removed and the flint starts to oscillate with a frequency dependent of its diameter and of the elastic modulus of the embedding material. A small part of the displacement is elastic and so it is recovered. On the contrary, a permanent displacement occurs due to plastic deformations. After about 0.1 seconds the oscillation stops and the permanent displacement of the flint can be obtained.

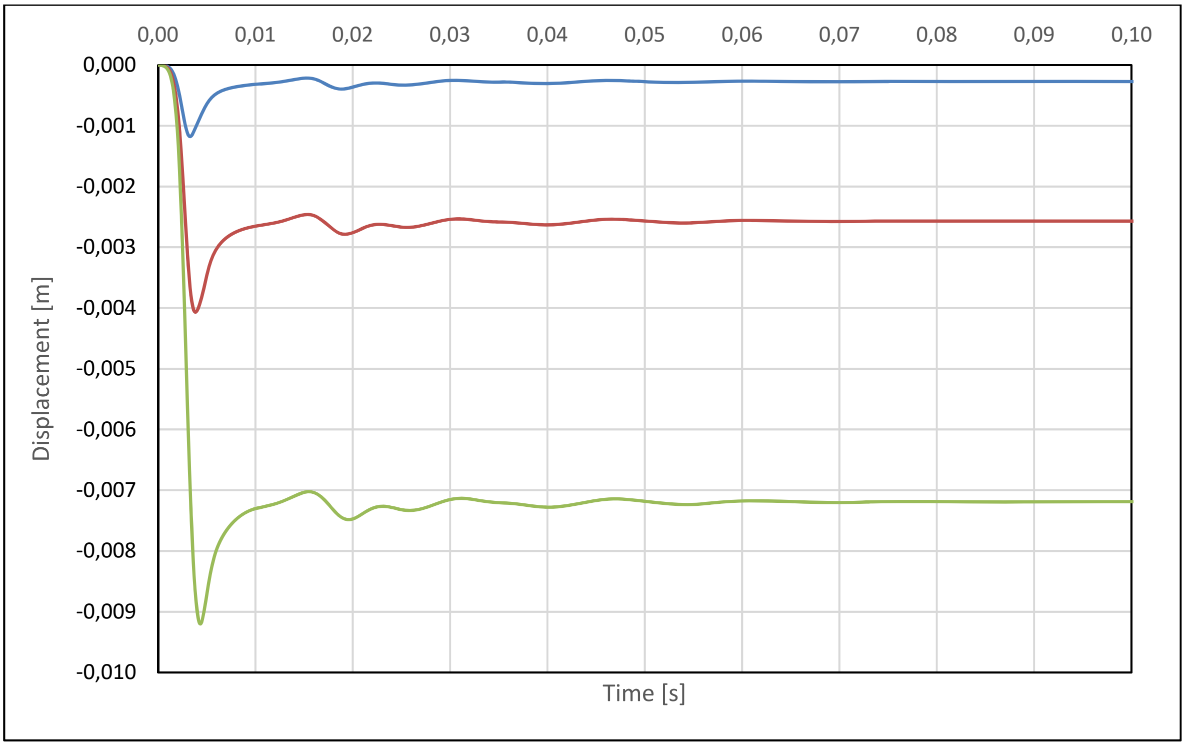

Figure 98. Dynamic time vs vertical displacements

The final permanent displacement is influenced by different variables:

- the undrained shear strength: a soil with a greater strength will have less plastic deformations and by consequence a lower permanent displacement;
- the elastic modulus: a stiffer soil will experience lower displacements for equal load, because of the bigger resistance to the plastic penetration flow;
- the material damping: since it acts as a dynamic resistance, the higher is the damping, the lower will be the displacement;
- flint diameter: for an equal force, the bigger is the diameter, the lower will be the displacement;
- impact load: the highest is the peak force and the longer is the impact duration, the bigger will be the displacement, because of the higher energy content.

7.4.2 Data processing

A parametric analysis is carried out in order to find a relation between the flint permanent displacement and the peak force. The dynamic load shape (see §7.2) is not varied in the analyses, but it is only scaled for different peak force values. The material damping is assumed equal to 5% for two target frequencies selected for different diameters (see §7.3.4). The other variables, such as the peak force F_{peak}, the chalk S_u, the chalk E_u and the flint diameter d are changed in order to obtain a database from which deriving a law.

In Appendix E 10.5, the obtained results are presented in 2 different tables, one for the centered force (0°) and one for the lateral force (at 45°). In each table there are reported the characteristics of the model and the peak force (vertical and horizontal) with the relative permanent displacement obtained. In order to find a law these data are subsequently processed in Excel.

The aim is to find an equation dimensionally correct which fits the data in the best way.

The variables involved are:

- F: peak force [kN];
- S_u: undrained shear strength chalk [kPa];
- E_u: undrained elastic modulus [kPa];
- d: flint diameter [m];
- L: flint length (plane strain, cylinder) [m];
- u: flint permanent displacement [m];

First of all, the force is normalized as follows:

$$Y = \frac{F}{\sqrt{S_u \ E_u} \ d \ L} \qquad 7.18$$

in this way, the parameter Y (normalized force) results adimensional.

Secondly, the permanent displacement (for blow) is normalized respect to the length of the flint considered, which is equal to 1 m because of the plane strain conditions:

$$X = \frac{u}{L} \qquad 7.19$$

Then, these two parameters are plotted (*Figure 99*), with *Y* on the y-axis and *X* on the x-axis (in a logarithmic scale for a better visualization of the data).

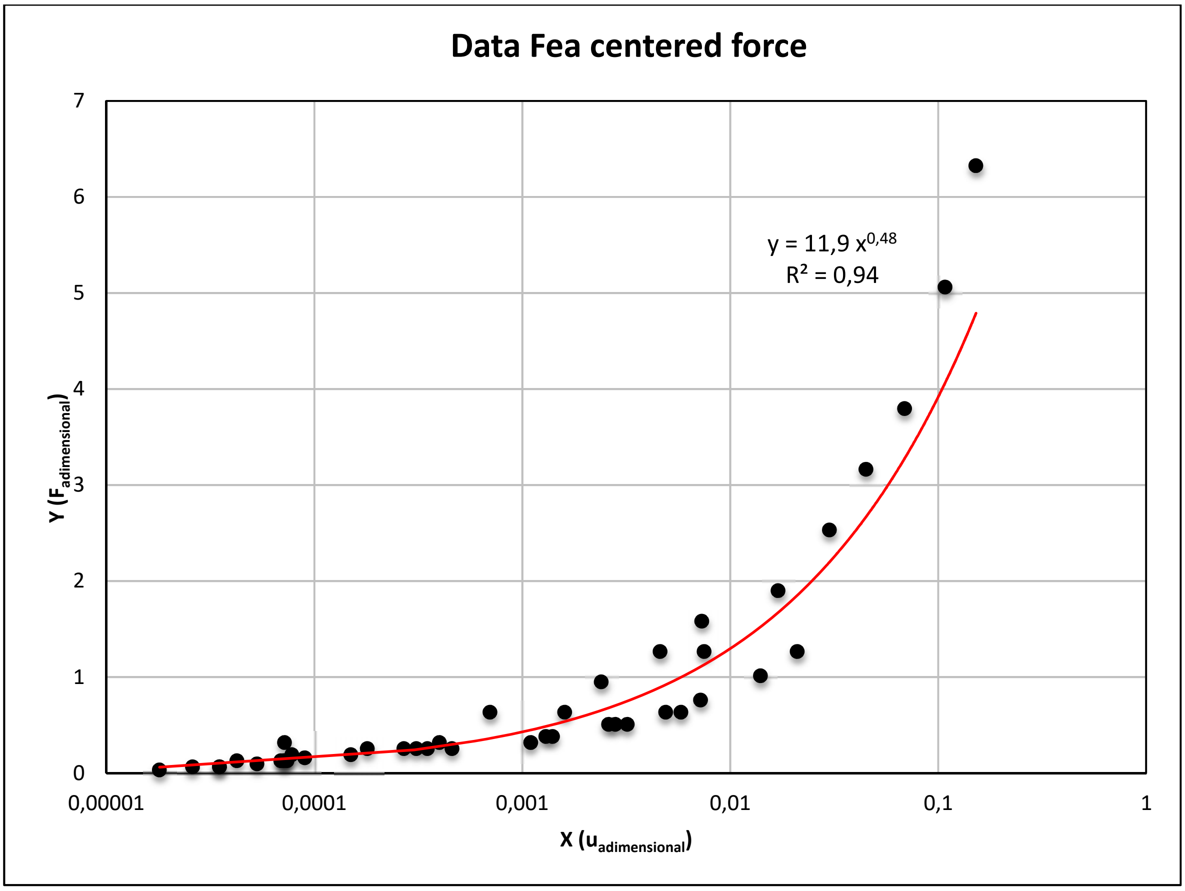

Figure 99. Finite element analysis results for centered force

By adding a power trend line, the results are fitted in a reasonable way and the resulting approximate equation is:

$$Y = 12\,(X)^{0.5} \rightarrow u = \left(\frac{F}{12\,\sqrt{S_u\,E_u}\,d\,L}\right)^2 L$$

$$\boxed{u = \frac{F^2}{144\,S_u\,E_u\,d^2\,L} \qquad 7.20}$$

It is could be useful to add a threshold to this equation. In fact, if the force does not reach a minimum value, the permanent displacement will be zero because no plasticization will occur.

Figure 100 focus only on small displacement values. It can be seen that for $Y < 0.3$ no analysis returns a displacement bigger than 1mm, and the trend of the data suggest the obtained displacement is an effect of the numerical analyses with no physical meaning. As well, by coincidence, the value of 1mm corresponds essentially to the refusal criteria proposed by API (2011), which indicate a general value of 1mm (250 blow for 25 cm). So, smaller displacements are also not meaningful from the engineering point of view as would represent an extremely and non-acceptable slow driving.

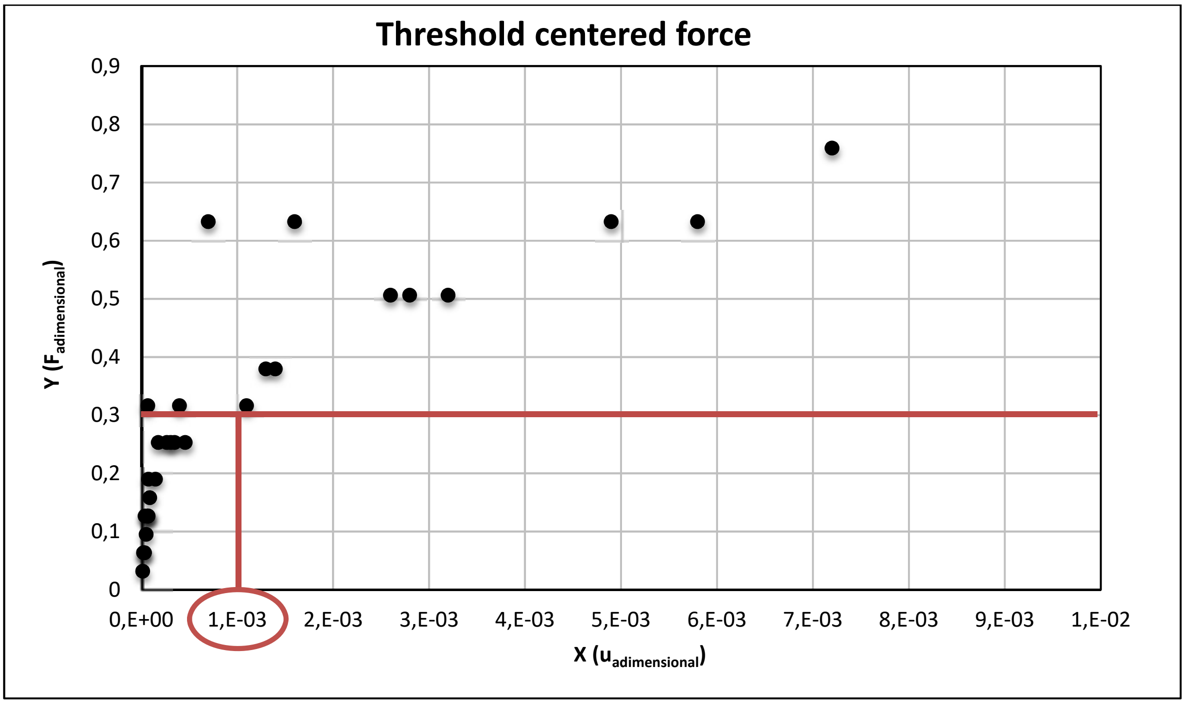

Figure 100. Threshold selection from FEA for centered force

At $Y = 0.3$ a threshold is set. Thus, before predicting a displacement with the formula, it is could be useful to check if the force satisfies this requirement:

$$F_y > 0.3\left(\sqrt{S_u\ E_u}\ d\ L\right) \qquad 7.21$$

The results could also be plotted in a linear scale. From *Figure 101* it can be seen clearly the threshold value of 0.3, which results also from the equation of a second order polynomial trendline (in green on the chart). This interpolation will not be used anyway because it results more complicated and it does not add a substantial precision on the predicted displacement values.

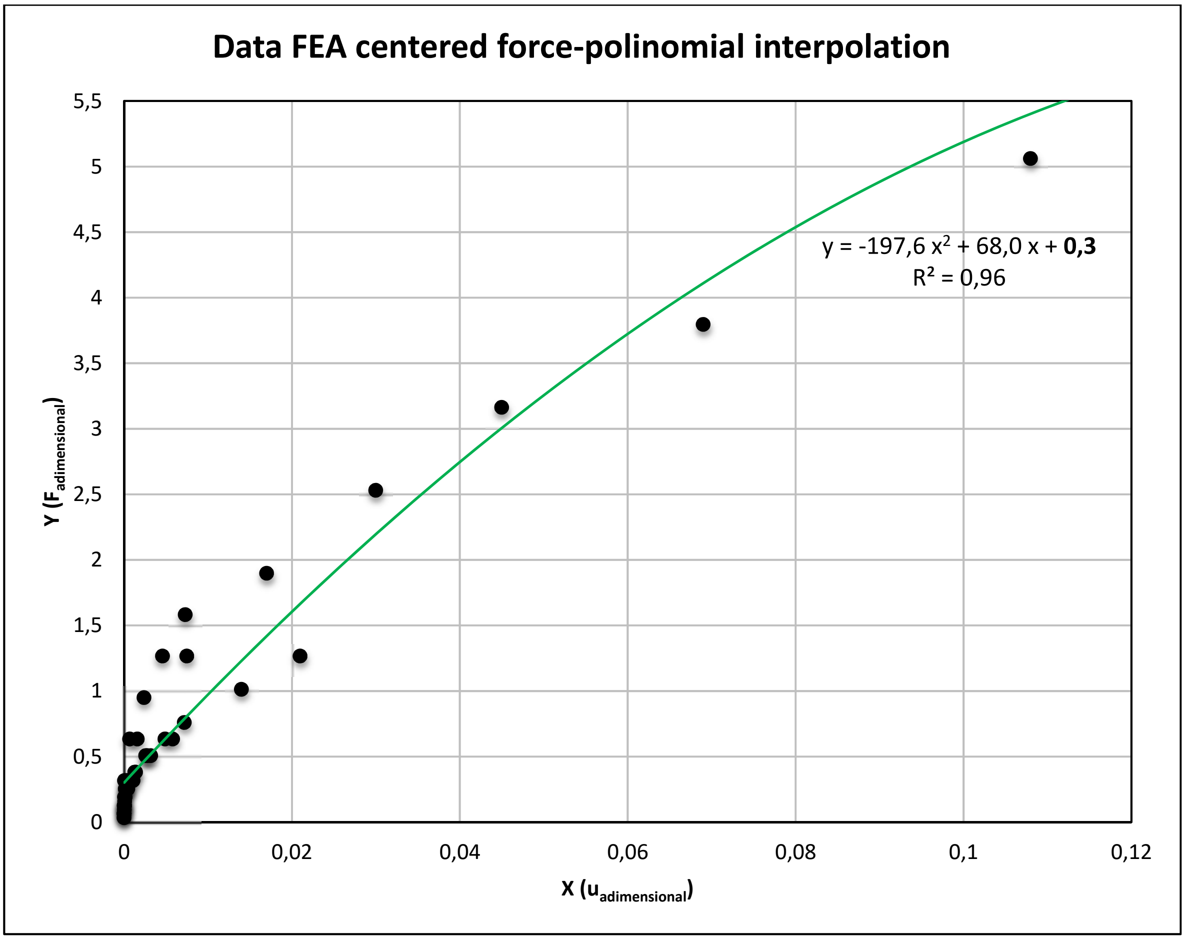

Figure 101. Polynomial interpolation of Dynamic results

This threshold value is in accordance with the static analysis (see Chapter 5). In fact, since in our analyses a S_u/E_u ratio of 1000 was assumed:

$$F_y > 0.3\left(\sqrt{S_u\ E_u}\ d\ L\right) > 0.3\left(\sqrt{S_u\ (1000 S_u)}\ d\ L\right) > \mathbf{9.6}\, S_u\, d\, L$$

The resulting value of **9.6** is similar to the N_c factor (see §5.2.3), which is equal to **11.9**, which confirmed that a peak force of the order of the static "capacity" of the flint/boulder is necessary to obtain an engineering significant displacement. The difference is justified by the fact that the value 11.9 is reached for a complete plasticization (flow mechanism).

If the selected threshold value is substituted inside the equation, the minimum displacement predicted will be about 0.6 mm, which could be assumed as a minimum reasonable result. The resulting law can be expressed as:

$$\begin{cases} if\ \ F_y > 0.3\left(\sqrt{S_u\ \ E_u}\ \ d\ \ L\right) \to u = \dfrac{F^2}{144\, S_u\, E_u\, d^2\, L} \\ if\ F_y > 0.3\left(\sqrt{S_u\ \ E_u}\ \ d\ \ L\right) \to u = 0 \end{cases}$$

It is interesting to plot this law by inverting it, in order to have a graph comparable to a bearing graph (an example it is shown in *Figure 102*).

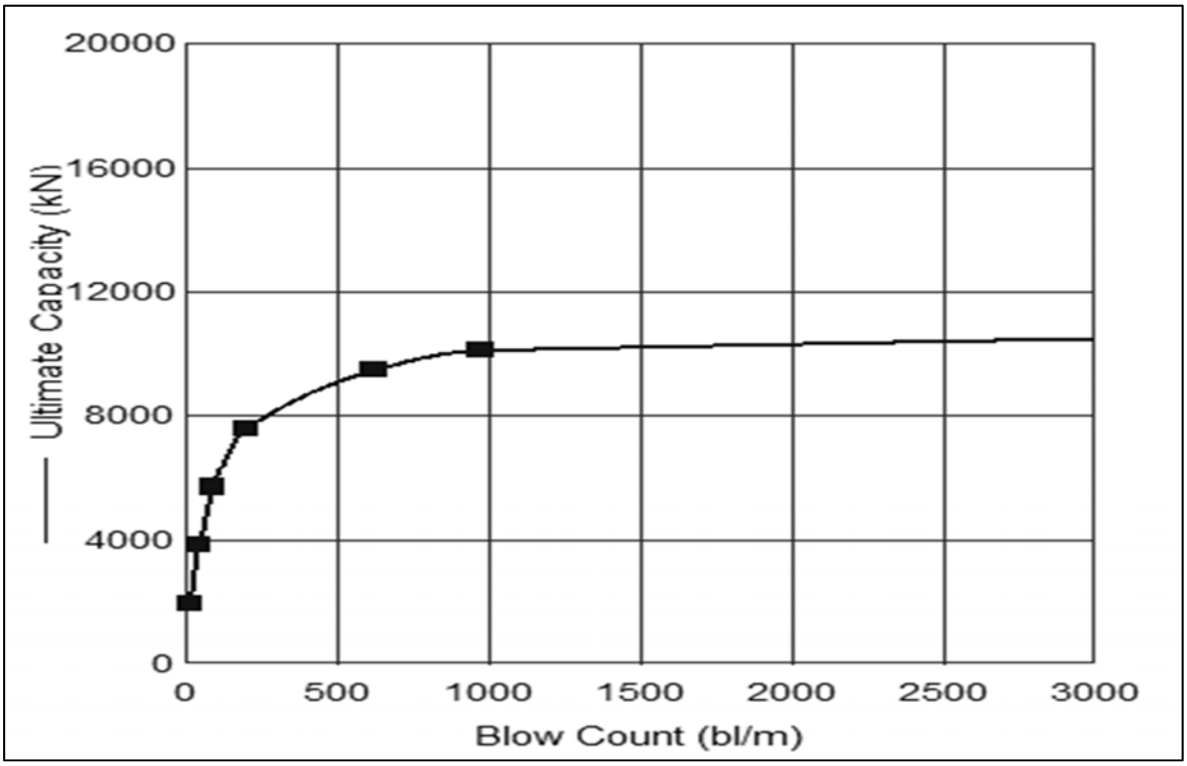

Figure 102. Example of a bearing graph from GRLWEAP

The bearing graph expresses the relationship between blow count and pile capacity. It is a common method used to assess the bearing capacity from an observed blow count or to calculate the blow count for a bearing capacity which must be achieved (Pile Dynamics, 2010). In a bearing graph, on the x-axis is plotted the blows/meter and on the y-axis the soil resistance to drive. So, it is simply necessary to plot the reciprocal of the normalized displacement (X parameter) and the reciprocal of the normalized force (Y parameter) to obtain a comparable graph. In fact, the force is normalized by dividing it for an equivalent resistance ($\sqrt{S_u\, E_u}\ \ d\ \ L$). For displacements lower than 0.6 mm, the relative force is imposed equal to the threshold value of 0.3. The resulting plot is:

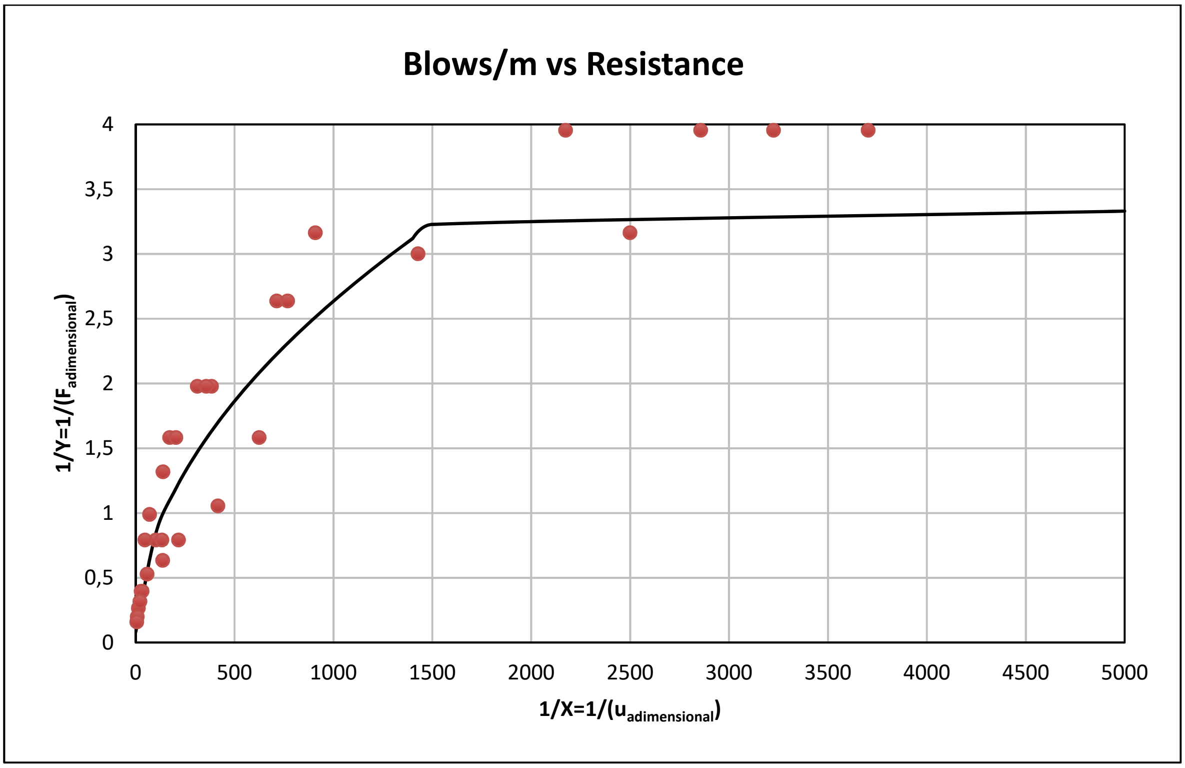

Figure 103. Blows count vs equivalent relative resistance

It can be seen that as the resistance increases (it is a relative resistance because it is related to a certain force, energy), a higher number of blows is needed to displace the boulder of 1m. When the resistance reaches the threshold value ($=\frac{1}{0.3}$), the line becomes horizontal. This means that for higher relative resistances the boulder will not displace. The explanation is that the resistance is too high compared to the energy transferred to the boulder, and by consequence the force cannot plasticize the adjacent soil and produce a permanent displacement.

In order to investigate the influence of the damping, for an average flint diameter of 0.5m the numerical analysis have been repeated without input material damping. The comparison of the results is reported in *Table 15* and graphically in *Figure 104*.

Table 15. Damped vs undamped analysis

u_no damping [m]	u_damping [m]	Ratio [%]	average [%]
0,00170	0,00160	94	**81**
0,00900	0,00750	83	
0,02200	0,01700	77	
0,04000	0,03000	75	
0,06500	0,04500	69	
0,00004	0,00004	97	
0,00036	0,00031	86	
0,00170	0,00130	76	
0,00380	0,00280	74	
0,00800	0,00490	61	
0,00004	0,00004	100	
0,00008	0,00007	93	
0,00017	0,00015	88	
0,00060	0,00046	77	
0,00170	0,00110	65	

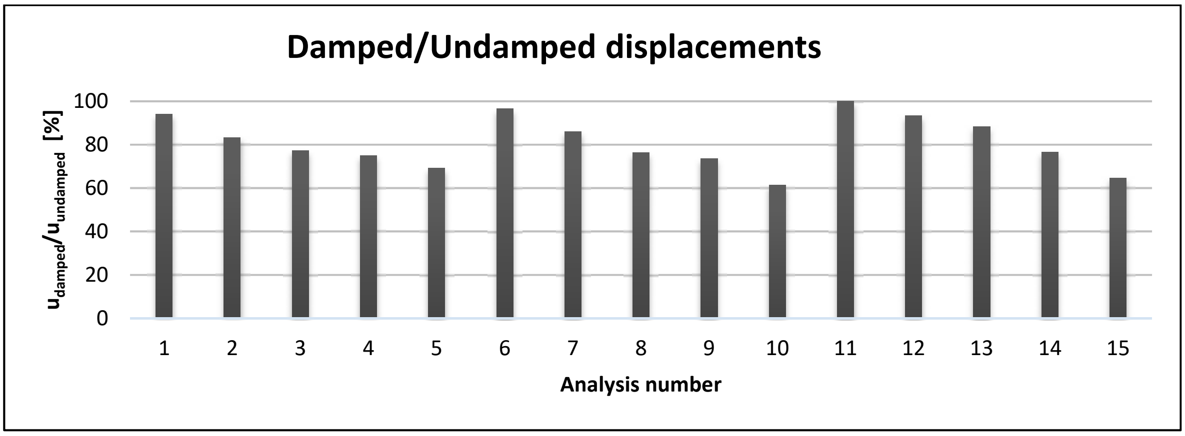

Figure 104. Damped vs undamped analysis

In the first 5 analyses (1-5), the soil properties are unchanged (Chalk 1) while the force is increased. The same for the analysis from 6 to 10 (Chalk 2) and from 11 to 15 (Chalk 3). It can be concluded that for small forces the difference between damped and undamped permanent displacements is lower than for high forces. This can be explained because small forces are associated with smaller oscillation velocities; since the damping is directly related to velocity, to lower velocities correspond a lower damping influence.

Moreover, the strength and stiffness properties of the material have a role in the damping influence. In fact, if the analysis 1 is compared with the analysis 15, it can be seen that for an equal undamped displacement (0.0017m) correspond two different damped displacements. The explanation could be that a stiffer material (analysis 15, Chalk 3) oscillates with a high velocity and by consequence its motion is more damped.

In conclusion, in the analyses performed, a 5% value of material damping produces an average difference of 80% on permanent displacements.

Lateral Contact between flint/boulder and pile (at 45°)

The same data processing is done for analysis related to the lateral contact. However, now the relationship is between the horizontal force and the permanent vertical displacement. The results of the finite element analysis are plotted in *Figure 105*.

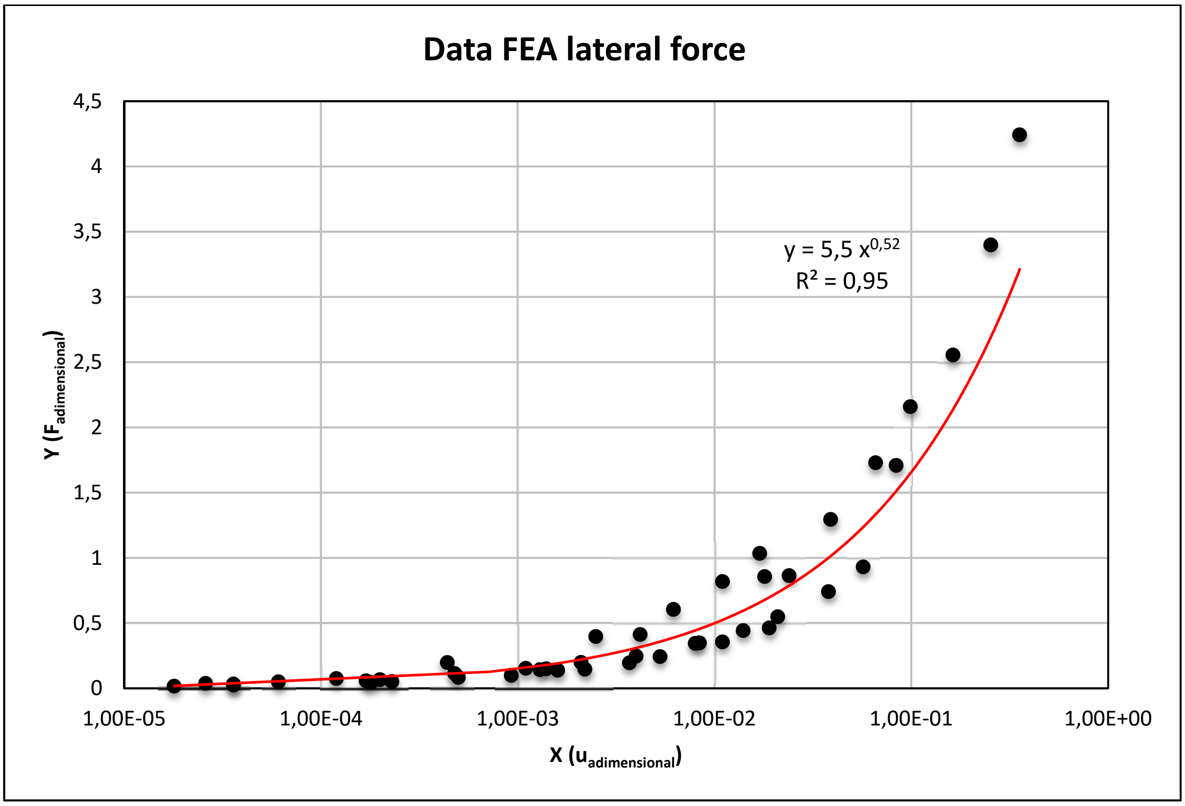

Figure 105. Finite element analysis results for lateral force

By adding a power trendline, the results are fitted in a reasonable way and the resulting approximate equation is:

$$Y = 5.5\,(X)^{0.5} \rightarrow u = \left(\frac{F_x}{5.5\sqrt{S_u\,E_u}\,d\,L}\right)^2 L$$

$$u = \frac{{F_x}^2}{30\,S_u\,E_u\,d^2\,L} \qquad 7.22$$

Figure 106 focuses only on small displacement values. It can be seen that for $Y < 0.13$ no analysis returns a displacement bigger than 1 mm.

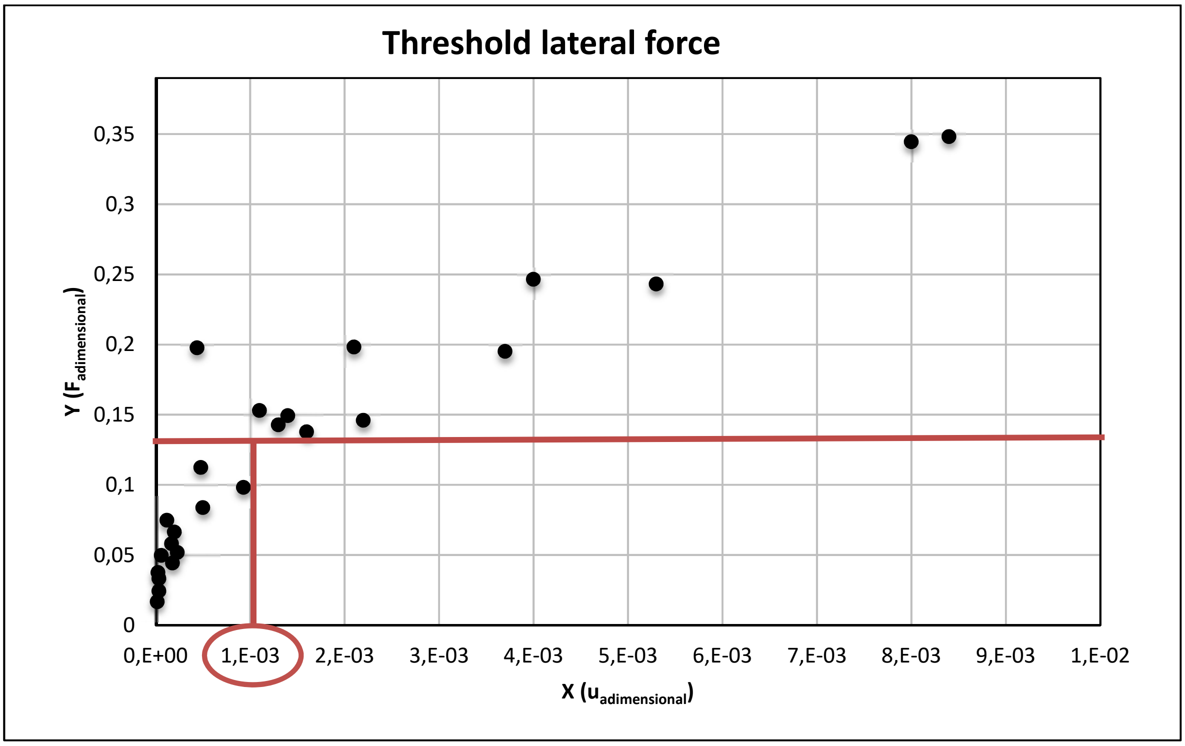

Figure 106. Threshold selection from FEA for lateral force

In conclusion, at 0.13 a threshold is set. Thus, before predicting a displacement with the equation, it is could be useful to check if the force satisfies this requirement:

$$F_x > 0.13\left(\sqrt{S_u\;E_u}\;d\;\;L\right) \qquad 7.23$$

The resulting law can be expressed as:

$$\begin{cases} if\ F_y > 0.13\left(\sqrt{S_u\ E_u}\ d\ L\right) \rightarrow u = \dfrac{F^2}{30\ S_u\ E_u\ d^2\ L} \\ if\ F_y > 0.13\left(\sqrt{S_u\ E_u}\ d\ L\right) \rightarrow u = 0 \end{cases}$$

Application examples of obtained equations

Table 16 reports some values obtained applying the found laws, for different flint geometries and chalk parameters.

Table 16. Example of displacements obtained from equation for different conditions

S_u [kPa]	d [m]	E_u [kPa]	L [m]	F_y [kN]	F_x [kN]	t [mm]	σ_y [Mpa]	u 0° [mm]	u 45° [mm]
100	0,5	100000	0,5	1568	784	40	350	**13,7**	**16,4**
500	0,5	500000	0,5	1568	784	40	350	**0,5**	**0,7**
500	0,3	500000	0,3	1568	784	40	350	**2,5**	**3,0**
300	0,2	300000	0,2	1568	784	40	350	**23,7**	**28,5**
800	0,4	800000	0,4	4802	2401	70	350	**3,9**	**4,7**
500	0,8	500000	0,8	4802	2401	70	350	**1,3**	**1,5**
1000	0,5	1000000	0,5	4802	2401	70	350	**1,3**	**1,5**

Table 17 reports some values derived from the threshold condition and the relative minimum pile thickness needed to prevent local buckling during driving according to Aldridge et al. (2005), for different flint geometries and chalk parameters.

Table 17. Example of minimum pile thickness obtained for different conditions

S_u [kPa]	E_u [kPa]	d [m]	L [m]	F_y threshold [kN]	F_x threshold [kN]	$t_{min\ y}$ [mm]	$t_{min\ x}$ [mm]
100	100000	0,5	0,5	237	103	**16**	**14**
500	500000	0,5	0,5	1186	514	**35**	**32**
500	500000	0,3	0,3	427	185	**21**	**19**
300	300000	0,2	0,2	114	49	**11**	**10**
800	800000	0,4	0,4	1214	526	**35**	**33**
500	500000	0,8	0,8	3036	1316	**56**	**52**
1000	1000000	0,5	0,5	2372	1028	**49**	**46**

7.4.3 Driveability assessment

At this point, two relationships (one for the vertical and one for the horizontal force) are found. In this sub-chapter is presented a possible method to apply them in a driveability study and it is specified in which situations they may be used.

First of all, the main concept is that for a big diameter pile (i.e. 4-7m) hitting a flint (average diameter of 30-50 cm) is not a "global" problem but a "local" one. This means that the advancement of the pile is not compromised by the interaction with the flint because, at the pile's scale, flint results too small to influence pile's displacements.

In fact, since the shaft resistance in non-displacement piles could be about 97% of the total, an increase in the toe resistance of for example 50% [5] has not a significant influence on the global behavior of the pile (it is possible to think at the flint as an increase in the end bearing capacity). So, in a driveability analysis it could be legitimate to neglect the presence of the flint: the resulting blows/meter should be very similar.

On the contrary, flint generates a point force which could trigger the local buckling of the pile wall. This reaction force depends on the advancement that the pile imposes to the flint during the driving process (i.e. the bigger will be the advancement for blow, the bigger will be the local reaction that the flint will generate).

The aim is to understand the maximum advancement per blow allowed, in order to prevent the local buckling by reducing the hammer energy.

After the FEA a relationship between the peak force (horizontal and vertical) and the permanent displacements of the flint has been found.

$$u_{perm} = f(F, E_{u,chalk}, S_{u,chalk}, d_{flint})$$

Therefore, given the $E_{u,chalk}$, $S_{u,chalk}$, d_{flint} and F_{peak}, this equation returns a permanent displacement of the flint.

---

[5] *Pile diameter=7m, pile thickness=77mm, S_u=100kPa →Toe resistance=9 S_u A_b=**1507kN***
*Spherical flint diameter=0.8m → F=15 π r^2 Su=**754kN** (ball penetrometer or 3D FEA)*
*→The total resistance increase=**1%** → **negligible***

Concerning the F_{peak}, Aldridge et al. (2005) provided a simple formula to find the force (vertical and horizontal) which damages a pile of a certain thickness and yield stress.

$$F_y = 2.8\ \sigma_y\ t^2$$
$$F_x = 1.4\ \sigma_y\ t^2$$

With that peak forces it is possible to find the displacement of the flint thanks to the previous relationships (see §7.4.2). By consequence, the maximum displacements per blow to prevent the pile damage can be found.

The energy of the hammer should be calibrated in order to not overpass this blow set. This calibration could be done with a trial and error procedure on GRLWEAP in which the hammer parameters are changed (i.e. stroke) in order to increase the blows/meter in the layer where flints are expected.

This procedure is summarized below:

1. from pile geometry and strength (σ_y, t), the limit force to prevent local buckling is obtained as indicated by Aldridge et al. (2005).

$$F_y = 2.8\ \sigma_y\ t^2 = F_{y,peak}$$
$$F_x = 1.4\ \sigma_y\ t^2 = F_{x,peak}$$

2. with this force, the flint geometry (d, L) and chalk properties (Su, Eu), the flint permanent displacement for one blow and for two different contact points is determined:

$$u_{perm,0°} = \frac{{F_{y,peak}}^2}{144\ S_u\ E_u\ d^2\ L}$$

$$u_{perm,45°} = \frac{{F_{x,peak}}^2}{30\ S_u\ E_u\ d^2\ L}$$

3. from the flint displacement, i.e. the pile base displacement, the lower limit value for blows rate (blows/m), i.e. the upper bound advancement per blow is found:

$$lower\ bound\ blows\ rate = \left(\frac{blows}{m}\right)_{min} = min\left(\frac{1}{u_{perm,0°}}, \frac{1}{u_{perm,45°}}\right)$$

4. from the lower bound blows rate (blows/meter), a limitation to hammer energy per blow is finally obtained (e.g. GRLWEAP calibration) as safe value for the pile tip buckling risk.

$$\frac{blows}{m} = f(hammer\ stroke) \geq \left(\frac{blows}{m}\right)_{min}$$

It is important to underline that this method should only be used for piles of big diameter because otherwise the assumptions initially done could not be accepted. In fact, for small diameter piles the increase in the toe resistance could be important and it could influence significantly the global behavior of the pile. For example:

Pile diameter=1m
pile thickness=18mm →Toe resistance=50kN
S_u=100kPa

Spherical flint diameter = 0.8m → $F_{lim} = 15\ \pi\ r^2\ S_u = 754kN$ (ball penetrometer)

→Total resistance increase=8% (could not be negligible).

In conclusion, it should be verified how much the flint presence influence the total resistance. Since the idea is that the flint is a portion of the pile diameter, the formula should be valid for a wide range of piles sizes.

8. Conclusions and future developments

8.1 Conclusions

An accurate study of the problematics which could occur during pile driving of large diameter piles in chalk has been carried out, with particular relevance of the cases when the pile advancement is obstructed by a boulder (flint). After a preliminary static analysis on flint behaviour, a special focus has been put on the dynamic displacement of a flint embedded in a softer formation, when it is hit by the wall of an open ended, steel pile. More in detail, several finite element analyses with PLAXIS were developed to simulate the static and dynamic interaction between a flint and a driven pile.

Concerning the static analyses, the failure behavior of a circular flint subjected to a force with different inclination has been explored by numerical analyses, presenting the results in a failure envelope. From that envelope it is possible to obtain easily the normal and tangential force needed for failure, depending on the incident angle. However, since the condition imposed by the pile is more like a pure vertical displacement on a flint, the vertical and horizontal forces arising from applied displacements are provided, for different contact points. It has been proved that the maximum vertical force arises if the pile hits the flint perfectly in the center, while the maximum horizontal force arises when the pile hits the flint at about 45-50° (angle in the center). Finally, the 3D analyses have revealed a similar trend of the arising forces.

Concerning the dynamic analyses, a relationship between the peak force and the related permanent flint displacement has been provided. Thus, given the dimension of the flint, the strength and stiffness of the chalk and the buckling force of the pile, it is possible to obtain the maximum displacement per blow to prevent tip damage. In fact, if this displacement is exceeded bigger reaction could arise and, since the pile cannot support that, it could buckle. In conclusion, the found law could be used in a driveability analysis in order to calibrate the maximum allowable stroke of the hammer to avoid potential pile damage. The applicability of this procedure could however be limited to big diameter piles or anyway to the cases in which the flint interaction is not a global problem (since the relative small dimension of the flint) but a local one.

Summarizing, the main elements investigated in the work herein presented were:

- a study of flint and chalk geology, with a special focus on the engineering properties;
- a study of pile-boulder interaction;
- a preliminary study on flint brittleness and breakage;
- a series of static 2D numeric analyses with a FE code (PLAXIS) to investigate the mechanical behavior of a flint embedded in a chalk subjected to a static force or displacement; the results are presented in several failure envelopes.
- a series of static 3D numeric analyses in order to analyze the tridimensional behaviour of the flint and to provide failure forces; a comparison with the 2D results is presented.
- a series of dynamic 2D numeric analyses in order to investigate the dynamic behavior of a flint subjected to an impact load; a relation between the peak force and the flint permanent displacement is provided for both centered and lateral point contact.
- a practical application of the resulting relation is proposed as a driveability assessment procedure.

Conclusions can be drawn in terms of an optimal range of hammer operational setting (maximum advancement per blow), depending on expected boulder size and chalk properties, to not damage the pile tip during the advancement.

8.2 Future developments

Since no similar studies have already been performed, starting from this work more improvements should be made in the future. In fact, the results that were obtained suggest that the developed numerical models are a promising tool to conduct more elaborate analyses. Future studies are now suggested:

- to deeply investigate flint breakage under an impact load, laboratory test (Dynamic load test on flints) could be carried out to define different type of curves S-N (cyclic stress-number of cycles to failure of flint subjected to tensile loads);
- a parametric analysis on the damping coefficient could be done to investigate its influence and to include it inside the final law; moreover, different material model could be used to model the hysteretical damping and the stiffness decay within the chalk (e.g. the hardening soil model with small-strain stiffness in PLAXIS).
- the same parametric dynamic analysis presented in Chapter 8 could be done in a 3D model, in order to explore different flint geometries and failure mechanisms. Eventually, it could be interesting to model also the pile or to investigate different shapes of the input load.

These suggested in-depths researches could led to a modification of the standard driveability analysis in presence of potential obstructions, which would be a huge development for the geotechnical offshore community.

9. References

Akhavan, A., 2013. *Flint and Chert.* [Online] Available at: http://www.quartzpage.de/flint.html [Accessed 15 Novembre 2017].

Aldridge, T., Carrington, T. & Kee, N., 2005. Propagation of pile tip damage during installation. In: *Proc. Int. Conf. Frontiers in Offshore Geotechnics.* Australia: Taylor and Francis, p. 827.

Amorosi, A., Boldini, D. & Elia, G., 2010. Parametric study on seismic ground response by finite element modelling. *Computers and Geotechnics,* 37(4), pp. 515-528.

API, 2014. *Recommended practice for planning, designing and constructing fixed offshore platforms.*

API, R. 2., 2011. *Geotechnical and foundation design considerations.* Washington: American Petroleum Institute.

Attewell, P. & Farmer, 1973. Attenuation of Ground Vibrations from Pile Driving. In: *Ground Engineering*, pp. 26- 29.

Biot, M. A., 1956. Theory of Propagation of Elastic Waves in a Fluid-Saturated Porous Solid. *The Journal of the Acoustical Society of America,* 28(2).

Boggs, S., 2009. *Petrology of Sedimentary Rocks.* Cambridge: Cambridge University Press.

Britannica, 2013. *Encyclopædia Britannica.* [Online] Available at: https://www.britannica.com/science/chalk [Accessed 8 Novembre 2017].

Broos, E., Sibbes, R. & Gijt, J. D., 2017. *Widening a harbor basin, demolition of a deep see quay wall in Rotterdam.* Hamburg, COME.

Burland, J. B. & Lord, J. A., 1970. The Load-deformation Behaviour of Middle Chalk at Mundford, Norfolk. *Proc Conf In Situ Investigations In Soil And Rocks, Brit Geotech Society,* pp. 3-15.

Cerfontaine, B. & Collin, F., 2017. Cyclic and Fatigue Behaviour of Rock Materials: Review, Interpretation and Research Perspectives. *Rock Mech Rock Eng.*

Clayton, C., 1986. The chemical environment of flint formation in Upper Cretaceous Chalk. In: *The scientific study of flint and chert.* Cambridge: Cambridge University Press, pp. 43-54.

Clayton, C. R. I. & Saffari-Shooshtari, N., 1990. 16 Constant normal stiffness direct shear testing of chalk/concrete interfaces. *Chalk: International symposium,* pp. 233-238.

Clough, R. & Penzien, J., 1993. *Dynamics of structures.* New York: McGraw Hill.

Cumming, F., 1999. *Machine tunneling in chalk with flint with particular reference to the mechanical properties of flint.* Doctoral thesis: University of Brighton.

Deeks, J. & Randolph, M. F., 1993. Analytical modelling of hammer impact for pile driving. *International journal for numerical and analytical methods in geomechanics,* Volume 17, pp. 279-302.

Durelli, A. & Parks, V., 1967. Influence of size and shape on the tensile strength of brittle materials. *British Journal of Applied Physics,* 18(3).

Fleming, W., Weltman, A. & Randolph, M., 1992. *Pile Engineering.* 2nd ed. London: Blackie Academic.

Frye, K., 1983. *The Encyclopedia of Mineralogy*: Springer US.

Goble, G. & Rausche, F., 1986. Wave Equation Analysis of Pile Foundations. In: *WEAP86 Program.* Washington, DC.: Federal Highway Administration .

Goble & Rausche, 1999. *Wave Equation Manual.* Cleveland, Ohio.

Hancock, J. M., 1975. The petrology of the Chalk. *Proceedings of the Geologists' Association,* 86(4), pp. 449-535.

Hilber, H. M., Hughes, T. J. R. & Taylor, R. L., 1977. Improved numerical dissipation for time integration algorithms in structural dynamics. *Earthquake Engineering & Structural Dynamics,* Volume 5, pp. 283-292.

Holeyman, A., Peralta, P. & Charue, N., 2015. Boulder-soil-pile dynamic interaction. In: *Frontiers in Offshore Geotechnics III – Meyer.* London: Taylor & Francis Group.

HSE, 2001. *A Study of Pile Fatigue During Driving and In-Service and of Pile Tip Integrity.*

Hussein, M., Bixler, M. & Rausche, F., 2003. Pile Driving Resistance and Load Bearing Capacity. In: *Proceedings of the 12th PanAmerican Conference on Soil Mechanics and Geotech Engineering.* MIT, pp. 1817-1824.

Hussein, M. H., Woerner, W. A., Sharp, M. & Hwang, C., 2006. Pile Driveability and Bearing Capacity in High-Rebound Soils. *GeoCongress* .

ISRM, 1981. *Rock Characterisation, Testing and Monitoring.* Pergamon Press: E.T. Brown.

Jamiolkowski, M., 1979. Design parameters for soft clays. *Proceeding of the 7th European Conference on Soil Mechanics,* pp. 21-57.

Jauregui, R. & Silva, F., 2011. Numerical Validation Methods. In: *Numerical Analysis - Theory and Application.* Jan Awrejcewicz.

Knauth, L., 1994. Petrogenesis of chert. In: *Silica: physical behavior, geochemistry, and materials application.* Mineralogical Society of America, pp. 233-258.

Knauth, L. P., 1979. A model for the origin of chert in limestone. *Geology,* 7(6), pp. 274-277.

Kramer, S. L., 1996. *Geotechnical earthquake engineering.* Upper Saddle River, N.J: Prentice Hall.

Kuhlemeyer, R. L. & Lysmer, J., 1973. Finite Element Method Accuracy for Wave Propagation Problems. *Journal of the Soil Mechanics and Foundations Division,* 99(5), pp. 421-424.

Laera, A. & Brinkgreve, R., 2015. *Ground response analysis in Plaxis 2D.* Delft: PLAXIS.

Lake, L., 1975. *Engineering Properties of Chalk with Special Reference to Foundation Design and Performance,* University of Surrey: Doctoral thesis.

Lancellotta, R., 2012. *Geotecnica.* 4 ed. Zanichelli.

Lautridou, J. P. et al., 1986. Porosity and frost susceptibility of flints and chalk: laboratory experiments, comparison of glacial and periglacial surface texture of flint materials, and field investigations. In: *The scientific study of flint.* Cambridge: Cambridge University Press, pp. 269-282.

Lawrence, J. A., Collier, R., Aliyu, M. M. & Murphy, W., 2017. Engineering geological characterization of flints. *Quarterly Journal of Engineering Geology and Hydrogeology,* Volume 50, pp. 133-147.

Lindgreen, H. & Jakobsen, F., 2012. Marine sedimentation of nano-quartz forming flint in North Sea Danian chalk. *Marine and Petroleum Geology,* 38(1), pp. 73-82.

Liu, M. & Gorman, D., 1995. Formulation of Rayleigh damping and its extension. *Computers & Structures,* 57(2), pp. 277-285.

Lord, J., Clayton, C. & Mortimore, R., 2002. *Engineering in chalk.* London: CIRIA.

Lysmer, J. & Kuhlemeyer, R. L., 1969. Finite Dynamic Model for Infinite Media. *Journal of Engineering Mechanics Division,* Volume 95, pp. 859-878.

Masoumi, H. & Degrande, G., 2008. Numerical modeling of free field vibrations due to pile driving using a dynamic soil-structure interaction formulation. *Journal of Computational and Applied Mathematics.*

Massarsch, K. & Fellenius, B., 2008. *Prediction of ground vibrations induced by impact pile driving.* The Sixth International Conference on Case Histories in Geotechnical Engineering.

Masson, H. J., 1973. Petrophysique de la Craie. *Bulletin de Liaison des Laboratoires des Ponts et Chaussées,* Volume Oct, pp. 23-48.

Matthews, M. & Clayton, C., 1993. Influence of intact porosity on the engineering properties of a weak rock. *Geothecnical Engineering of Hard Soils-Soft Rocks. International Symposium,* pp. 693-702.

Monroe, J., Wicander, R. & Hazlett, R., 2006. *Physical Geology: Exploring the Earth.* 6 ed. Belmont: Thomson.

Moore, C., 1989. Carbonate diagenesis and Porosity. *Elsevier Science Publications.*

Mortimore, R., 2010. A chalk revolution: what have we done to the Chalk of England. *Proceedings of the Geologists' Association.*

Mortimore, R. N., Duperret, A. & Lawrence, J., 2004. Chalk physical properties and cliff instability. *Geological Society London Engineering Geology Special Publications.*

Mortimore, R. & Wood, C., 1986. The distribution of Flint in the English Chalk. *Conference paper.*

Mortimore, R. & Wood, C., 1986. The distribution of Flint in the English Chalk. In: *The scientific study of flint and chert.* Cambridge: Cambridge University Press, pp. 7-20.

Mortimore, R., Wood, C. & Gallois, R., 2001. British Upper Cretaceous Stratigraphy. *Geological Conservation Review Series,* Volume 23, p. 558.

Muir, W. D., 2004. *Geotechnical modelling.* London: Spon Press.

Nejati, H. R. & Ghazvinian, A., 2013. Brittleness Effect on Rock Fatigue Damage Evolution. *Rock Mech Rock Eng.*

Newmark, N., 1959. *ASCE Journal of Engineering Mechanics Division,* 85(3).

Nichols, G., 2009. *Sedimentology and Stratigraphy.* 2 ed. Chichester: Wiley-Blackwell.

Nicolini, E. & Castelletti, M., 2017. Numerical analysis to determine the failure envelope of a cross-shape plate foundation. *OSIG.*

Pile Dynamics, I., 2010. *GRLWEAP Help.*

PLAXIS, 2014. *Plaxis 2D Manual.* Anniversary Edition ed.

Randolph, M., 2016. An analitycal solution for th undrained horizontal-torsional resistance of mudmats. *Geotechnique.*

Randolph, M., 2016. *Design Issues for Steel Pipe Piles for Coastal Structures and Offshore Wind Turbines.* The HKIE Geotechnical Division Annual Seminar.

Randolph, M., 2016. *Design Issues for Steel Pipe Piles for Coastal Structures and Offshore Wind Turbines.* The HKIE Geotechnical Division Annual Seminar: s.n.

Randolph, M. F., 1991. Analysis of the dynamics of pile driving. In: P. K. Banerjee & R. Buttefield, eds. *evelopments in Soil Mechanics I V: Advanced Geotechnical Analyses.* s.l.: Elsevier Applied Science.

Randolph, M. F. & Andersen, K. H., 2006. Numerical Analysis of T-Bar Penetration in Soft Clay. *International Journal of Geomechanics,* 6(6), pp. 411-420.

Randolph, M. & Gourvenec, S., 2011. *Offshore Geotechnical Engineering.* Australia: Spon Press.

Randolph, M. & Houlsby, G., 1984. The limiting pressure on a circular pile loaded laterally in cohesive soil. *Géotechnique ,* 34(4), pp. 613-623.

Randolph, M., Martin, C. & Hu, Y., 2000. Limiting resistance of a spherical penetrometer in cohesive material. *Geotechnique,* 50(5), p. 573.

Randolph & Stewart, 1994. T-bar penetration testing in soft clay. *Journal of Geotechnical Engineering.*

Randolph & Zhou, 2011. Effect of shaft on resistance of a ball penetrometer. *Geotechique.*

Rausche, F., 2000. Pile Driving Equipment - Capabilities and Properties. In: *Proceedings of the 6th International Conference on the Application of Stress-Wave Theory to Piles.* São Paulo: Balkema, pp. 75-89.

Roark, R. & Young, W. .., 1975. *Formulas for stress and strain.* London: McGraw-Hill Book Company.

Roussel, H., 1979. *Pile driving analysis of large diameter high capacity offshore pipe piles.* Doctoral thesis: Tulane University New Orleans.

Saffari-Shooshtari, N., 1989. *COnstant normal stiffness direct shear testing of chalk-concrete interfaces.* Doctoral thesis: University of Surrey.

Schijve, J., 2003. Fatigue of structures and materials. *Fatigue Struct Mater,* Volume 25, pp. 679-702.

Serdaroglu, M. S., 2010. *Nonlinear analysis of pile driving and ground vibrations in saturated cohesive soils using the finite element method.* Doctoral thesis: University of Iowa.

Skempton, A., 1954. The pore-pressure coefficients A and B. *Geotechnique,* pp. 143-147.

Smith, E., 1960. Pile-Driving Analysis by the Wave Equation. *Journal of the Engineering Mechanics Division, Proceedings of the American Society of Civil Engineers,* 86(4).

Smith, N. A., Hislam, J. L. & Fowell, R. J., 2003. A Note On the Strength of Flint Particles. *Technology roadmap for rock mechanics,* pp. 1105-1108.

Strandgaard, T. & Vandenbulcke, L., 2002. *Driving monopoles into glacial till.* IBC's Wind Power Europe.

Stuyts, B. et al., 2017. *A methodology for the probabilistic assessment of pile refusal due to boulder encounter.* OSIG.

Vesic, A. S., 1975. Bearing capacity of shallow foundations. In: H. F. Winterkorn & H. Y. Fang, eds. *Foundation Engineering Handbook.* New York: Van Nostrand Reinhold Company.

Walter, S., 1972. *Flint: its origin, properties and uses.* London: Faber.

Zhao, J., 2000. Applicability of Mohr–Coulomb and Hoek–Brown strength criteria to the dynamic strength of brittle rock. *Int J Rock Mech Min Sci,* 37(7), p. 1115–1121.

10. Appendices

10.1 Appendix A

- Resulting initial stiffness for numerical analysis

d	E [kPa]	F [kN]	x [m]	k
0,2	100000	114,3	8,77E-04	130360,4
0,4	100000	234,5	1,41E-03	166194,2
0,8	100000	401	1,69E-03	236857,6
0,2	500000	107,4	1,64E-04	654878
0,4	500000	219	2,61E-04	839080,5
0,8	500000	159	3,98E-04	1154717
0,2	1000000	107	8,13E-05	1313653
0,4	1000000	218	1,30E-04	1680802
0,8	1000000	485	2,13E-04	2281279

10.2 Appendix B

- Input dynamic load multiplier

Time [seconds]	Dynamic multiplier
0	0
0,0000605	0,00205863
0,000121	0,00411726
0,0001815	0,006576178
0,000242	0,009035097
0,0003025	0,010645403
0,000363	0,012255709
0,0004235	0,014973101
0,000484	0,017690492
0,0005445	0,022035344
0,000605	0,026380197
0,0006655	0,033019278
0,000726	0,039658359
0,0007865	0,049396821
0,000847	0,059135284
0,0009075	0,072889218
0,000968	0,086643153
0,0010285	0,105373252
0,001089	0,124103352
0,0011495	0,148709697
0,00121	0,173316041

0,0012705	0,204491701
0,001331	0,235667362
0,0013915	0,273711984
0,001452	0,311756606
0,0015125	0,356379694
0,001573	0,401002781
0,0016335	0,451129273
0,001694	0,501255764
0,0017545	0,554892219
0,001815	0,608528674
0,0018755	0,662727822
0,001936	0,716926969
0,0019965	0,767902073
0,002057	0,818877178
0,0021175	0,862295967
0,002178	0,905714756
0,0022385	0,937179769
0,002299	0,968644781
0,0023595	0,984322391
0,00242	1,0
0,0024805	0,997328356
0,002541	0,994656712
0,0026015	0,973004502
0,002662	0,951352291
0,0027225	0,912508235
0,002783	0,873664178
0,0028435	0,822466055
0,002904	0,771267933
0,0029645	0,71348677
0,003025	0,655705607
0,0030855	0,596580616
0,003146	0,537455625
0,0032065	0,484250339
0,003267	0,431045052
0,0033275	0,389118769
0,003388	0,347192486
0,0034485	0,318608412
0,003509	0,290024338
0,0035695	0,2730029
0,00363	0,255981463
0,0036905	0,246173236
0,003751	0,236365009
0,0038115	0,22892535
0,003872	0,22148569
0,0039325	0,21273537

0,003993	0,20398505
0,0040535	0,191958077
0,004114	0,179931105
0,0041745	0,163925258
0,004235	0,147919412
0,0042955	0,127751702
0,004356	0,107583992
0,0044165	0,083058849
0,004477	0,058533707
0,0045375	0,043562893
0,004598	0,02859208
0,0046585	0,021158139
0,004719	0,013724199
0,0047795	0,010293149
0,00484	0,006862099
0,0049005	0,005146574
0,004961	0,00343105
0,0050215	0

10.3 Appendix C

- Influence of interface thickness

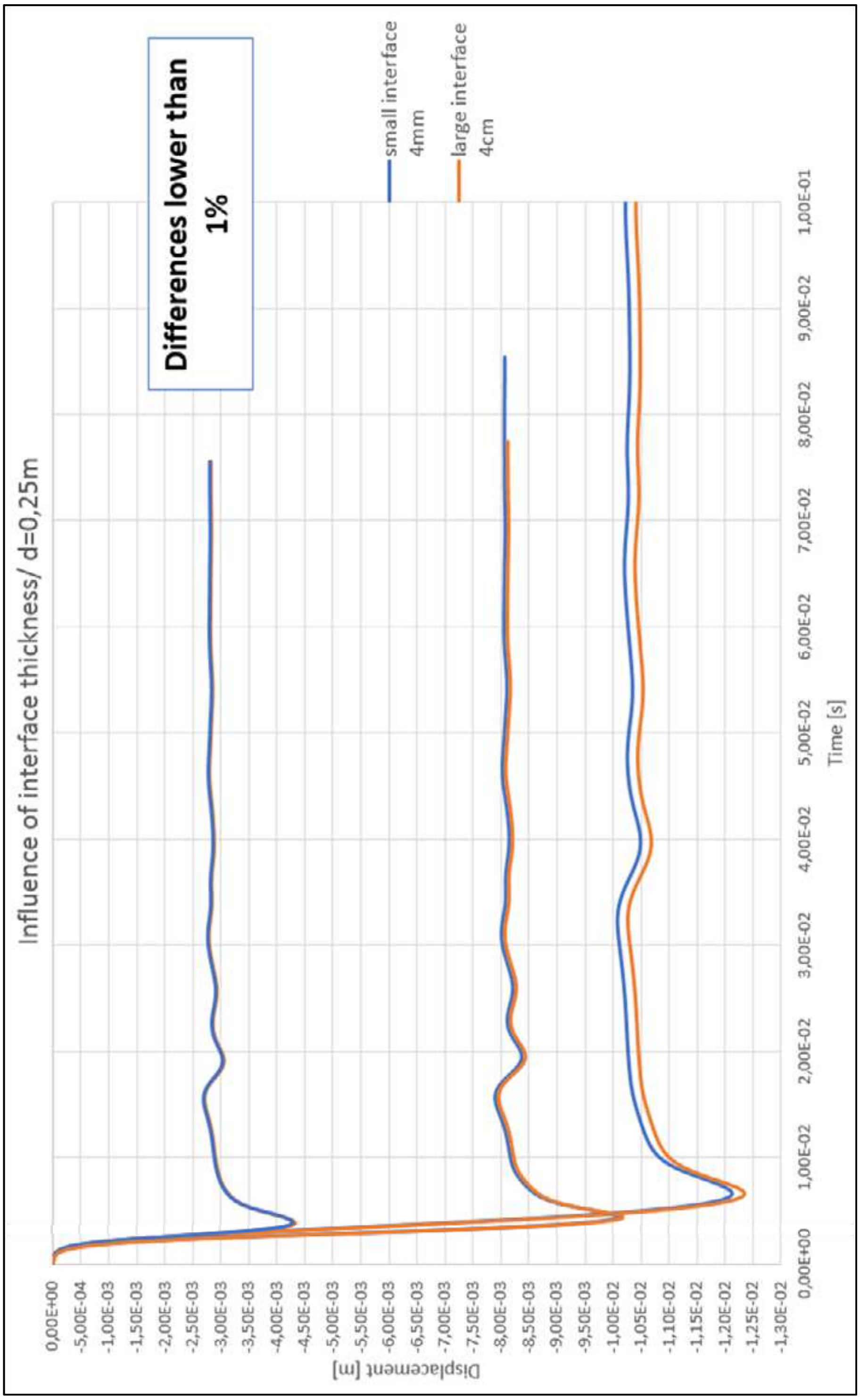

10.4 Appendix D

- Time-velocity curves of undamped analyses

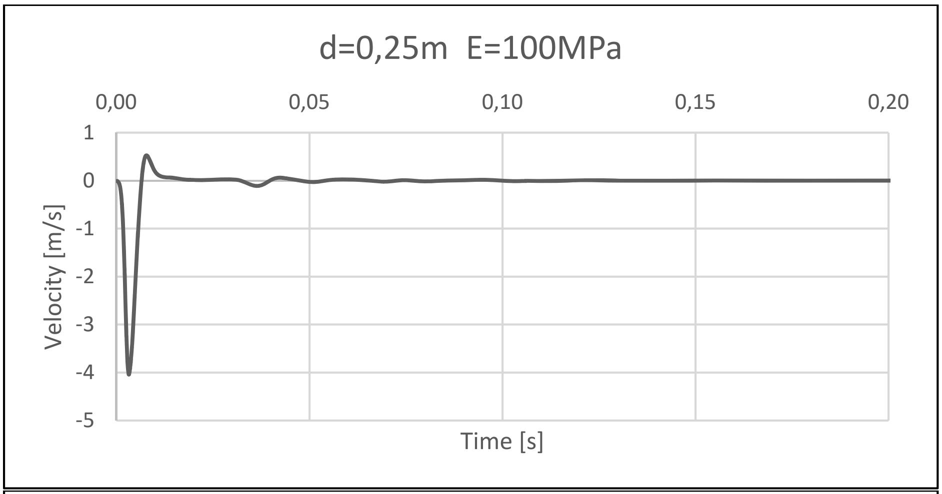

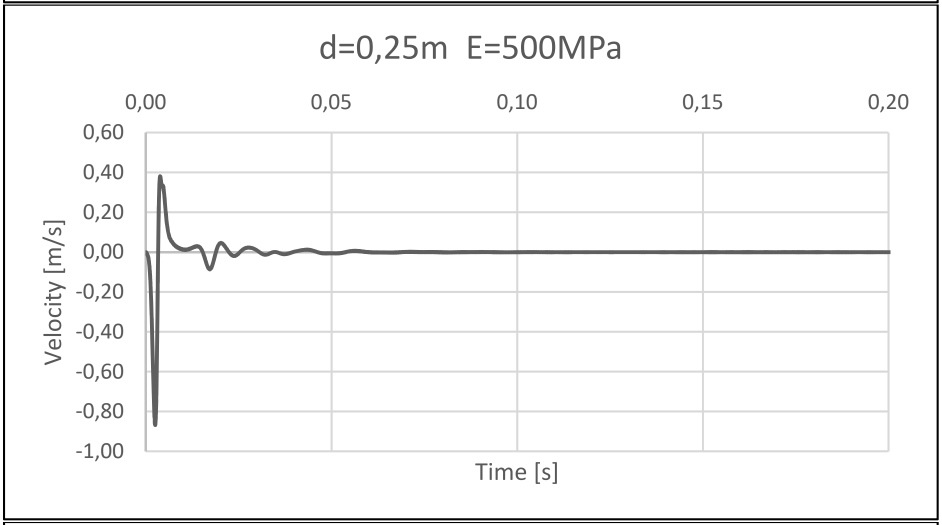

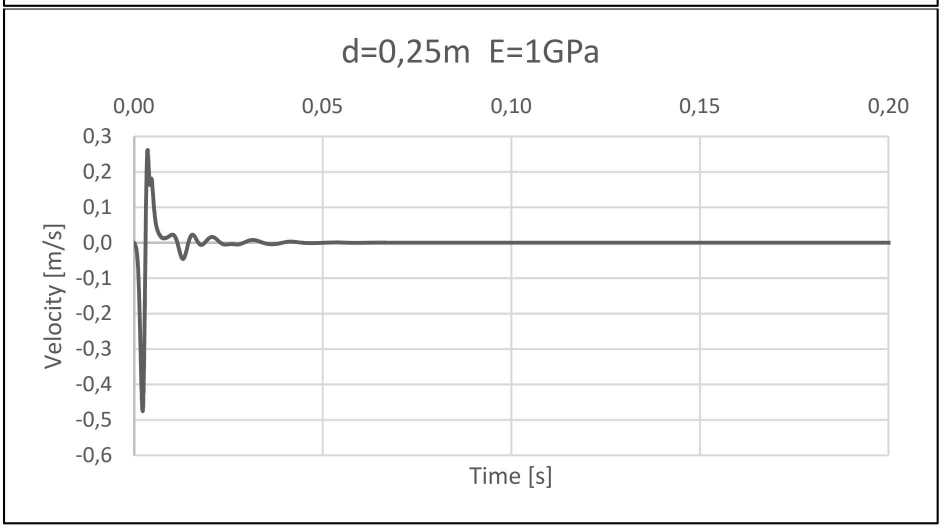

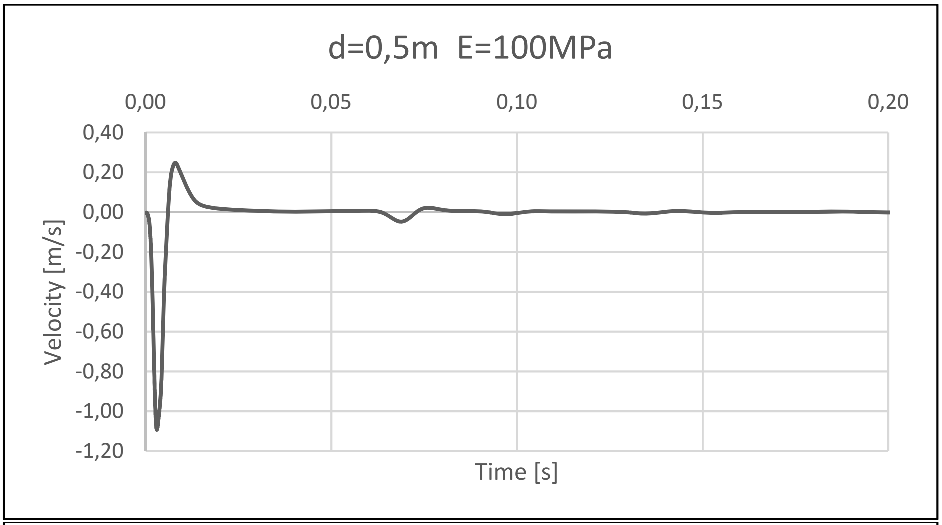
d=0,5m E=100MPa
0,00
0,05
0,10
0,15
0,20
0,40
0,20
0,00
-0,20
-0,40
-0,60
-0,80
-1,00
-1,20
Velocity [m/s]
Time [s]

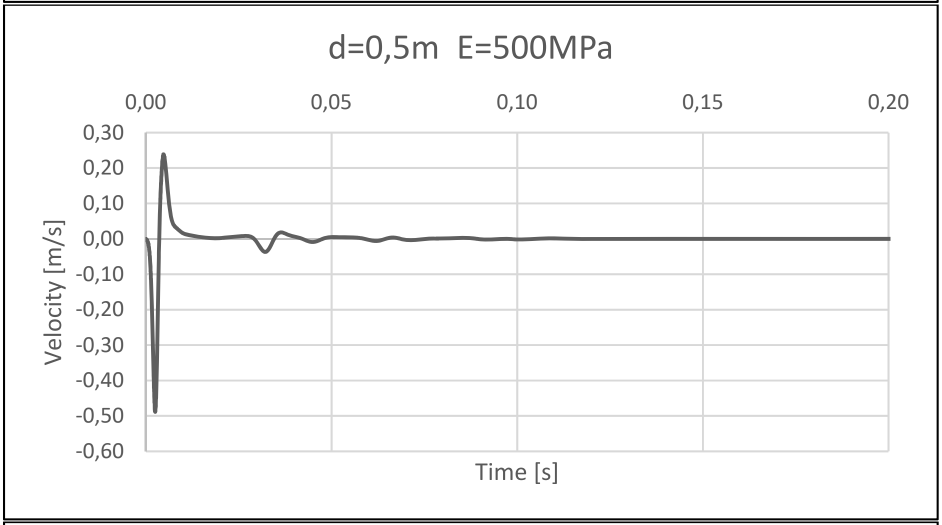
d=0,5m E=500MPa
0,00
0,05
0,10
0,15
0,20
0,30
0,20
0,10
0,00
-0,10
-0,20
-0,30
-0,40
-0,50
-0,60
Velocity [m/s]
Time [s]

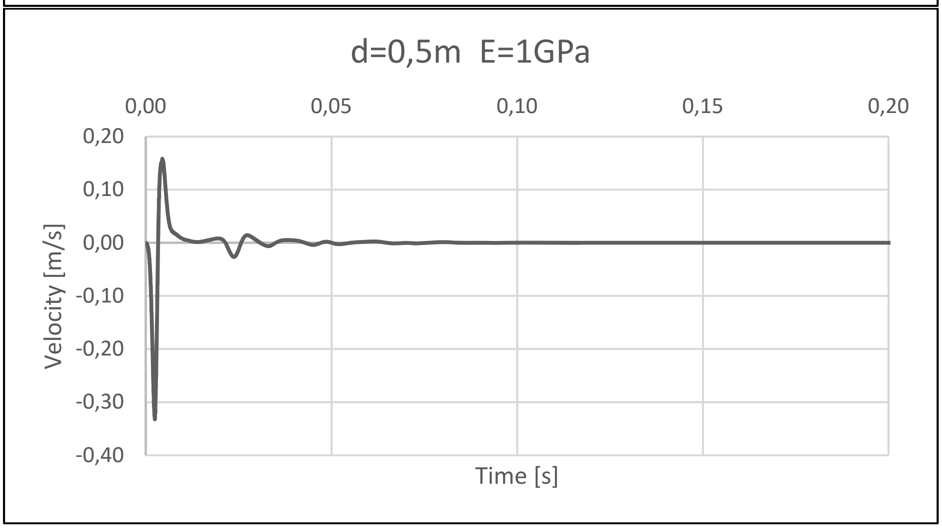
d=0,5m E=1GPa
0,00
0,05
0,10
0,15
0,20
0,20
0,10
0,00
-0,10
-0,20
-0,30
-0,40
Velocity [m/s]
Time [s]

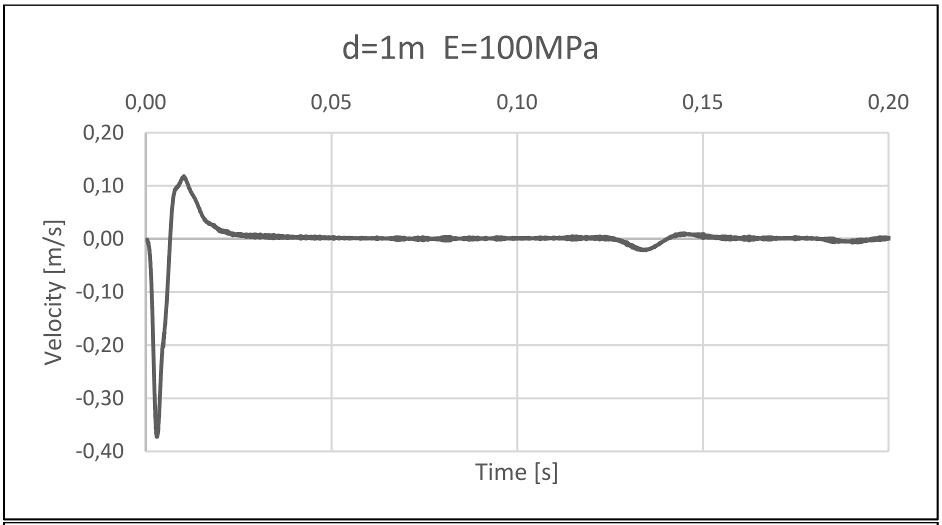
d=1m E=100MPa
0,00
0,05
0,10
0,15
0,20
0,20
0,10
0,00
-0,10
-0,20
-0,30
-0,40
Velocity [m/s]
Time [s]

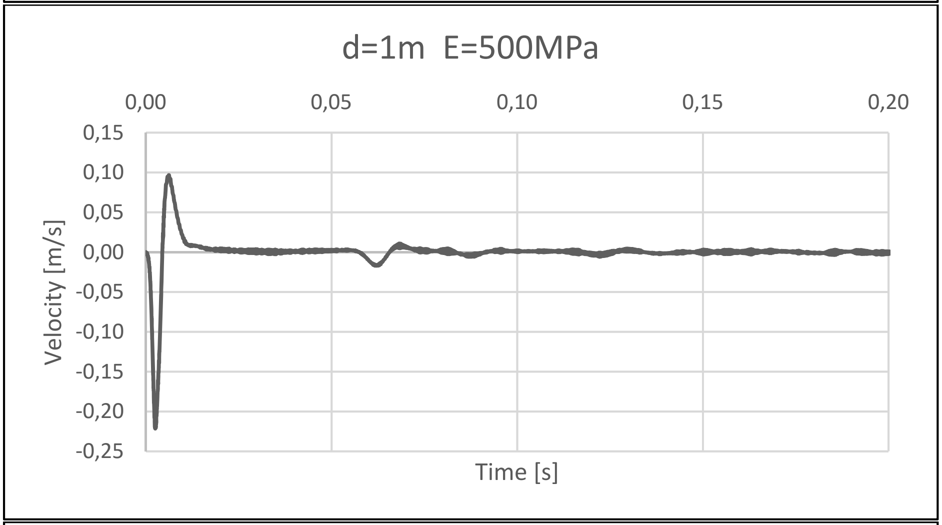
d=1m E=500MPa
0,00
0,05
0,10
0,15
0,20
0,15
0,10
0,05
0,00
-0,05
-0,10
-0,15
-0,20
-0,25
Velocity [m/s]
Time [s]

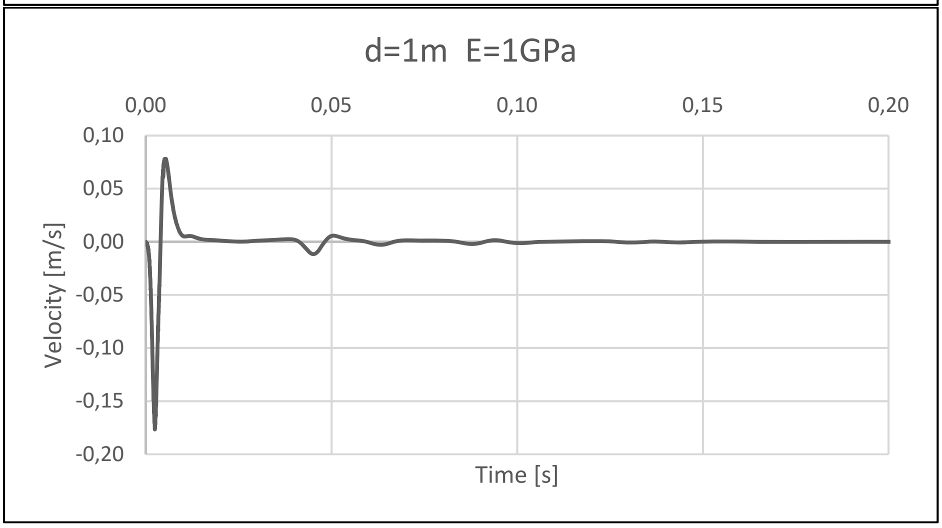
d=1m E=1GPa
0,00
0,05
0,10
0,15
0,20
0,10
0,05
0,00
-0,05
-0,10
-0,15
-0,20
Velocity [m/s]
Time [s]

10.5 Appendix E

- Centered force (0°) database

d [m]	E_u [kPa]	S_u [kPa]	F_y [kN]	f_1 [Hz]	f_2 [Hz]	damping [%]	u_{perm} [m]	$F_{y,norm}$
0,25	1,00E+05	100	1000	45	195	5	9,8E-03	1,26
0,25	1,00E+05	100	2000	45	195	5	3,5E-02	2,53
0,25	1,00E+05	100	3000	45	195	5	6,9E-02	3,79
0,25	1,00E+05	100	4000	45	195	5	1,1E-01	5,06
0,25	1,00E+05	100	5000	45	195	5	1,5E-01	6,32
0,25	5,00E+05	500	1000	45	195	5	2,7E-04	0,25
0,25	5,00E+05	500	2000	45	195	5	2,6E-03	0,51
0,25	5,00E+05	500	3000	45	195	5	7,2E-03	0,76
0,25	5,00E+05	500	4000	45	195	5	1,4E-02	1,01
0,25	5,00E+05	500	5000	45	195	5	2,1E-02	1,26
0,25	1,00E+06	1000	1000	45	195	5	7,4E-05	0,13
0,25	1,00E+06	1000	2000	45	195	5	3,5E-04	0,25
0,25	1,00E+06	1000	3000	45	195	5	1,4E-03	0,38
0,25	1,00E+06	1000	4000	45	195	5	3,2E-03	0,51
0,25	1,00E+06	1000	5000	45	195	5	5,8E-03	0,63
0,5	1,00E+05	100	1000	30	185	5	1,6E-03	0,63
0,5	1,00E+05	100	2000	30	185	5	7,5E-03	1,26
0,5	1,00E+05	100	3000	30	185	5	1,7E-02	1,90
0,5	1,00E+05	100	4000	30	185	5	3,0E-02	2,53
0,5	1,00E+05	100	5000	30	185	5	4,5E-02	3,16
0,5	5,00E+05	500	1000	30	185	5	4,3E-05	0,13
0,5	5,00E+05	500	2000	30	185	5	3,1E-04	0,25
0,5	5,00E+05	500	3000	30	185	5	1,3E-03	0,38
0,5	5,00E+05	500	4000	30	185	5	2,8E-03	0,51
0,5	5,00E+05	500	5000	30	185	5	4,9E-03	0,63
0,5	1,00E+06	1000	1000	30	185	5	3,5E-05	0,06
0,5	1,00E+06	1000	2000	30	185	5	7,1E-05	0,13
0,5	1,00E+06	1000	3000	30	185	5	1,5E-04	0,19
0,5	1,00E+06	1000	4000	30	185	5	4,6E-04	0,25
0,5	1,00E+06	1000	5000	30	185	5	1,1E-03	0,32
1	1,00E+05	100	1000	15	165	5	7,2E-05	0,32
1	1,00E+05	100	2000	15	165	5	7,0E-04	0,63
1	1,00E+05	100	3000	15	165	5	2,4E-03	0,95
1	1,00E+05	100	4000	15	165	5	4,6E-03	1,26
1	1,00E+05	100	5000	15	165	5	7,3E-03	1,58
1	5,00E+05	500	1000	15	165	5	2,6E-05	0,06
1	5,00E+05	500	2000	15	165	5	6,9E-05	0,13
1	5,00E+05	500	3000	15	165	5	7,8E-05	0,19

1	5,00E+05	500	4000	15	165	5	1,8E-04	0,25
1	5,00E+05	500	5000	15	165	5	4,0E-04	0,32
1	1,00E+06	1000	1000	15	165	5	1,8E-05	0,03
1	1,00E+06	1000	2000	15	165	5	3,5E-05	0,06
1	1,00E+06	1000	3000	15	165	5	5,3E-05	0,09
1	1,00E+06	1000	4000	15	165	5	7,2E-05	0,13
1	1,00E+06	1000	5000	15	165	5	9,0E-05	0,16

- <u>Lateral force (45°) database</u>

d [m]	E_u [kPa]	S_u [kPa]	F_y [kN]	F_x [kN]	f_1 [Hz]	f_2 [Hz]	damping [%]	u_{perm} [m]	$F_{x,norm}$
0,25	1,00E+05	100	1000	683	45	195	5	2,4E-02	0,86
0,25	1,00E+05	100	2000	1351	45	195	5	8,4E-02	1,71
0,25	1,00E+05	100	3000	2020	45	195	5	1,6E-01	2,56
0,25	1,00E+05	100	4000	2687	45	195	5	2,5E-01	3,40
0,25	1,00E+05	100	5000	3354	45	195	5	3,6E-01	4,24
0,25	5,00E+05	500	1000	564	45	195	5	1,3E-03	0,14
0,25	5,00E+05	500	2000	1376	45	195	5	8,4E-03	0,35
0,25	5,00E+05	500	3000	2166	45	195	5	2,1E-02	0,55
0,25	5,00E+05	500	4000	2926	45	195	5	3,8E-02	0,74
0,25	5,00E+05	500	5000	3675	45	195	5	5,7E-02	0,93
0,25	1,00E+06	1000	1000	350	45	195	5	1,8E-04	0,04
0,25	1,00E+06	1000	2000	1089	45	195	5	1,6E-03	0,14
0,25	1,00E+06	1000	3000	1922	45	195	5	5,3E-03	0,24
0,25	1,00E+06	1000	4000	2803	45	195	5	1,1E-02	0,35
0,25	1,00E+06	1000	5000	3659	45	195	5	1,9E-02	0,46
0,5	1,00E+05	100	1000	652	30	185	5	4,2E-03	0,41
0,5	1,00E+05	100	2000	1354	30	185	5	1,8E-02	0,86
0,5	1,00E+05	100	3000	2046	30	185	5	3,9E-02	1,29
0,5	1,00E+05	100	4000	2733	30	185	5	6,6E-02	1,73
0,5	1,00E+05	100	5000	3413	30	185	5	9,9E-02	2,16
0,5	5,00E+05	500	1000	458	30	185	5	1,7E-04	0,06
0,5	5,00E+05	500	2000	1180	30	185	5	1,4E-03	0,15
0,5	5,00E+05	500	3000	1948	30	185	5	4,0E-03	0,25
0,5	5,00E+05	500	4000	2723	30	185	5	8,0E-03	0,34
0,5	5,00E+05	500	5000	3492	30	185	5	1,4E-02	0,44
0,5	1,00E+06	1000	1000	383	30	185	5	3,6E-05	0,02
0,5	1,00E+06	1000	2000	819	30	185	5	2,3E-04	0,05
0,5	1,00E+06	1000	3000	1551	30	185	5	9,3E-04	0,10
0,5	1,00E+06	1000	4000	2308	30	185	5	2,2E-03	0,15

0,5	1,00E+06	1000	5000	3085	30	185	5	3,7E-03	0,20
1	1,00E+05	100	1000	625	15	165	5	4,4E-04	0,20
1	1,00E+05	100	2000	1255	15	165	5	2,5E-03	0,40
1	1,00E+05	100	3000	1911	15	165	5	6,2E-03	0,60
1	1,00E+05	100	4000	2587	15	165	5	1,1E-02	0,82
1	1,00E+05	100	5000	3271	15	165	5	1,7E-02	1,03
1	5,00E+05	500	1000	593	15	165	5	2,6E-05	0,04
1	5,00E+05	500	2000	1182	15	165	5	1,2E-04	0,07
1	5,00E+05	500	3000	1776	15	165	5	4,8E-04	0,11
1	5,00E+05	500	4000	2418	15	165	5	1,1E-03	0,15
1	5,00E+05	500	5000	3134	15	165	5	2,1E-03	0,20
1	1,00E+06	1000	1000	524	15	165	5	1,8E-05	0,02
1	1,00E+06	1000	2000	1048	15	165	5	3,6E-05	0,03
1	1,00E+06	1000	3000	1572	15	165	5	6,1E-05	0,05
1	1,00E+06	1000	4000	2097	15	165	5	2,0E-04	0,07
1	1,00E+06	1000	5000	2646	15	165	5	5,0E-04	0,08